

Development of MR Thermometry Strategies for  
Hyperthermia of Extremity and Breast Tumors  
by

Cory Robert Wyatt

Department of Biomedical Engineering  
Duke University

Date: \_\_\_\_\_

Approved:

\_\_\_\_\_  
James R. MacFall, Supervisor

\_\_\_\_\_  
Mark Dewhirst

\_\_\_\_\_  
H. Cecil Charles

\_\_\_\_\_  
Zeljko Vujaskovic

\_\_\_\_\_  
Kathy Nightingale

Dissertation submitted in partial fulfillment of  
the requirements for the degree of Doctor of Philosophy in the Department of  
Biomedical Engineering in the Graduate School  
of Duke University  
2010

ABSTRACT

Development of MR Thermometry Strategies for  
Hyperthermia of Extremity and Breast Tumors

by

Cory Robert Wyatt

Department of Biomedical Engineering  
Duke University

Date: \_\_\_\_\_

Approved:

---

James R. MacFall, Supervisor

---

Mark Dewhirst

---

H. Cecil Charles

---

Zeljko Vujaskovic

---

Kathy Nightingale

An abstract of a dissertation submitted in partial fulfillment of  
the requirements for the degree of Doctor of Philosophy in the Department  
of Biomedical Engineering in the Graduate School  
of Duke University

2010

Copyright by  
Cory Robert Wyatt  
2010

## **Abstract**

Numerous studies have shown that the combination of radiation therapy and hyperthermia, when delivered at moderate temperatures (40°–45°C) for sustained times (30–90 minutes), can help to provide palliative relief and augment tumor response, local control, and survival. However, the dependence of treatment success on achieved temperature highlights the need for accurate thermal dosimetry, so that the prescribed thermal dose can be delivered to the tumor. This can be achieved noninvasively with MR thermometry. However, there are many challenges to performing MR thermometry in the breast, where hyperthermia of locally advanced breast cancer can provide a benefit. These include magnetic field system drift, fatty tissue, and breathing motion.

The purpose of this research was to develop a system for the hyperthermia treatment of LABC while performing MR thermometry. A hardware system was developed for performing the hyperthermia treatment within the MR bore. Methods were developed to correct for magnetic field system drift and to correct for breath hold artifacts in MR thermometry of the tumor using measurement of field changes in fat references. Lastly, techniques were developed for measuring temperature in the fatty tissue using multi-echo fat water separation methods, reducing the error of performing MR thermometry in such tissues. All of these methods were characterized with phantom and in vivo experiments in a 1.5T MR system.

The results of this research can provide the means for successful hyperthermia treatment of LABC with MR thermometry. With this thermometry, accurate thermal doses can be obtained, potentially providing improved outcomes. However, these results

are not only applicable in the breast, but can also be used for improved MR thermometry in other areas of the body, such as the extremities or abdomen.

# Table of Contents

Abstract.....	iv
List of Tables .....	x
List of Figures .....	xi
Acknowledgements.....	xv
1 Introduction .....	1
1.1. Breast Cancer .....	1
1.1.1. Breast and Breast Cancer Therapy.....	1
1.1.2. Epidemiology and Etiology.....	4
1.1.3. Molecular Basis of Breast Cancer.....	6
1.2. Breast Cancer Therapy.....	8
1.2.1. Standard Therapy.....	8
1.2.2. Hyperthermia .....	12
1.2.3. LTSL Liposomes .....	14
1.3. Magnetic Resonance Thermometry .....	16
1.3.1. MR Thermometry Overview .....	17
1.3.2. PRFS-Based MR Thermometry.....	19
1.3.3. Complications of PRFS Thermometry due to $B_0$ Field Drift.....	22
1.3.4. Complications of PRFS Thermometry in Fatty Tissue .....	24
1.3.5. Complications of PRFS Thermometry due to Motion.....	26
1.4. Overview .....	28
1.4.1. Objectives.....	28
1.4.2. Significance .....	31
2 System for Hyperthermia Treatment of Locally Advanced Breast Cancer .....	33
2.1. Introduction .....	33
2.1.1. Need for an improved treatment system for use in the MRI scanner.....	33
2.1.2. Need for Local MR Imaging Coils .....	35
2.1.3. Evaluating the New Treatment System .....	35
2.2. Experimental Methods .....	36
2.2.1. Modifying the Breast Applicator for use in the MR Scanner .....	36

2.2.2.	Construction of the New Patient Support System .....	37
2.2.3	Construction of local MR imaging coils.....	38
2.2.4.	Evaluation of the Treatment System with Volunteer Comfort Study.....	43
2.3	Results.....	44
2.3.1.	Changes to the Breast Applicator .....	44
2.3.2.	Final Treatment System and Comfort Study Results .....	45
2.3.3.	MR Results of the Comfort Study .....	48
2.3.4.	Local Imaging Coils.....	50
2.4	Discussion.....	52
2.5	Conclusion.....	55
3	Field Drift Correction with Oil References in the Extremity and Breast .....	56
3.1	Introduction .....	56
3.2	Theoretical Development .....	57
3.2.1.	Field Fitting Methods.....	57
3.3	Materials and Methods.....	58
3.3.1.	Phantom Creation .....	58
3.3.2.	Field Drift Characterization .....	59
3.3.3.	MAPA Phantom Experiment .....	60
3.3.4	MAPA Leg Experiment .....	62
3.3.5	Breast Applicator Phantom Experiments.....	63
3.3.6	Data Analysis.....	64
3.4	Results.....	66
3.4.1	Field Drift Temporal Behavior.....	66
3.4.2	MAPA Phantom Results .....	68
3.4.3	MAPA In-Vivo Leg Results .....	69
3.4.4	Breast Applicator Results.....	70
3.5	Discussion.....	73
3.6	Conclusion.....	78
4	Development, Characterization, and Optimization of MR Thermometry in Fatty Tissue using IDEAL Fat-Water Separation and Nonlinear Fitting Techniques.....	79

4.1	Introduction .....	79
4.2	Theoretical Development .....	81
4.2.1	IDEAL Temperature Method Development .....	81
4.2.2	Nonlinear Fitting Method Development.....	83
4.2.3	Cramer-Rao Lower Bound model for nonlinear fitting of temperature .....	84
4.3	Experimental Methods .....	87
4.3.1	Parameterization of Echo Times .....	87
4.3.2	Characterizing the Bias of the IDEAL Method and Nonlinear Fitting Method with Simulation .....	88
4.3.3	Characterizing the Nonlinear Fitting Method with Simulation and the CRLB .....	89
4.3.4	Phantom Construction, Spectral and Fat-Water Composition Determination.....	94
4.3.5	Phantom Experiments to Validate IDEAL Method.....	97
4.3.6	Experimental Confirmation of Temperature Noise CRLB for Nonlinear Temperature Algorithm .....	99
4.4	Results.....	101
4.4.1	Bias of the IDEAL algorithm .....	101
4.4.2	Characterizing the Noise Behavior of the Nonlinear Temperature Algorithm ....	103
4.4.3	Phantom Construction, Spectral and Composition Determination .....	110
4.4.4	Phantom Experiments to Validate IDEAL Method.....	113
4.4.5	Experimental Confirmation of Temperature Noise CRLB for Nonlinear Temperature Algorithm .....	121
4.5	Discussion.....	125
4.5.1	Bias of the IDEAL algorithm .....	125
4.5.2	Characterizing the Noise Behavior of the Nonlinear Temperature Algorithm ....	125
4.5.3	Phantom Construction, Spectral and Composition Determination .....	130
4.5.4	Phantom Experiments to Validate IDEAL Method.....	131
4.5.5	Experimental Confirmation of Temperature Noise CRLB for Nonlinear Temperature Algorithm .....	136
4.6	Conclusion.....	138
5	Breath Hold Correction Technique for MR Thermometry of Locally Advanced Breast Cancer	140
5.1	Introduction .....	140



5.2	Materials and Methods.....	140
5.2.1.	Creation of Multi-Gradient Echo Pulse Sequence .....	140
5.2.2.	Phantom Design and Construction .....	143
5.2.3.	Phantom Non-Heating Experiment with Volunteer Breath Holds.....	144
5.2.4.	Phantom Heating Experiment with Simulated Breath Holds.....	146
5.2.5.	In-Vivo Breast Experiment .....	147
5.2.6.	Data Analysis .....	148
5.3	Results.....	151
5.3.1	Multi-Gradient Echo Pulse Sequence .....	151
5.3.1.	Phantom Non-Heating Experiment with Volunteer Breath Holds.....	152
5.3.2.	Phantom Heating Experiment with Simulated Breath Holds.....	159
5.3.3.	In-Vivo Breast Experiment .....	163
5.4	Discussion.....	166
5.5	Conclusion.....	168
6	Future Work.....	170
	Appendix .....	173
	Magnetic Resonance Imaging Review .....	173
	MR Protocol for Breast Comfort Study .....	176
	Volunteer Questionnaire for Breast Comfort Study .....	177
	References .....	178
	Biography .....	194

## List of Tables

Table 1.1: Stages of Breast Cancer .....	4
Table 2.1: Component values for the local imaging coils.....	42
Table 2.2: Breast Comfort Study Questionnaire Responses .....	47
Table 2.3: Water signal percentage values calculated in the fatty and glandular tissue of the breast. ....	50
Table 3.1: Final uncorrected temperature error (°C), final temperature error after correction (°C), and the best percent correction for every trial of each experiment of the oil reference study .....	72
Table 3.2: Average temperature error across all trials of the MAPA leg and phantom experiments for several reference combinations. ....	73
Table 4.1: TE parameters for the MP-IDEAL ESGs. ....	96
Table 4.2: TE parameters for the ESGs to confirm the temperature noise CRLB values.....	100
Table 4.3: Calculated $A_w$ , $A_f$ , $T2^*_w$ , $T2^*_f$ , and SNR for all fat-water phantom experiments .....	113
Table 4.4: Temperature variation of IDEAL temperature values minus fiber optic temperature values for three echo and five echo reconstructions .....	119
Table 5.1: Description of experiment parameters for the non-heating phantom experiments .....	146
Table 5.2: ESG values used for water and fat fitting with MP-IDEAL.....	150
Table 5.3: Mean and standard deviation of all the time points in each experiment for both the uncorrected and corrected data sets. ....	158
Table 5.4: Average Root Mean Squared (RMS) deviation across all time points of the two heating experiments.....	162
Table 5.5: Mean and standard deviation of all time points of the uncorrected and corrected data sets for the in vivo breast experiment .....	166

## List of Figures

Figure 1.1: Internal anatomy of the human breast anatomy of the human breast .....	2
Figure 1.2: Location of lymph nodes surrounding the breast .....	3
Figure 1.3: Standard treatment regimen for LABC .....	12
Figure 1.4: Percent temperature error vs. percent water signal for a simulated fat-water voxel ...	25
Figure 2.1: First prototype of the patient support system .....	34
Figure 2.2: 3D model of the GE breast coil used as a mold for the patient support .....	38
Figure 2.3: Diagram detailing the size and positioning of the coils on the breast applicator using the custom holders .....	39
Figure 2.4: Schematic of the MR imaging coil .....	40
Figure 2.5: Pictures of the modified breast applicator .....	45
Figure 2.6: Pictures of new patient support system .....	46
Figure 2.7: MR images of a volunteer's breast inside the applicator.....	48
Figure 2.8: Water and fat separated images of a volunteer's breast inside the applicator. ....	49
Figure 2.9: Pictures of both prototype local imaging coils .....	50
Figure 2.10: Pictures of both etched local imaging coils .....	51
Figure 2.11: Pictures of the etched local imaging coils on the breast applicator.....	51
Figure 2.12: SNR of the local coils and body coil for the single echo sequence.....	52
Figure 2.13: SNR of the local coils and body coil for the 15.4ms echo of the multi-gradient echo sequence.....	52
Figure 3.1: Construction and materials of the phantoms used in the experiments.....	59
Figure 3.2: Pictures of the MAPA and breast applicators.....	62
Figure 3.3: Images of the experimental setup for the oil reference experiments .....	64
Figure 3.4: Long-term frequency drift of the 1.5T magnet.....	67

Figure 3.5: Frequency drift over time for all trials of the MAPA phantom and leg experiments..	68
Figure 3.6: Results from the MAPA phantom experiment .....	69
Figure 3.7: Results from the MAPA leg experiment .....	70
Figure 3.8: Results from the breast applicator phantom experiment .....	71
Figure 4.1: Diagram explaining the parameterization of the phase difference between the water and fat signals each TE value of an ESG .....	88
Figure 4.2: PRESS spectra at the center of each fat-water phantom .....	95
Figure 4.3: Temperature bias of the IDEAL and NLM-Temp algorithms.....	102
Figure 4.4: $B_0$ field bias of the IDEAL and NLM-Temp algorithms.....	102
Figure 4.5: Simulation temperature noise values from NLM-Temp plotted along with the CRLB temperature noise calculations, both using the same input values.....	104
Figure 4.6: Temperature noise CRLB across several rotations for a constant $T2^*_w$ and changing $T2^*_f$ .....	105
Figure 4.7: Temperature noise CRLB maps for 3-echo, 5-echo, and 7-echo ESGs with starting and separation angles ranging from $1^\circ$ to $360^\circ$ .....	106
Figure 4.8: Temperature noise CRLB maps as a function of starting angle and separation angle with different values of fat-water frequency differences .....	107
Figure 4.9: Temperature noise CRLB for starting angle and separation angle = $150^\circ$ for a varying fat signal %.. .....	108
Figure 4.10: Multifactorial, combined simulation showing temperature noise CRLB as a function of starting angle and separation angle.....	109
Figure 4.11: CRLB minimum temperature noise for number of echoes, N, varying from 3 to 15. ....	110
Figure 4.12: Measured vs. Fit water and fat signal for each fat-water phantom.....	111
Figure 4.13: Measured vs. Fit total signal for each fat-water phantom .....	112
Figure 4.14: Experimental setup for the IDEAL temperature experiments .....	114
Figure 4.15: IDEAL reconstructed water-only images and fat-only images for phantom with 50:50 water to fat ratio.....	115

Figure 4.16: IDEAL calculated $B_0$ field maps using three and five echoes in the 50:50 water-fat phantom. . . . .	116
Figure 4.17: Plots of IDEAL temperature vs. Fiber Optic Temperature for All Fat-Water Phantoms. . . . .	118
Figure 4.18: IDEAL Temperature maps for all water-fat phantoms at 6 time points during data acquisition . . . . .	120
Figure 4.19: Phantom results of measured temperature noise and CRLB temperature noise for 3-echo ESGs. . . . .	122
Figure 4.20: Phantom results of measured temperature noise and CRLB temperature noise for 5-echo ESGs. . . . .	123
Figure 4.21: Phantom results of measured temperature noise and CRLB temperature noise for 7-echo ESGs. . . . .	124
Figure 5.1: Pulse sequence diagram for the custom multi-gradient echo pulse sequence . . . . .	143
Figure 5.2: Construction of phantom mimicking a large breast with LABC . . . . .	144
Figure 5.3: Picture of the fat-water phantom developed for the breath hold experiments . . . . .	144
Figure 5.4: Comparison of IDEAL results for the single echo and multi echo sequences . . . . .	152
Figure 5.5: Picture of phantom secured inside the breast applicator . . . . .	154
Figure 5.6: A MR image of the phantom inside the applicator with the volunteer on top. . . . .	154
Figure 5.7: Overlay of a field change map on the magnitude image of the phantom in the applicator . . . . .	155
Figure 5.8: Comparison of field measured and field fit using the LSSP algorithm for the first phantom non-heating experiment . . . . .	155
Figure 5.9: Uncorrected and corrected temperature change measurements in the water gelatin for experiment #1 of the non-heating phantom experiments . . . . .	156
Figure 5.10: Uncorrected and corrected temperature change measurements in the water gelatin for experiment #2 of the non-heating phantom experiments . . . . .	157
Figure 5.11: Uncorrected and corrected temperature change measurements in the water gelatin for experiment #3 of the non-heating phantom experiments . . . . .	158

Figure 5.12: Experimental setup of the phantom in the applicator, the air bolus, and the water bolus for the phantom heating experiments .....	159
Figure 5.13: Magnitude image of the phantom in the applicator and the boluses on top .....	160
Figure 5.14: Comparison of field measured and field fit using the LSSP algorithm for the first phantom heating experiment .....	160
Figure 5.15: Uncorrected and corrected temperature change measurements in the water gelatin for the first phantom heating experiment .....	161
Figure 5.16: Uncorrected and corrected temperature in the water gelatin for the second phantom heating experiment.....	162
Figure 5.17: Magnitude image of the volunteer’s right breast in the applicator .....	163
Figure 5.18: Fat and water separated images using MP-IDEAL for the in vivo experiment.....	164
Figure 5.19: Field change map used in the LSSP method for the in vivo experiment.....	164
Figure 5.20: Uncorrected and corrected temperature maps at the last breath hold for the in vivo experiment .....	164
Figure 5.21: ROI of pixels used in the left side of the glandular tissue used for sampling and plot of the uncorrected and corrected temperature change across all time points.....	165
Figure 5.22: ROI of pixels used in the right side of the glandular tissue used for sampling and plot of the uncorrected and corrected temperature across all time points..	165

## **Acknowledgements**

First, I would like to thank my girlfriend, Aubrey, for her support throughout this work. Her patience, understanding, and caring help make my work possible. I also would like to thank my parents, Bob and Marcia, for their continual care and concern. I would not be where I am today without their constant support. Additionally, I would like to thank my brother, Kevin, for supporting me and taking me to the airport for all my graduate school interviews.

I would also like to express my sincere gratitude to all the people that have assisted me in my research. First, I would like to thank my advisor, James MacFall, for providing me with the knowledge, guidance, and support necessary to and to perform good science and to be a successful PhD student. I would also like to thank my committee members. Cecil Charles for helping me with all things MR and providing words of wisdom. Mark Dewhirst for providing both grant support, project direction, and good feedback. Zeljko Vujaskovic and Kathy Nightingale for their constructive feedback and support.

I would like to thank Brian Soher for his support, teaching, and advice given throughout this research. Also, I extend my sincere gratitude to Paul Stauffer, Paolo Maccarini, Kavitha Arunachalam, Valeria De Luca, Carlos Daniel Martin, Yu Yuan, Sneha Rangarao, Yngve Birkelund, Oystein Klemetsen, and Sara Salahi for supporting and assisting in this research and for engaging in many fruitful conversations. I would also like to thank Gary Cofer, Bastiaan, Al Johnson, and the CIVM laboratory for their support in both building my MR coils, providing me with access to a GE EPIC compiler,

and providing nitrogen for experiments. I would like to thank Kevin Kelley and Jerry Dalhke for assistance in learning and running the GE MRI system and for many MR scanner lessons.

Research was supported NCI grant #PO1-CA042745 and NIH grant #T32-EB001040. Education supported by the Duke Biomedical Engineering Department and NIH grant #T32-EB001040.



# **1 Introduction**

## **1.1. Breast Cancer**

### **1.1.1. Breast and Breast Cancer Therapy**

The human female breast consists of milk-producing glands that are surrounded by layers of connective tissue and fat. The glands consist of approximately 12-20 lobules that branch out from the nipple. Each lobule is composed of tiny, hollow sacs called alveoli, which produce the milk. The alveoli are connected to the nipple through a network of small vessels called the lactiferous ducts. At the areola, the region of tissue near the nipple, the smaller ducts combine into larger ducts which exit through the nipple. The lobules are supported by the surrounding fatty tissue, which is composed of fat, connective tissue, and ligaments. All of the lobules and ducts are often referred to as fibroglandular tissue. The entire breast is supported by ligaments attached to the chest wall, which allows it to rest on the pectoralis major muscle, separating the breast from the ribcage. Lastly, the lymphatics of the breast drain into lymph nodes under the armpit, above the collarbone, and behind the breastbone. A diagram of the internal anatomy of the breast is shown in Figure 1.1(based on[1]), while a diagram of the locations of the various lymph nodes is shown in Figure 1.2 (based on [2]).

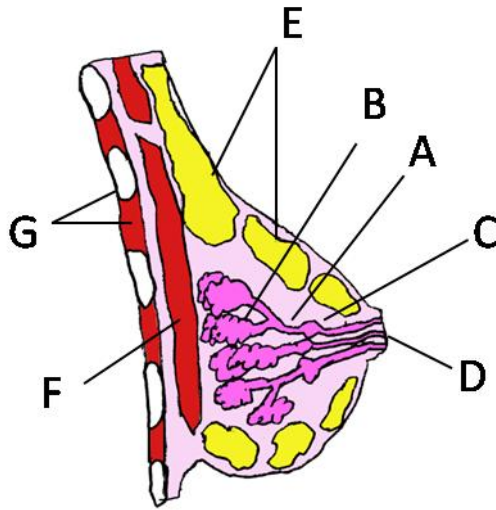


**Figure 1.1:** Internal anatomy of the human breast anatomy of the human breast (A) Lactiferous ducts (B) Lobules (C) Dilated section of duct to hold milk (D) Nipple (E) Fatty Tissue (F) pectoralis major muscle (G) Chest wall/Rib cage[1]

The volume and content of the tissues can change over both short and long periods of time. During menstruation, the fibroglandular tissue volume, water content, and total breast volume can increase by approximately 10% [3] due to the effects of increased estrogen and progesterone. The breast then returns to normal after the cycle, due to the return to normal concentrations of hormones. As a woman ages, the amount of fibroglandular tissue in the breast decreases slowly until menopause, when the decrease becomes more rapid and the fibroglandular tissue is replaced with fatty tissue [4-6]. One study found that water content dropped approximately 10-20% post-menopausal, with an equal increase in fat content [7]. These changes are due to decreased levels of estrogen and other hormones.

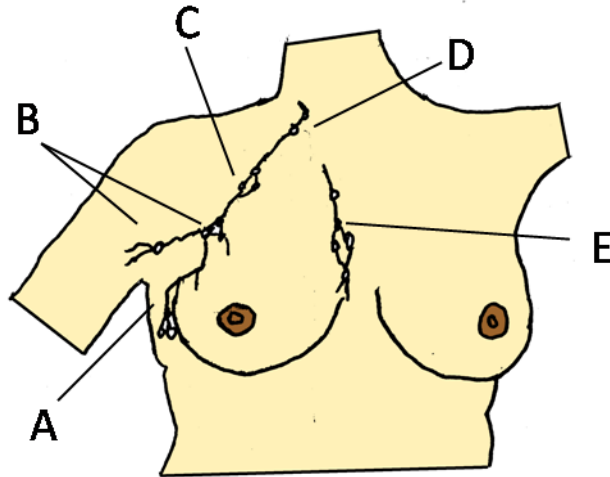


**Figure 1.2:** Location of lymph nodes surrounding the breast (A) Axillary lymph nodes level I (B) Axillary lymph nodes level II (C) Axillary lymph nodes level III (D) Supraclavicular lymph nodes (E) Internal mammary lymph nodes[2]

Breast cancer originates in the fibroglandular tissue and is usually classified by which portion of the glands they originate from. The two types are ductal carcinoma (originates in the ducts) and lobular carcinoma (originates in the lobules). These are further classified as in situ or invasive. Invasive carcinoma is cancer that has spread into the surrounding fatty tissue, while in situ carcinoma has yet to spread.

There are 5 stages of breast cancer that depend on the invasiveness, size, and location of the carcinoma. A table detailing all 5 stages is shown in Table 1.1[8]. Generally, stages 0, I, and II are known as early stage breast cancers while III and IV are known as late stage cancers. Locally advanced breast cancer (LABC) is another name given to most late stage carcinomas. LABC involves all tumors that meet any of the following conditions: greater than 5 cm in diameter, involves the skin or chest wall, and

axillary lymph node or ipsilateral supraclavicular, infraclavicular, or internal mammary node involvement[9].

**Table 1.1: Stages of Breast Cancer[8]**

Stage 0	Noninvasive breast carcinomas
Stage I	Invasive carcinoma that is less than 2cm in diameter and has not spread beyond the breast
Stage IIA	No tumor in breast but cancer in axillary lymph nodes OR Tumor is 2cm or smaller and has spread to axillary lymph nodes OR Tumor is greater than 2cm but less than 5cm in diameter, no lymph node involvement
Stage IIB	Larger than 2cm but less than 5cm in diameter and has spread to axillary lymph nodes OR Larger than 5cm in diameter but has not spread to axillary lymph nodes
Stage IIIA	Tumor is not present in the breast or can be present at any size AND The cancer has spread to axillary lymph nodes that are connected to each other or other structures or lymph nodes near the breastbone
Stage IIIB	Tumor present in the breast at any size AND Has spread to chest wall or skin of the breast AND The cancer may have spread to axillary lymph nodes that are connected to each other or other structures or lymph nodes near the breastbone
Stage IIIC	May be no sign of cancer or cancer of any size AND May have spread to chest wall or skin of the breast AND Has spread to lymph nodes above or below the collarbone AND May have spread to axillary lymph nodes or lymph nodes near the breastbone
Stage IV	Cancer has spread to other organs of the body

### 1.1.2 Epidemiology and Etiology

This section is a summary of facts found in the American Cancer Society’s Breast Cancer Facts and Figures 2009-2010 publication[10].

Cancer is a class of diseases that is characterized by the uncontrolled growth and spread of abnormal cells, that can affect many parts of the body including the brain, breast, prostate, liver, lungs, colon, and reproductive systems. According to the American Cancer Society, cancer is the second leading cause of death in the United States for men and women[10]. Of those deaths, breast cancer is currently the second leading cause of cancer-related deaths of women in the US, behind lung cancer. However, as of 2008, breast cancer has the highest rate of incidence of all cancers in

women. In 2009, there is expected to be 192,370 newly diagnosed cases of invasive breast cancer and 62,280 newly diagnosed cases of in situ breast cancer in women. In the same year, approximately 40,170 women are expected to die from breast cancer. Breast cancer incident rates increased steadily from 1978 (the year they were first recorded) to 1987. From 1987 to 1994, breast cancer incidence rates were stable. Then, from 1994 to 2002, breast cancer incidence rates increased again. However, since 2002, incidence rates have been on the decline. All of the periods discussed above are linked to reductions or increases in risk factors among the population[10].

There are several risk factors for breast cancer. First, family history plays a large role, particularly if a first-degree relative has been diagnosed. While many breast cancer cases are combinations of lifestyle factors and low-risk genetic factors, 5-10% of cases are result from inheritance of mutations to the breast cancer susceptibility genes, BRCA1 and BRCA2. However, BRCA1 and BRCA2 only account for approximately 50% of familial breast cancer cases[10].

Another important risk factor is age, with the probability of a person being diagnosed with breast cancer increasing with age. The lifetime risk of developing breast cancer is higher today than in the 1970's, which is due in part to an increase in life expectancy and to the overall increase in incidence discussed previously[10].

Hormonal levels are another large risk factor. Reproductive hormones can increase cancer risk by promoting cell proliferation and DNA damage. There are several conditions or medications that alter hormones in such a way as to increase the risk of developing breast cancer. First, girls who enter puberty early (<12 years) or women who have late menopause (>55 years) have a higher risk for breast cancer[10]. Pregnancy also

plays a significant role, with women who have their first child later in life (>30 years) having a higher risk[10]. Also, the number of pregnancies is significant, with the risk for breast cancer decreasing with the number of pregnancies. However, after any pregnancy, there is a transient increase in the risk of breast cancer, particularly after the first birth of an older woman. Breastfeeding has been shown to decrease breast cancer risk, with longer duration providing less risk[10]. Oral contraceptives increase breast cancer risk, but the risk is negligible 10 years after a woman stops taking them. Lastly, menopausal hormone therapy, which includes estrogen and progestin, has been shown to increase risk, with higher risk associated with longer use[10].

There are several anatomical and physical risk factors for breast cancer that have not been discussed. First, increased breast tissue density and bone density are associated with higher breast cancer risk. Obesity is also linked with increased risk, but only for postmenopausal women. Additionally, physical activity is associated with a lower risk of breast cancer, with the largest effects being seen in postmenopausal women and women with normal BMI.

Lastly, exposure to ionizing radiation has been correlated with increased risk of breast cancer, due to the mutations in cellular DNA.

### **1.1.3 Molecular Basis of Breast Cancer**

Breast carcinogenesis is the process in which normal cells in the breast are transformed into cancer cells. Carcinogenesis was originally thought to have three phases: usual hyperplasia, pre-malignant cell changes that lead to atypical hyperplasia,

and finally developing into in-situ carcinoma[11]. However, in 2001 it was shown that usual hyperplasia is genetically unaltered and characterized by another cytokeratin profile than ductal carcinoma in situ (DCIS)[12]. Therefore, new models have been proposed in which atypical hyperplasia is a direct precursor to DCIS and lobular carcinoma in situ (LCIS)[13]. In the model usual hyperplasia branches off at an early stage[14, 15]. From that point in situ carcinomas can progress into invasive carcinomas when they break through the basement membrane of either the duct or lobule into the surrounding tissue. Lastly, the invasive carcinoma can become metastatic by invading blood vessels or lymphatic channels and circulating to other organs.

All of the events in breast carcinogenesis can occur due to mutations or loss of the function of genes that control the proliferation of the cell. There are two main classes of these genes, oncogenes and tumor suppressor genes. Oncogenes are genes that promote malignancy with their activation or increased activation. Conversely, tumor suppressor genes promote malignancy through the loss of gene function.

There are a few key oncogenes that have been identified as playing a role in the progression of breast carcinogenesis. These include HER-2, EGFR (also known as HER-1), and the c-myc oncogenes. The HER receptors contribute to proliferation, angiogenesis, altered cell-cell interactions, increased cell motility, metastases, and resistance to apoptosis[16]. C-myc is involved in cellular proliferation, differentiation, and apoptosis, hormone responsiveness, and chemotherapy resistance[17].

The main tumor suppressor genes include p53, p27, BRCA-1, and BRCA-2. The p53 gene is the most important tumor suppressor gene since it is mutated in about half of human cancer cases and approximately 20-30% of breast cancer cases[18]. The p53 gene

can arrest cell division to allow for DNA repair and can help trigger apoptosis or cell differentiation. Thus, if p53 is mutated and defective, then the cell cannot undergo the repair it needs or undergo apoptosis when facing cancer causing mutation. The p27 gene operates through a different mechanism but can also arrest cell division. BRCA-1 and BRCA-2 are two genes which are involved in DNA repair but work through different mechanisms. Approximately 0.12% of the population carries a mutation of BRCA-1, but people with mutations have a 49-73% chance by age 50 and 71-87% chance by age 70 of developing breast cancer[19-21]. Similar rates have been found for BRCA-2.

## **1.2 Breast Cancer Therapy**

Most patients with LABC present with a tumor that can be diagnosed easily by palpation. Histologic diagnosis is then performed with either core needle biopsy or fine-needle aspiration (FNA). Either method can be used to determine the estrogen receptor (ER), progesterone receptor (PR), and HER-2 status of the tumor. Mammography, ultrasound, and MRI are several methods that can then be used to determine the extent of local disease. Ultrasound and MRI are particularly useful at evaluating possible infiltration of the tumor into the lymph nodes.

### **1.2.1 Standard Therapy**

Initially, LABC treatment involved the use of radical mastectomy[22]. Radiation therapy alone was also used, but was found to have serious complications when using the doses needed to achieve local control (>6000 rads[23]). These complications include chest-wall fibrosis, brachial plexopathy, lymphedema, skin ulceration, and rib



necrosis[23]. However, both surgery and radiation therapy alone had poor 5-year disease free survival (DFS) rates: 41% and 29% respectively[24]. Combining surgery and radiation therapy did improve local control, but overall survival (OS) was not significantly improved over either therapy by itself[25]. This was due to the fact that many of the patients receiving combined therapy still died from metastatic disease. The lack of survival due to metastatic disease after local therapy highlights the need for a systemic therapy in the treatment of breast cancer[26].

The need for systemic therapy can be addressed with chemotherapy. Several studies have shown that adjuvant chemotherapy given before mastectomy for patients with stage I-III breast cancer results in significant reduction in the rates of recurrence and risk of death. One study with cyclophosphamide, methotrexate, and fluorouracil treatment after mastectomy showed a 34% reduction in the relative risk of recurrence and a 26% reduction in the relative risk of death[27]. A meta-analysis of several studies with adjuvant chemotherapy given after surgery showed similar results[28]. Adjuvant radiation therapy was compared to adjuvant chemotherapy in a study of 120 patients with operable stage III breast cancer that were randomized to receive postoperative radiation therapy alone, postoperative chemotherapy alone, or radiotherapy and chemotherapy. Adjuvant levamisole immunotherapy was administered for all cases. The 3-year recurrence rates were 68% for patients who received chemotherapy alone, 57% for patients who received radiation therapy alone, and 13% for those who received both treatments, with all results being statistically significant ( $p < 0.001$ )[29]. The investigators also found a survival benefit for patients who received both chemotherapy and radiation therapy, with the 3-year OS rates being 57% for patients who received radiation therapy

alone in contrast to 72% for those who received chemotherapy alone, and 90% for those who received both chemotherapy and radiation therapy. Levamisole immunotherapy was found to increase the DFS from 12 to 18 months when compared to a 60 patient control group.

The previous results show that combining adjuvant therapies with surgery can significantly improve both DFS and OS. However, adding chemotherapy before surgery or other treatments can provide significant advantages. This form of chemotherapy is typically called neoadjuvant chemotherapy or neoadjuvant system therapy (NST). NST has several advantages with LABC treatment that include earlier treatment of subclinical distant micrometastases, downstaging of the primary tumor (which may allow for operability), and the ability for an in vivo assessment of response to specific chemotherapy agents[30]. There have been a few trials on the effect on survival of NST on LABC. Most have demonstrated equivalent outcomes between trials with only neoadjuvant chemotherapy and trials with only adjuvant chemotherapy[31, 32]. The only negatives involved from neoadjuvant chemotherapy are the delay of local therapy and potential increase in chemotherapeutic drug resistance[26]. Thus, NST is included in most treatment plans of LABC.

A clear picture of a typical treatment plan for LABC can be found in Figure 2[26]. To recap, after biopsy, neoadjuvant chemotherapy is administered. This can be either an anthracycline based regimen or a combination of anthracycline and taxane. However, studies have shown that there is no difference in the pathological complete response (pCR) or other clinical endpoints (DFS or OS) between the two regimens[33, 34]. In Figure 1.3, a sequential regimen is shown, where anthracycline is given as the

neoadjuvant drug while a taxane is given as the adjuvant drug. After NST, modified radical mastectomy is performed if the tumor is operable, which is often made possible due to NST. If the tumor is still inoperable after NST, radiation therapy is performed to possibly shrink the tumor further. After local surgery, adjuvant radiation therapy is performed, which has been shown to reduce the rates of locoregional recurrence (LRR) in LABC and inflammatory breast cancer[35-37]. However, more studies are needed to determine the optimal time for radiation therapy after surgery and the selection of RT fields after response to NST[30]. Finally, adjuvant hormonal therapy is given if the tumor is ER+ or PR+.

Up to 80% of patients treated with chemotherapy or hormonal therapy have objective responses, and a small percentage of these patients will have a complete response[26]. It is worth noting that patients that are positive for HER2/neu, a growth promoting factor, typically receive hormonal treatments of either Herceptin or Lapatinib instead of the more common hormonal treatments. HER2/neu is found in approximately 15-30% of breast cancer cases[10]. Herceptin has been shown to reduced the risk of recurrence and death by 52% and 33%, respectively, when given with chemotherapy compared to chemotherapy alone[10].

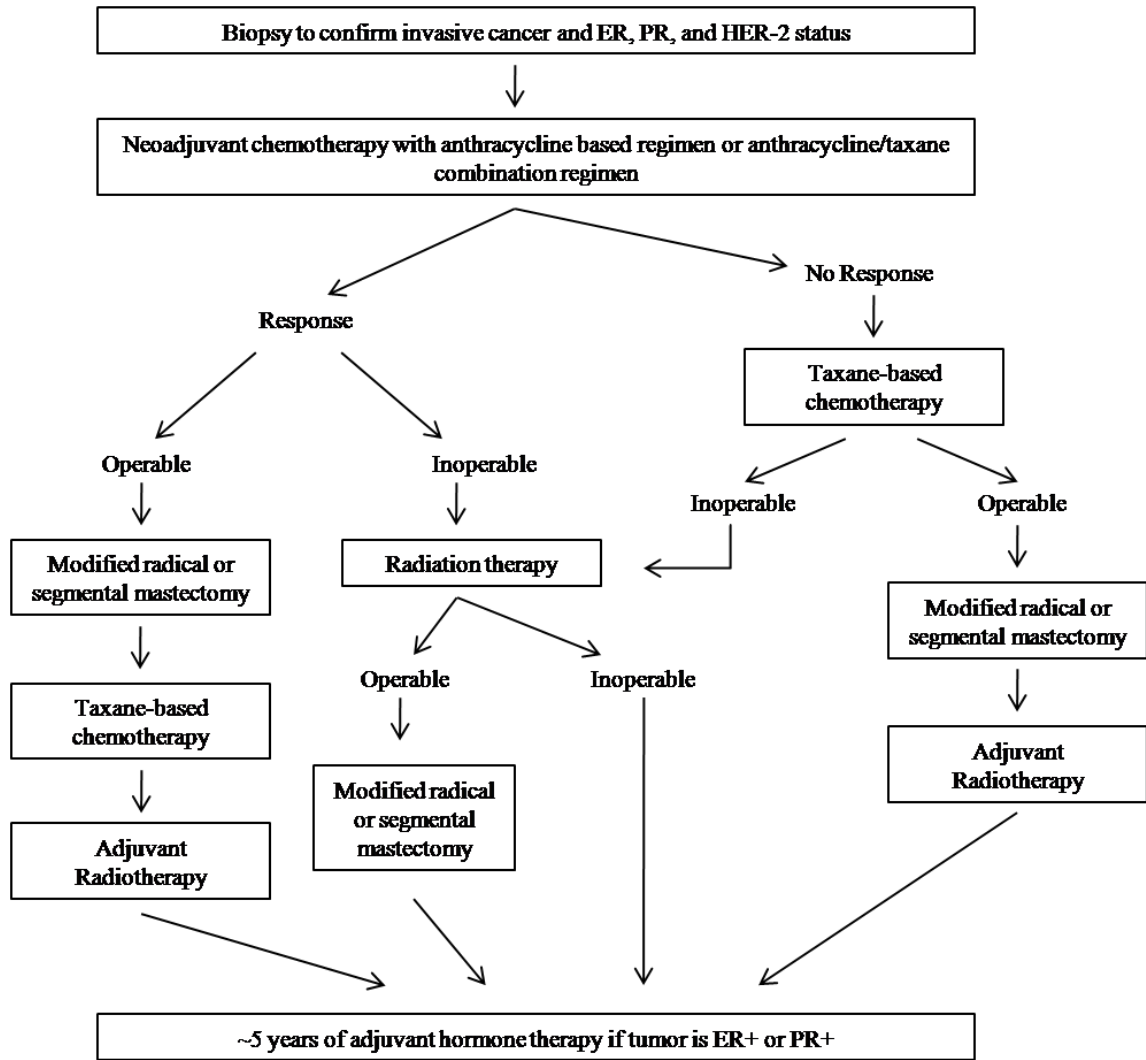


**Figure 1.3:** Standard treatment regimen for LABC

## 1.2.2 Hyperthermia

Hyperthermia (HT) is a therapeutic technique in which cancerous tissue is heated to 40-45°, inducing vascular and cellular changes that improve the therapeutic effectiveness when used in conjunction with chemotherapy or radiation therapy[38]. In Figure 1.3, HT would be given concurrently with any of the radiotherapy or chemotherapy treatments. HT induces many cellular and vascular changes which provide

clinical benefits that make it synergistic with many chemotherapeutic agents and radiation therapy. In particular, it has been shown to enhance chemotherapy and radiation therapy in LABC [39] and superficial breast cancer[40]. First, HT inactivates DNA repair and promotes the immune response to cancer through activation of macrophages and NK cells, while also promoting the induction of cytokines. A number of vascular changes occur with HT that improve oxygen delivery (for radiosensitization) and drug delivery[38].

There are a number of devices that can be used to heat a target into the hyperthermic range. The most common devices are radiofrequency (RF) applicators, which use tuned antennas to transmit RF energy into the body. However, RF applicators are best used to heat deep-seated tumors, due the long wavelengths of RF[41-43]. Microwave applicators are also used, but are typically used only for superficial tumors due to their small wavelength[44, 45]. Both types can be used in different configurations, with the most common being phased arrays, waveguides, and spiral antennas. Less used are ultrasound applicators[46, 47] and magnetic fluids[48, 49], which are heated up by applying alternating magnetic fields.

Numerous studies have shown that the combination of radiation therapy and hyperthermia, when delivered at moderate temperatures (40°–45°C) for sustained times (30–90 minutes), can help to provide palliative relief and augment tumor response, local control, and survival[38, 50, 51]. Positive phase III clinical trials comparing radiation therapy with or without hyperthermia have been reported for several tumor sites, including recurrent breast cancer on the chest wall[52], melanoma[53], advanced head and neck cancer[54], and esophageal cancer[55]. Very few clinical trials have been

performed involving hyperthermia of LABC. However, a trial at Duke University involving 43 evaluable patients receiving hyperthermia alongside neoadjuvant chemotherapy (using paclitaxel and liposomal Doxorubicin) showed that significant doses of heat were significantly correlated with an improved pathologic response, which in turn showed a trend towards improved survival[56].

### **1.2.3 LTSL Liposomes**

While adjuvant or neoadjuvant chemotherapy does improve survival, normal tissue and organ toxicities are a major limitation to delivering a therapeutic dose to the tumor. One solution for reducing toxicity involves targeting the tumor with temperature sensitive liposomal drug delivery. A basic liposome consists of phospholipids arranged in a bilayer, forming a vesicle. However, several modifications were needed to make the liposome ideal for drug delivery. Initial studies with the chemotherapy drug Doxorubicin (DOX) showed significant leakage of the drug[57]. This was corrected by creating a transmembrane pH gradient in the liposome, with the contents of the liposome being more acidic[58]. When liposomes were initially used in vivo, there was rapid entrapment of the liposomes in the liver, spleen, and bone marrow, limiting circulation to approximately 30 minutes in humans. Circulation was improved by adding polyethylene glycol-derivatized lipids (PEG lipids) to the lipid bilayer, which prevents opsonization and liposome aggregation, two mechanisms leading to the entrapment[59-61]. Both PEG coated liposomes and normal liposomes have been used for drug delivery since they passively target tumors due to their increased vascular permeability[62, 63]. However, it has been shown that liposomes can be targeted further by attaching antibody or receptor

targets onto the liposomes. Using these improvements, delivery of doxorubicin in liposomes has been shown to reduce cardiotoxicity, myelosuppression, and alopecia in comparison to free doxorubicin[64]. Unfortunately, accumulation of the drug in the tumor can be inadequate due to the slow release of the drug from the liposome[57]. To address this, temperature-sensitive liposomes (TSLs) have been developed that release their contents much quicker than standard liposomes when increased above a certain temperature. This is accomplished with most TSLs by using dipalmitoyl phosphatidylcholine (DPPC), which converts from solid to liquid phase at 41°C. Combined with the inclusion of micelle-forming lysolipids that form stabilized pores at the phase transition, DOX release can be increased 20-fold[65]. In fact, in experimental work DOX-TSL has exhibited complete drug release within 10-20 seconds at mild hyperthermic temperatures (40-42°C). In pre-clinical studies using DOX-TSL and 42°C hyperthermia in mouse models with flank xenografts of human squamous cell carcinoma, it was seen that DOX-TSL was clearly more effective at achieving tumor growth delay than traditional TSLs, non-temperature sensitive liposomes, and free DOX[65]. The difference in effectiveness was correlated with a significant increase in delivery to the tumor, with a 30-fold increase of free DOX tumor concentration using DOX-TSL over intravenous free DOX [66]. This increased concentration of DOX in the tumor can result in the shutdown of blood flow in the tumor within 24 hours[67]. From these results it is obvious that temperature sensitive liposomal drug delivery can significantly improve the delivery of chemotherapy drugs to tumors while also reducing the side effects. Neoadjuvant use of DOX-TSL in LABC was discussed in the previous section, with

significant doses of heat being significantly correlated with improved pathological response.

### **1.3 Magnetic Resonance Thermometry**

In the previous sections, the benefits of adjuvant hyperthermia with radiation therapy were discussed. What has not been discussed is the need to know the amount of heat delivered to a tumor, or thermal dose. In some trials where invasive temperatures were measured during treatment, retrospective analysis has shown that descriptors of temperatures achieved were significantly correlated with beneficial outcome[68-72].

Initially, successful hyperthermia treatment was thought to be achieved through cell kill due to temperature increase. A temperature  $>42^{\circ}\text{C}$  for 1 hour or more was thought to be needed to achieve significant cell kill, and thus a successful treatment[73-75]. However, studies involving hyperthermia combined with radiation therapy of canine soft tissue sarcomas and human superficial tumors demonstrated that clinical response and local control can be achieved at temperatures below what is required for significant cell kill ( $<42^{\circ}\text{C}$ ). In fact, for most experiments, the temperature was typically in the range of  $40\text{-}42^{\circ}\text{C}$ [76]. These studies demonstrate that the thermal dose is more clinically important than achieving the correct temperature for cell kill.

The dependence of treatment success on achieved thermal dose highlights the need for accurate thermal dosimetry, so that the prescribed thermal dose can be delivered to the tumor. In fact, phase III trials [40, 77, 78] have demonstrated that controlled delivery of thermal dose is clearly related to treatment outcome. However, this control



was only possible with extensive invasive thermometry, which cannot be done in a routine fashion, particularly in deep-seated tumors. Also, information from invasive thermometry suffers from poor sampling of just a few points in the tumor, with little sampling of surrounding tissue. Fortunately, a number of research groups have demonstrated that magnetic resonance (MR) imaging is effective and accurate for noninvasively assessing temperature changes in tissues associated with absorption of nonionizing radiation[79-84]. The methods and challenges of MR thermometry will be discussed in this section. A review of the concepts of acquiring MR images can be found in the appendix.

### **1.3.1. MR Thermometry Overview**

Several methods to measure temperature changes using MR imaging techniques have been developed and demonstrated. These can be separated into two categories of methods, endogenous and exogenous. Endogenous methods rely on the inherent thermosensitive properties of the tissue in the body, while exogenous methods rely on thermosensitive contrast agents to be injected in vivo.

There are three endogenous tissue properties that have been used to measure temperature change, which are (in order of sensitivity) the diffusion coefficient, the T1 (spin-lattice) relaxation time, and the proton resonant frequency shift (PRFS). Overviews of these methods can be found in the literature[85-90]. The diffusion method measures changes in the apparent diffusion coefficient (ADC), which increases with increases of temperature ( $\sim 2.4\%/^{\circ}\text{C}$  [91]). Standard diffusion sequences can be used, with segmented EPI sequences being ideal for body imaging (reference gellermann

paper). The T1 method measures changes in T1, which increases with increases in temperature. Any technique that measures T1 can be used, with T1-weighted GRE or Look Locker sequences being used. Unfortunately, T1-based MR thermometry does not have enough sensitivity to measure the small temperature changes of a hyperthermia treatment. Also, T1-based methods are only linear in a small temperature range (43-45°C [92]) and can suffer from hysteresis due to edema and vasodilation induced in the tissue due to the heat[93]. PRFS methods measure the change in frequency of the water signal, which decreases with increasing temperature change. These changes can be measured in a wide variety of methods that will be explained in detail in later sections. Of the three endogenous MR thermometry methods, PRFS is the preferred, due to the linearity of the frequency change, the tissue independence, and high sensitivity[89, 90]. However, both diffusion and T1 relaxation have advantages that make them useful in specific situations. Both methods can be made less sensitive to B0 field inhomogeneity by using spin echo techniques, while PRFS methods are restricted to sensitive gradient echo methods. T1 measurement relatively motion resistant since images can be registered between measurements, unlike the PRFS and diffusion methods.

However, there are exogenous contrast agents that change thermosensitive MRI parameters with temperature, typically with much higher sensitivity than can be obtained with the endogenous methods described above. Unfortunately, while these contrast agents can provide high temperature sensitivity, many reagents have not been tested in human clinical trials or have been shown to produce reactions in vivo. For example, Zuo et al. have shown that the thulium based complex TmDOTP<sup>5-</sup> has 100-fold the temperature sensitivity compared to PRFS thermometry of water[94]. However, it has

been shown that TmDOTP<sup>5-</sup> cannot be used in human in vivo studies because it causes a slight drop in blood pressure[95, 96]. Thus, endogenous methods are still preferred, specifically PRFS thermometry methods, which will be discussed in detail.

### 1.3.2. PRFS-Based MR Thermometry

As discussed in the previous section, PRFS-based MR thermometry is the method of choice for measuring temperature noninvasively during hyperthermia treatment. The proton resonant frequency shift occurs when the hydrogen bonds in water lengthen with increasing temperature, increasing the magnetic shielding experienced by the water protons by the electrons in the hydrogen bond. This change in the shielding decreases the resonant frequency of the water protons, which results in a decrease in the phase of the water signal, depending on the echo time (TE), as the temperature increases. Fortunately, the frequency changes are linear with temperature, with many in vivo and in vitro experiments showing that most tissues have a sensitivity of approximately 0.01 ppm/°C. These phase changes can be measured by acquiring phase sensitive images using gradient echo or offset spin-echo sequences. The signal acquired from these sequences (in a water-only voxel) is represented in equation 1,

$$s = A_w e^{-TE/T2^*_w} e^{2\pi i TE(\alpha f \Delta T + \psi)} \quad (1.1)$$

where  $A_w$  is the proton density of water, TE is the echo time (ms), T2\* is the relaxation time (ms),  $\alpha$  is the PRFS phase sensitivity (expressed in parts per million per degrees Celsius or ppm/°C), f is the imaging frequency (Hz),  $\Delta T$  is temperature change (°C), and

$\psi$  is the magnetic field offset of the voxel (Hz). Ideally, it would be possible to measure absolute temperature using the phase of an image at one echo time. Unfortunately, phase is also accumulated due to field inhomogeneities, so a reference phase image must be acquired first to determine the initial phase distribution. Then, that reference image is subtracted from all subsequent phase images, resulting in a phase difference image that can be converted to temperature change. The following formula can then be used to calculate temperature change,

$$\Delta T = \frac{\Delta \theta}{2\pi f \alpha TE} \quad (1.2)$$

where  $\Delta\theta$  is the phase difference (radians).

PRFS thermometry has been used for a number of applications. The most widespread use of PRFS has been in the field of thermal ablation. Some of the various tissue ablations that have been monitored with PRFS techniques include prostate[97], uterine fibroids[98], breast fibroadenomas[99], brain tissue[100], bone lesions[101], and esophageal tissue[102]. However, there has also been increasing use in the field of hyperthermia. During hyperthermia treatment, the PRFS thermometry results provide accurate temporal information used for thermal dose calculations and can be used to spatially characterize the heating pattern during the treatment. The PRFS method has been used for thermometry in rectal carcinoma[103] and in soft tissue sarcoma[104].

Unfortunately, using the PRFS method in hyperthermia presents several challenges not typically found in ablation treatments. First, the length of a hyperthermia

treatment is typically much longer than that of ablation, with treatments taking at least 1 hour. This length allows for large errors to occur due to magnet instabilities, mostly from the drift of the main field over time. Secondly, the temperature error must be small, since the optimal treatment temperature is within a small window (41-45°C) and thermal dose is very important. In ablation, temperature error is of less concern since the ablation is typically performed at temperatures much higher than required for tissue necrosis (55-60°C). Also, the extent of the ablated region can often be determined without using contrast agents by using T1-weighted, T2-weighted, or diffusion weighted images[105]. However, there is no reliable method of imaging the extent of the treated region after hyperthermia treatment.

Since smaller temperature measurement error is needed for hyperthermia (41-45°C), the maximum allowable temperature error desired for hyperthermia treatment needs to be defined for the purposes of this dissertation. As discussed in the introduction of section 1.3, the emphasis is no longer on the cell kill percentage achieved at a certain temperature. Instead, the emphasis is on thermal dose. For instance, if during a typical hyperthermia treatment the MR thermometry measures 43°C (the typical treatment goal) when the actual temperature is 42°C (a 1°C error), this may result in a prediction of more cell kill than would actually occur. However, there would still result in a clinical response if a good cumulative thermal dose is delivered. A clinically useful thermal dose can be easily achieved with a 50-60 minute hyperthermia session even if the temperature is 40°C. Thus, while extremely accurate thermometry is not mandatory to determine if the tumor exceeds a cutoff temperature for cell kill, it is needed for prediction of treatment success using thermal dose. The thermal dose delivered can be improved with

MR thermometry, where you can get spatial data of the temperature throughout the entire tumor. Thus, temporal and spatial accuracy of thermometry becomes more important than temperature accuracy at each time point. Using this information, it was determined that a 1.0°C temperature error (averaged over the region of interest, such as a tumor if possible) is a reasonable goal for this dissertation and for non-invasive MR thermometry in general.

### **1.3.3. Complications of PRFS Thermometry due to $B_0$ Field Drift**

As mentioned previously, large errors can occur when the main magnetic field ( $B_0$ ) drifts significantly during scan time, creating significant non-temperature related phase shifts in water. These phase shifts due to field changes are inseparable from phase changes due to temperature using traditional PRFS methods, resulting in error in temperature measurement. A maximum specification of the rate of magnetic field drift in a modern commercial MRI system magnet is 0.1 ppm/hour, or approximately 6.4 Hz/hour at 1.5T. The resonant frequency of water also changes at -0.01ppm/°C, or 0.64 Hz/°C at 1.5T, meaning that an hour long hyperthermia treatment could have up to 10°C of temperature error due to  $B_0$  drift, alone, if not corrected. Considering that the maximum amount of temperature change for a typical hyperthermia treatment is between 6-8 °C, field drift could be a significant problem for accurate measurement of temperature change.

Fortunately, several methods have been developed to correct for field drift error. Many attempts have been made to correct for drift inside the tumor and surrounding tissue. One approach is to provide reference materials in the image that change phase

with magnetic field drift but do not change phase with temperature. De Poorter, et.al. were the first to place water gelatin references around a phantom and linearly extrapolate the phase changes due to B0 drift from the references to inside the phantom[106]. El-Sharkawy and colleagues used a saline filled hose around a phantom as a reference material and used a least squares fit of measured field changes in the saline to interpolate the field change inside a gel phantom[107]. Finally, Wust and Gellermann have used similar interpolation methods but instead used body fat or external water as the reference material[103, 108, 109].

While all of these methods have been shown to be effective in correcting for substantial B0 drift, there have been several issues that have not been thoroughly examined. First, while De Poorter and colleagues have looked at field correction with three references in the legs of human volunteers, there has been no investigation into whether using more references will improve correction or how well such references perform inside a hyperthermia applicator. Also, De Poorter showed results from only one leg experiment, which showed large temperature errors, that were never resolved. El-Sharkawy and colleagues did perform phantom experiments in a hyperthermia applicator. However, they did not perform in vivo experiments and their temperature correction was insufficient due to use of a short TE difference for their field measurement. Additionally, De Poorter and El-Sharkawy both used water-based reference materials, for which the phase has large temperature dependence. Our experiments use silicone oil as a reference, to effectively eliminate this dependence and allow for references to be placed in a heated water bolus. Lastly, the fat referencing method used by Gellerman and Wust has some potential error due to the presence of a variable percentage of water in adipose tissue,

which can limit the effectiveness of that approach when there is not enough ‘pure’ fat to get a suitable sample region.

In summary, there have been many methods developed to correct for the field drifts seen during hyperthermia treatments. Unfortunately, none of these methods are robust, with many of the methods allowing temperature errors due to temperature changes. Therefore, a robust method needs to be developed and optimized to correct for these field drifts.

#### **1.3.4. Complications of PRFS Thermometry in Fatty Tissue**

While the PRFS method is effective in tissues that are mostly water, there can be significant error in tissues containing even small amounts of fat. The error stems from the negligible phase sensitivity of fat with temperature (0.000045 ppm/°C for pure vegetable oil[110]), due to the lack of hydrogen bonds present. Most fat tissue contains small amounts of water (<20%), so there will be some phase change due to temperature. However, that phase change will be significantly less than that expected for tissue containing mostly water (muscle). While it is still possible to calculate a phase sensitivity value using the phase changes observed, it will be heavily dependent on the fat-water ratio of the tissue. A simulation of a voxel containing fat and water was performed by adding temperature related phase changes to water and calculating temperature from the overall signal phase change over time for a constant TE sampling value. This was done for the entire range of possible fat-water ratios, with the results shown in Figure 1.4. As seen from the figure, there is an almost linear relationship between fat-water ratio and the percent temperature error. Unfortunately it is difficult to



exploit this since it would be far too time consuming and inaccurate to measure the fat-water ratio and calibrate the temperature measurement before treatments.

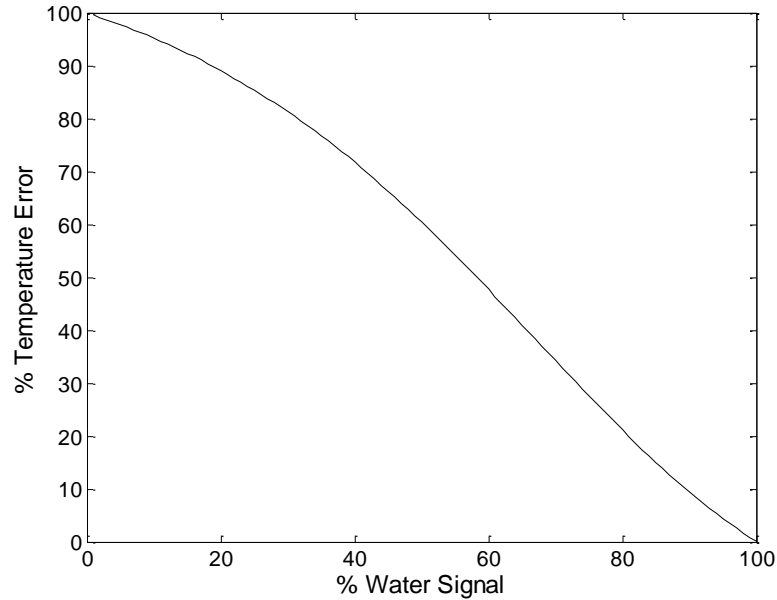


**Figure 1.4:** Percent temperature error vs. percent water signal for a simulated fat-water voxel. This diagram demonstrates the large errors that can occur when fat is present in a voxel.

There have been many attempts to solve this problem, many of them focused on separating the water and fat signals and measuring their independent phase changes. One method involves the suppression of the fat signal so that only the water signal is measured[111]. Unfortunately, the fat signal cannot be completely eliminated due to multiple resonance peaks present in fat and inhomogeneity of the B0 field over the volume of interest. Another group has used multiple echoes to average the error due to fat, thus resulting in a lower overall temperature error[112]. However, this method only works for phantoms of 20% fat or lower. Another group has used the change in signal intensity due to changes in the T1 relaxation time to measure temperature in fatty

tissue[113], but it is very tissue specific and sensitive to system drift. Additionally, several groups have measured the frequency difference between the fat and water peaks using spectroscopy[111, 114, 115]. Since both the water and fat peaks change frequency with changes in the B0 field, only measuring the water frequency change will result in error due to B0 drift. Thus, measuring the frequency difference of water relative to fat provides a correction for the drift, since the frequency difference will be solely dependent on temperature change. Drawbacks to this method typically include long scan times, poor spatial resolution, and dependence on a good shim. Fat suppression methods attempt to eliminate the fat signal so that only the water signal is measured [116, 117]. Unfortunately, the fat signal cannot be completely suppressed due to the multiple resonance peaks present in fat (particularly the olefinic peak near water) and inhomogeneity of the B0 field over the volume of interest. Lastly, intermolecular quantum coherence phenomena have been used to determine the frequency difference between fat and water [118]. While this method is promising for measuring absolute temperature, it still requires significant research to make it clinically useful.

Therefore, while many methods have been developed to measure temperature in fatty tissue, there has not been sufficient development of a method that will measure temperature of hyperthermia treatment of LABC in a timely and accurate manner.

### **1.3.5. Complications of PRFS Thermometry due to Motion**

Image artifacts occur when the object being imaged moves during acquisition. While registration algorithms can correct for most bulk motion, there are several motion induced artifacts that cannot be corrected with registration. In the phase direction,

motion artifacts manifest as periodic replications (or ghosts) of the moving tissue. In the readout direction, the moving tissue is displaced in the image in proportion to the velocity of the motion. However, in addition to these artifacts, B0 field changes can occur due to the motion of tissue. These changes occur due to changes in the distribution of magnetic susceptibility due to the new position of tissue. The field changes can occur at distant locations from the source of motion. Some of the most common motion-induced field changes occur due to breathing and cardiac motion. The field changes induced by these phenomena can occur at locations distant from the source of motion. These field changes then result in phase changes in the images, which in turn result in temperature error when using PRFS thermometry methods. Breathing motion has been shown to induce field changes in the brain[119-121], breast[122-124], and abdomen[125]. The effects on the B0 field due to breathing have also been simulated by several groups[126-128]. In the breast, average field changes of 0.14ppm and maximum changes of 0.4ppm near the chest wall are seen between expiration and inspiration. At 1.5T, these would equate to approximately 36°C and 104°C, respectively.

Many techniques have been developed to help correct for these phase changes. Many methods involve averaging or fitting of the k-space data[119, 129], but these methods require complex operations on the raw scanner data and also suffer from low signal-to-noise ratio (SNR) in k-space compared to image space. Real-time adjustment of the field (shimming) has also been used[130], but not feasible due to the nonlinear nature of the field changes and the limited availability of 2<sup>nd</sup>-order active shimming. Additional approach include field change estimation from calculating differences in tissue position[131] and use of navigator echoes for respiratory gating[132-134]. Also,

phase correction using reference images taken at multiple stages of the breathing cycle[124, 135] can be used to perform respiratory gating. However, many of these respiratory gating methods require short imaging acquisitions, signal acquisition near the diaphragm for use in determining respiratory position, and may not correct for complex lung movement. Lastly, a method using phase references from the surrounding non-heated tissue extrapolates phase correction into the heated tissue[136, 137].

Unfortunately, the method uses phase from the surrounding fat and water, which will have phase changes due to the temperature increase in hyperthermia treatments. Even the fatty tissue will have phase changes due to its small water content.

Thus, while many correction methods have been developed, none of them would sufficiently correct for the field changes experienced in the breast during hyperthermia treatment of LABC.

## **1.4 Overview**

### **1.4.1 Objectives**

Because of the importance of improving treatment for breast cancer and the promise of adjuvant hyperthermia, the present work is focused on developing a comprehensive approach to hyperthermia cancer therapy in the breast. To perform hyperthermia of LABC, two important components are needed: an applicator to heat the tumor and accurate thermometry of the heat distribution. Before the start of this dissertation, a RF applicator for hyperthermia of LABC was developed and clinically used at Duke in the Radiation Oncology Department[42, 56]. However, this applicator was not fully MR compatible. Also, the patient support system was unusable in the MR

due to size limitations and ferrous material. Thus, our initial objective was to modify the applicator to be MR compatible and to allow for attachment of a new patient support system that will fit in the MR bore while providing superior patient comfort. Chapter 2 describes how this system was modified. Also, oil references were added to allow for accurate temperature imaging using standard PRFS imaging in the presence of field drift.

The complications of performing MR thermometry in the breast have been discussed previously. While many MR methods have been developed for noninvasive thermometry of hyperthermia treatments, there are still several hurdles. Since the effectiveness of hyperthermia treatment is heavily dependent on the applied thermal dose, these difficulties need to be addressed to provide optimal treatment of LABC. Therefore, a method was developed for correcting for  $B_0$  field drift using external oil references that surround the object of interest. This method extrapolates the phase changes in the oil references to the entire image, then uses those extrapolated values to correct for phase changes in vivo. While oil reference field correction will still have large PRFS temperature errors in fatty tissue (due to low water content), it should be effective when used in water-rich glandular and tumor tissues. This method was evaluated by imaging in vivo and in phantoms without temperature change during periods of moderate  $B_0$  drift. The variation of the temperature change (nominally zero) after correction can be used to estimate the error of the technique. This method is discussed in detail in Chapter 3.

As discussed in section 1.3.4, large errors are seen in PRFS thermometry of fatty tissue. To address this, new methods were developed to measure temperature in fatty tissues. These methods were then analyzed to determine their bias and optimal scan parameters. IDEAL fat-water separation method[138] can be used to calculate

temperature in fatty tissues, but it results in large errors in the  $B_0$  field measurement as well as bias in the temperature estimate. Thus, a new nonlinear method of separating fat and water was developed for replacement of the linear IDEAL method. Heating experiments were performed on fat-water gelatin phantoms to validate the methods. Also, the best imaging parameters (such as echo time and number of echoes) needed for minimal temperature error were determined using simulations and imaging experiments with fat-water phantoms. These methods and their results can be found in Chapter 4.

Since IDEAL and other methods require multiple images to perform fat-water separation properly, imaging time can be long. For initial experiments, each image was acquired separately due to the lack of a commercial multi-echo sequence. Thus, a pulse sequence was programmed to acquire multiple gradient echo images within one repetition time (TR) period. It was then tested on phantoms and compared to our traditional methods, resulting in approximately a 300% decrease in imaging time. The pulse sequence data can be found in Chapter 5.

Lastly, a method was developed to correct for phase changes in the tumor between breath holds. As discussed in section 1.3.5, breathing creates significant phase changes in the breast. Due to the number of images and SNR required for our thermometry methods to work, it is difficult to acquire data without large phase changes, whether triggered or not. Thus, it was decided that images would be acquired during breath holds, to minimize phase changes. Unfortunately, phase changes are still present between breath holds, which are interpreted as temperature changes. While this does not pose a problem for thermometry in the fatty tissue, it creates significant temperature error in the water-rich tumor, where the fat-water thermometry methods discussed in Chapter 4

fail. Therefore, we developed a new method for correcting these phase changes using the B0 maps from the fat-water separation methods discussed in Chapter 4. The field changes of the B0 maps inside the breast are converted to phase changes and extrapolated to the inside of the tumor for correction, similar to the method used in Chapter 3. PRFS thermometry is then used to measure temperature in the tumor, with correction from the measured phase changes. These experiments are presented in Chapter 5.

In summary, the hardware developed in Chapter 2 will be used to heat LABC inside the MR scanner bore. The fat-water separation methods developed in Chapter 4 will be used to provide accurate thermometry in the fatty tissue. Traditional PRFS thermometry combined with the oil reference methods developed in Chapters 3 and 5 will be used to perform accurate thermometry in the water-rich tumor.

#### **1.4.2. Significance**

The overall objective of this dissertation is to create a complete system of hardware and software to enable accurate thermometry of the hyperthermia treatment of LABC. The combination of the new fat-water imaging method and the oil reference correction method will reduce the error seen in MRI thermometry of both fatty tissue and the tumor. With accurate noninvasive thermometry, HT treatments of LABC can be performed with knowledge of the temperature in the entire breast. This knowledge will allow for optimal heating of the tumor with as little heat in the surrounding tissue as possible, which will not only improve the results of the hyperthermia treatment but also allow for optimal release of DOX-TSL liposomes. With these improvements, HT of LABC can be further validated and correlated with heat delivery, which could promote its use in standard

therapy. A clinical trial is planned to start in sometime in 2011 using this system to perform HT of LABC.

The work performed for this dissertation is not only applicable to HT of LABC. The oil reference correction methods developed are applicable for B0 drift correction of the HT treatment of cancers located in many other regions of the body, including the leg, arm, and abdomen. Also, all of the thermometry methods developed could be used for LABC ablation or other thermal procedures.



## **2 System for Hyperthermia Treatment of Locally Advanced Breast Cancer**

### **2.1 Introduction**

#### **2.1.1. Need for an improved treatment system for use in the MRI scanner**

An applicator was developed to perform hyperthermia of LABC while the subject was being imaged in the MRI system. The applicator was based on a pre-existing design for breast hyperthermia outside of the MRI system. An advantage of this approach is that an IDE (FDA Investigational Device Exemption) had already been obtained for this pre-existing system and thus approval for use of a modified design could be expected to be more timely. Thus, the modified design, for use in the MRI system, is tuned for 140 MHz and contains five twin-dipole antennas. The pre-existing applicator was used for treatment of patients outside of the MR on a bed with memory foam placed around the applicator. This was reasonably effective at keeping the patient comfortable during treatment, even though there was still pain in the chest of the patient over time due to the rectangular shape of the applicator. Since the pre-existing bed was too wide to fit into the magnet, an unmodified GE MR bed was acquired and the default curved table insert was removed. A custom polycarbonate table insert was then made to provide a flat surface to support the applicator and patient. A large rectangular hole was also cut into the table to allow for the breast applicator to sit as low as possible in the MR bore, providing as much space as possible for the patient. A custom memory foam pad similar to the one used outside the MR system was made to fit inside the MR bore and around the applicator. This support system can be seen in figure 2.1.

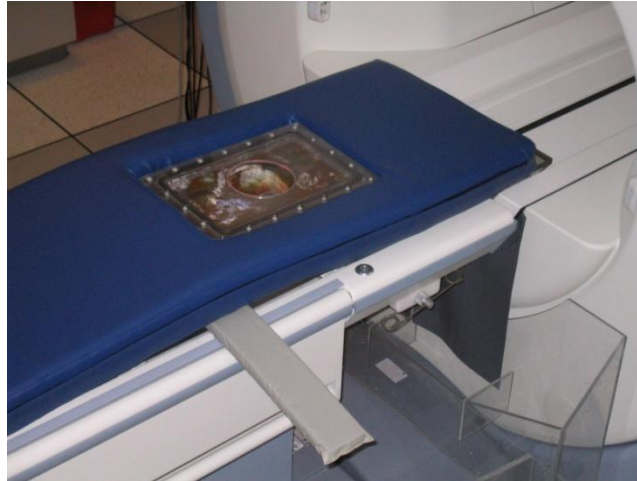


**Figure 2.1:** First prototype of the patient support system. Notice how the applicator is centered and there is little padding around the edges of the applicator, both of which resulted in discomfort.

A comfort study was performed with 10 subjects, each lying in the MR bore on the support system for 60 minutes. While all subjects were able to lie inside the bore for the entire 60 minutes, there was still significant pain and discomfort reported by almost all subjects. In particular, they reported significant pain near their breast bone and a sensation that they were about to fall off of the applicator. This pain and discomfort could be a problem during an actual hyperthermia treatment since it can result in patient movement or early termination of the treatment. Lastly, the applicator is centered directly in the center of the table, with no preference for either side given to the patient. This contributed to the feeling of unsteadiness and lack of support among the subjects.

Therefore, a new patient support system was developed that can easily fit into the MR bore while keeping the patient comfortable. Due to the size of the applicator, the MR breast imaging coils normally used for MR breast imaging (to provide high quality images) could not be used for patient support and imaging of the breast during heating. Thus, a new set of imaging coils were developed specifically for this applicator. Lastly,

modifications needed to be made to the breast applicator to accommodate the new support system and make it MR compatible and to incorporate oil references for magnetic field drift correction.

### **2.1.2. Need for Local MR Imaging Coils**

Due to the inability to use any commercial breast coils with the breast applicator, the body coil is the only other coil available to image the breast during treatment. However, the SNR of the body coil is not sufficient to allow for accurate thermometry in the breast during breath holds, since the scan time must be short (10-20 seconds for 3 images when using fat-water separation methods). Improved SNR can be achieved by developing MR surface coils that are situated in close proximity to the breast. Thus, two MR surface coils were developed that attach to the sides of the breast applicator and tested to determine the SNR improvement that they provide over the body coil.

### **2.1.3. Evaluating the New Treatment System**

The new treatment system needed to be evaluated to determine if it provided appropriate patient comfort, allowed for adequate positioning and support of the breast inside the applicator, and provided adequate SNR for thermometry. The comfort and support of the system was determined during a 10 subject comfort study using healthy female volunteers from a wide range of ages. The SNR improvement of the system using the custom MR surface coils was determined using phantom experiments. These evaluation studies as well as the construction and design of the system will be discussed in this chapter.

## **2.2 Experimental Methods**

### **2.2.1. Modifying the Breast Applicator for use in the MR Scanner**

An early configuration of the breast applicator is shown in Figure 2.1. When tested in the MR, severe signal dropout was seen in half of the applicator due to ferromagnetic springs in the valves for the water connections. Also, it was found that the applicator was not airtight, losing significant amounts of air within an hour of filling. To fix these issues, the ferrous valves were connected approximately 2 feet from the applicator using new plastic connections and tubing to the applicator. The applicator was then made airtight by applying a layer of silicone RTV to all of the glue joints of the applicator.

To allow for attachment of the support system, the flange around the top of the applicator was extended in all directions. The o-ring system was improved to allow for a better seal and threaded holes were drilled into the flange to allow for attachment of the support system.

Oil references were then added to the interior and exterior of the applicator. Two circular references were added to the interior, each approximately 0.5” in diameter. Three plastic clips were glued to the bottom of the inside of the applicator for each reference to allow for them to be temporarily attached onto the applicator. The two exterior references were attached to the underside of the top flange on both sides of the applicator. Each reference was made of polycarbonate and was filled with silicone oil (Thomas Scientific #6428R25).

Lastly, in previous experiments with the breast applicator, it was found that the silicone bolus was too tightly sealed. This resulted in the bolus pushing into the breast and flattening it when trying to fill the applicator. Thus, a larger silicone bolus was made to allow for it to conform to the breast much more than the previous bolus.

### **2.2.2. Construction of the New Patient Support System**

The new patient support system was developed using the same GE bed and custom polycarbonate insert used in the initial system discussed in the chapter introduction. The main idea behind the new support system was to distribute the weight of the patient evenly across the top of the applicator, to prevent the occurrence of pressure points. This was done through the use of a plastic mold that was made from the surface of a 3T commercial GE breast coil using plaster and the Duke Prosthetics Shop. A 3D model of the breast coil used as the mold is shown in Figure 2.2. Two molds were made, one for each breast. For each mold, one side of the mold was flattened and a hole was made so that the breast can drop through it into the breast applicator. The plastic around the mold was then partially melted with heat guns and pressed with molds so that the plastic slowly slopes downward into the hole. This was done for patient comfort and to allow for maximum protrusion of the breast into the applicator.

The mold and breast applicator were then modified so that each mold could screw into the top of the applicator in eight places. A thin plastic breast cup designed for immobilization of the breast for radiation treatment was secured between the applicator bolus and the hole of the plastic mold. The cup functions not only to immobilize the breast but to also prevent the bolus from compressing the breast. A custom pad of half-

inch thick memory foam was created with a hole on one side that is slightly smaller than the hole in the patient support. It can be flipped around to allow for use with both molds (and thus treatment of either breast). Lastly, Bionix vacuum bags (Bionix Development Corporation, Toledo, OH) were placed underneath the torso portion of the support structure to provide rigid support for the applicator and plastic mold. Pictures of the final patient support system setup are shown in Figure 2.5.

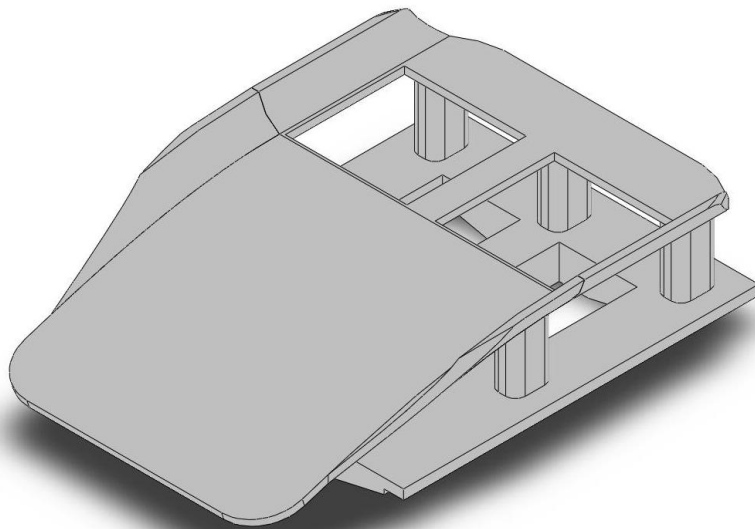


**Figure 2.2:** 3D model of the GE breast coil used as a mold for the patient support. The top portion was used for the mold.

### **2.2.3 Construction of local MR imaging coils**

To build the coils, two 1/8" thick acrylic sheets of approximately 8.67" x 4" were made. These allow them to fit on the sides of the breast applicator between the gussets that hold up the top flanges. Then, custom holders were machined out of acrylic to attach

the coils onto the breast applicator gussets. These work by having slots for both the coils and the gussets. There are then screws that protrude into those slots, clamping the coils and gussets into the slots. The holders allow for the coils to be rigidly held as close to the applicator as possible, which will result in maximum SNR and a consistently matched coil. A diagram demonstrating the size of the coils and how they attach to the applicator is shown in Figure 2.3.

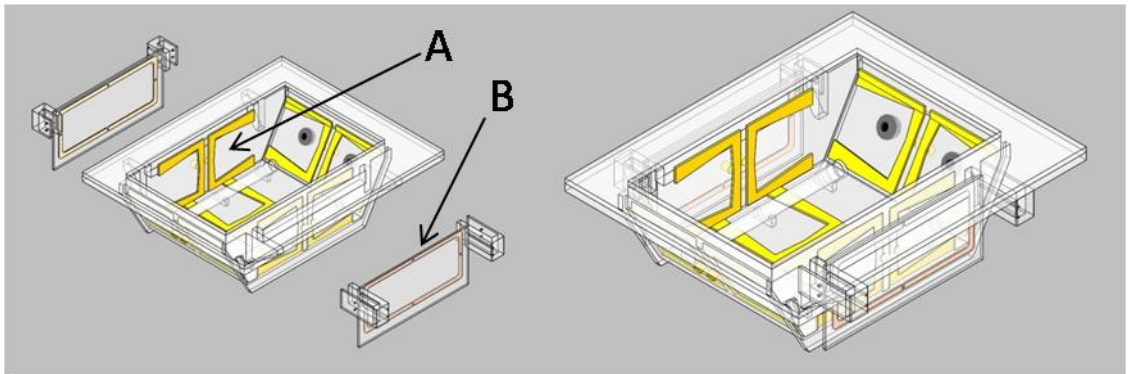


**Figure 2.3:** Diagram detailing the size and positioning of the coils on the breast applicator using the custom holders. (Left) Coils before placement on the applicator (Right) Coils after placement on the applicator. Notice the holders on the side of the coils, which slide onto and screw into the applicator, securing the coils in place as close as possible to the applicator. The RF heating antennas are labeled as (A) while the MR imaging coils are labeled as (B).

Initially, two prototype coils (3.3"x7.5") were made using 0.25" wide copper tape. A schematic of the coil can be seen in Figure 2.4. Once those were made, similar MR coils were made with by etching copper on PCB boards. MR compatible ceramic capacitors were placed at four equidistant locations along the coil and were adjusted to make the coil resonant at approximately 63.85 MHz, the frequency of the NMR signal at 1.5T. A variable capacitor (Voltronics Corporation, Denville, NJ) (C1) was placed in parallel with one of the RF capacitors (C2) to allow for easy tuning of the resonant frequency. Another capacitor (C4) was chosen as the matching capacitor. Connecting

between matching capacitor and the center conductor is an inductor. While both the matching capacitor and the inductor can be adjusted to affect the match of the coil, they also serve the purpose of contributing to the transmit block of the coils.

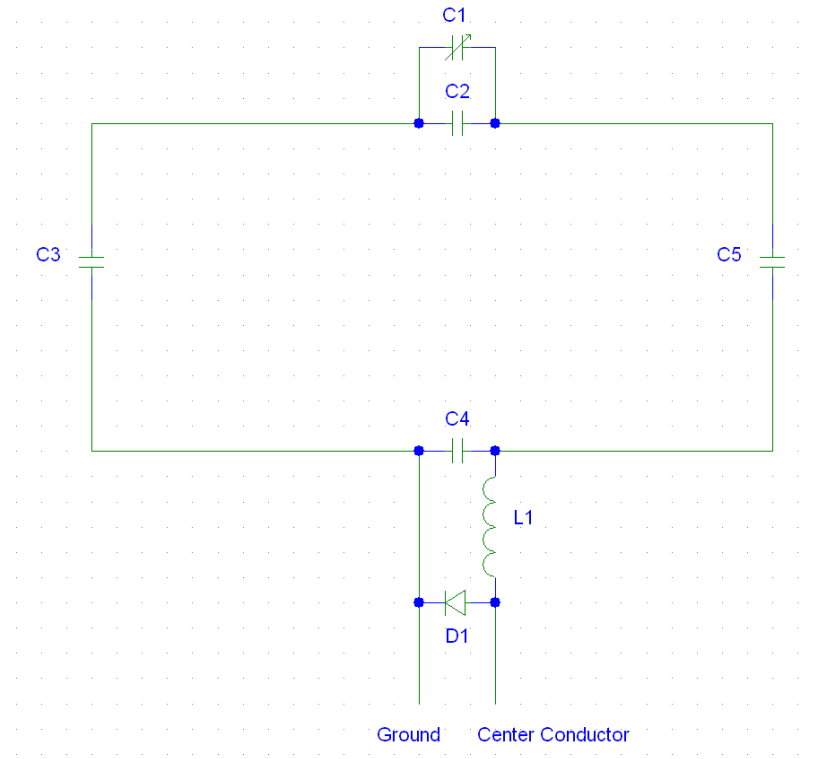


**Figure 2.4:** Schematic of the MR imaging coil

Many coils both transmit RF (to produce the B1 excitation field that flips the spins) and receive the resulting MR signal, which are known as transmit-receive coils. While this can reduce noise, it can result in poor B1 field homogeneity, which will affect the signal and phase across the volume. Better spatial homogeneity of the signal and phase can be obtained by transmitting the RF pulse with the body coil and receiving the MR signal with a local MR coil. In this case, the local coil must be detuned during the transmit portion, to prevent damage to the coil due to the large energy of the body coil



transmit and prevent local heating of the imaging subject. For the coils developed for this thesis, an active diode block was used. This involves adding a PIN diode (D1) between the ground and center conductor, which is turned on by a 15 V DC signal (already supplied by the MRI system) that is transmitted through the center conductor during the body coil transmit. The diode then creates a short, which creates a loop between C4 and L1. If C4 and L1 are resonant, then a resonant loop is created which increases the impedance of the larger coil loop. This prevents large currents from circulating in the coil during the transmit pulse.

To tune and match the coil, the applicator was filled with D<sub>2</sub>O until the bolus surrounded a phantom made of a 100% water gelatin and 0.9% salt. The coils were then secured to the applicator and the antenna reflection coefficient (S<sub>11</sub>) of each coil was measured. The tune and match process involved adjusting the match capacitor and inductor so that they were resonant but also providing a match close to 50 ohms. However, when the matching capacitor is adjusted the resonant frequency of the coil changes. Thus, the other capacitors in the coil needed to be adjusted to set the resonant frequency back to 63.85 MHz. Unfortunately, this changes the match of the coil, which must be corrected by changing the matching capacitor and inductor. This process is repeated until the coil is matched to 50 ohms and is resonant at approximately 63.85 MHz. The final values of the components are shown in Table 2.1. The value of L1 is an approximation since it is a variable inductor (#165-02A06L, CoilCraft, Cary, IL) near one of its bounds. The value of C1 was also approximated since it is a variable capacitor (#NMAP15HV, Voltronics Corporation, Denville, NJ).

**Table 2.1:** Component values for the local imaging coils

	<b>Coil 1</b>	<b>Coil 2</b>
<b>C1</b>	~10 pF	~10 pF
<b>C2</b>	47 pF	47 pF
<b>C3</b>	51 pF	56 pF
<b>C4</b>	51 pF	56 pF
<b>C5</b>	220 pF	235 pF
<b>L1</b>	~25 nH	~25 nH

To test the active block, the coils were placed in close proximity to each other. The S11 of the coil not being tested was measured while a DC voltage of 1V was applied to the coil being tested. Without the DC voltage the S11 of the other coil would have split peaks due to coupling of the two coils. However, with the DC voltage applied the S11 becomes one peak due to the activation of the active block on the coil being tested.

To determine the SNR of the new coils and compare them to the body coil, a spherical phantom containing homogenous 100% water gelatin was placed into the breast applicator that had been partially filled with D<sub>2</sub>O. The phantom was then imaged using the new breast imaging coils with one slice near the center of the phantom and applicator. An SPGR sequence was used with parameters TE=20ms, TR=34ms, FOV=28cm, BW=15.64 kHz, slice thickness = 5mm, and NEX = 4. A sequence that acquires many gradient echoes in one TR period (discussed in detail in Chapter 5) was also used with TE = [15.4,21.8,28.2], TR=50, FOV=28cm, BW=15.64 kHz, slice thickness = 5mm, and NEX=2. The local imaging coils were then removed and a similar slice of the phantom was then imaged with the same sequence, except this time using the body coil.

#### **2.2.4. Evaluation of the Treatment System with Volunteer Comfort Study**

To assess the performance of the new patient support system, a volunteer comfort study was performed. Volunteers were recruited and the study was conducted under a Duke University Medical Center IRB approved protocol (IRB#PRO227). A new comfort study has now been started to assess the effectiveness of the new patient support system with healthy volunteers. A total of ten subjects were proposed, and ten volunteers have been enrolled. Of those ten volunteers, five volunteers placed their left breast in the applicator while the other five placed their right breast in the applicator. Before the volunteer entered the MRI suite, the custom MR bed was attached to the MR bore and clean sheets were draped over the support system. A pillow was placed at the front of the applicator for the patient to rest their head and arms on comfortably. The applicator was then partially filled with D<sub>2</sub>O until the bolus surrounded the plastic breast cup. Lastly, a flattened plastic turkey oven roasting bag (Reynold's Oven Bags, Turkey Size) was placed over the plastic cup to prevent contact between the subject and the cup itself, to maintain a hygienic environment in the applicator.

Once the system was set up properly, the volunteer was brought in and situated on the applicator. The subject then adjusted their own position on the applicator until their breast was comfortably positioned in the breast cup. Once positioned, the volunteer was moved into the MR bore using the MRI system's positioning system and localizer scans were performed to determine the exact position of the volunteer's breast inside the cup. Next, a MR protocol was performed to image the breast and determine its fat-water content. This information was acquired to determine an average fat/water signal ratio in the fatty and glandular tissues. The average value can then be used for simulations, such

as finding the expected temperature noise that will be seen during a treatment. A table containing all the scan parameters and on which subjects they were performed can be seen in the appendix. The protocol is split up according to volunteer number, since the protocol was changed slightly due to technical problems early in the study and time constraints for certain volunteers.

The volunteers comfort and willingness to continue the study was vocally checked through the MR intercom system approximately every 15 minutes. After approximately 60-70 minutes, the volunteer was removed from the MR bore and the support system. The support system was then drained of D<sub>2</sub>O and removed from the MRI suite. Lastly, the volunteer was asked to fill out a questionnaire to determine their comfort during the study and where they felt any discomfort. A copy of the questionnaire can be found in the appendix.

## **2.3 Results**

### **2.3.1. Changes to the Breast Applicator**

Pictures of the modified breast applicator and the added oil references can be seen in Figure 2.5.

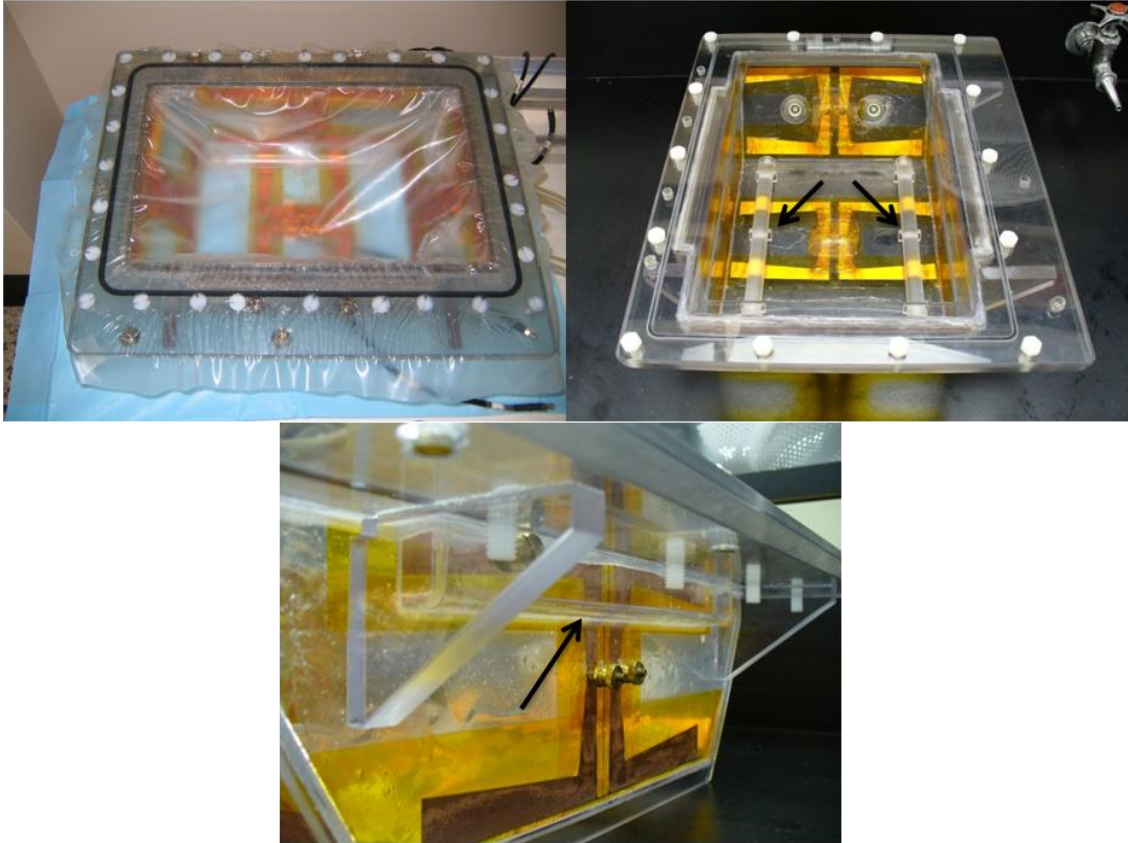


**Figure 2.5:** Pictures of the modified breast applicator. The top left image shows the breast applicator after modification. The top right image shows the two references added to the inside of the applicator. The bottom image shows one of the two references added to the outside of the applicator. The oil references are indicated by black arrows.

### 2.3.2. Final Treatment System and Comfort Study Results

A picture of the final treatment system in various stages of assembly is shown in Figure 2.6.

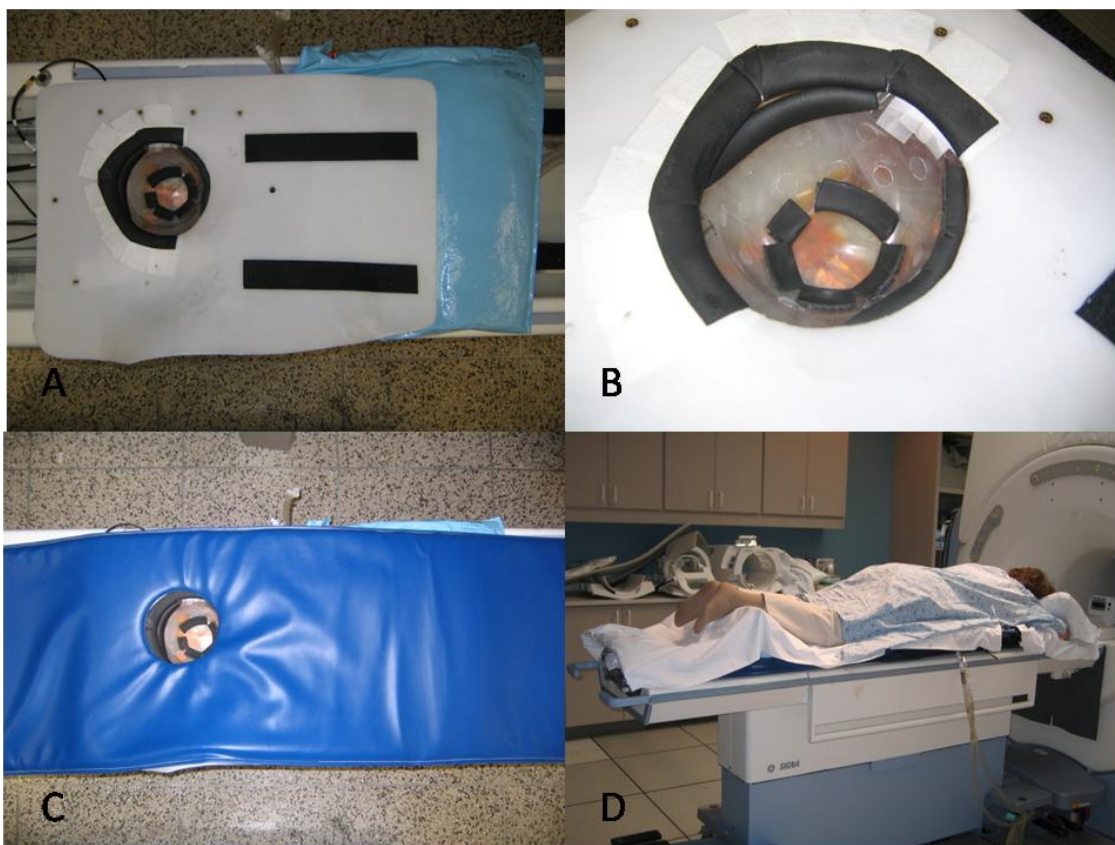


**Figure 2.6:** Pictures of new patient support system (A) Applicator with plastic mold attached in position with Bionix support bag underneath. (B) Close-up view of the breast cup used to contain the breast is attached in the center of the applicator. (C) Support system assembled with the large foam pad on top. (D) Comfort study subject lying on the bed before being inserted into the bore of the MRI system.

All ten of the volunteers were able to lay on the support system inside the MRI system for approximately 60-70 minutes. The responses to the questionnaire are compiled in Table 2.2. We were unable to get responses from subject #2. Most comments given were about back, shoulder, and opposite breast pain that were all most likely caused by the extended time in the prone position. Most shoulder discomfort was caused by the subject not realizing that they could reposition their arms if necessary. Also, subject #10 complained of numbness of the hands, but acknowledged that it would have been alleviated by repositioning her arms. Some subjects discussed some discomfort in the

sternum, but it was of much less magnitude than what was reported with the previous support system. However, all of these discomforts were relatively minor, with no strong pain being reported. As seen in Table 2.2, not one subject reported a pain level of greater than 2, which was deemed as “a little” pain. It is also worth noting that subject #8 was most likely uncomfortable with the MR scan itself, citing discomfort at being in an enclosed space and the loud noises making her tense. Despite these discomforts, several subjects fell asleep for prolonged periods during the comfort study. Adjustments made to the slope of the hole in the mold eased some of the chest discomfort felt by many volunteers earlier in the study. Finally, the combination of the loose bolus and the plastic breast cup helped secure the breast in a good position but also prevent it from becoming compressed by the water bolus.

**Table 2.2:** Breast Comfort Study Questionnaire Responses. The mean data shows that on average, the volunteers found the system comfortable (4 was listed as comfortable for Question 1) and only small amounts of pain were reported.

Volunteer #	Question 1	Question 2	Question 3	Question 4	Question 5
1	5	2	2	4	2
2	n/a	n/a	n/a	n/a	n/a
3	5	2	1	4	2
4	6	2	1	4	1
5	5	1	1	3	2
6	3	2	1	3	4
7	3	2	1	3	1
8	3	2	2	4	3
9	4	2	1	4	3
10	5	1	2	4	1
<b>Mean</b>	4.33	1.78	1.33	3.67	2.11

### 2.3.3. MR Results of the Comfort Study

The individual fat and water images processed using the IDEAL algorithm (discussed in Chapter 4) are shown in Figure 2.7 for the right breast of volunteer #6, along with the anatomical sagittal and axial images. Two other sets of water and fat images are shown for volunteers #7 and #9 in Figure 2.8.

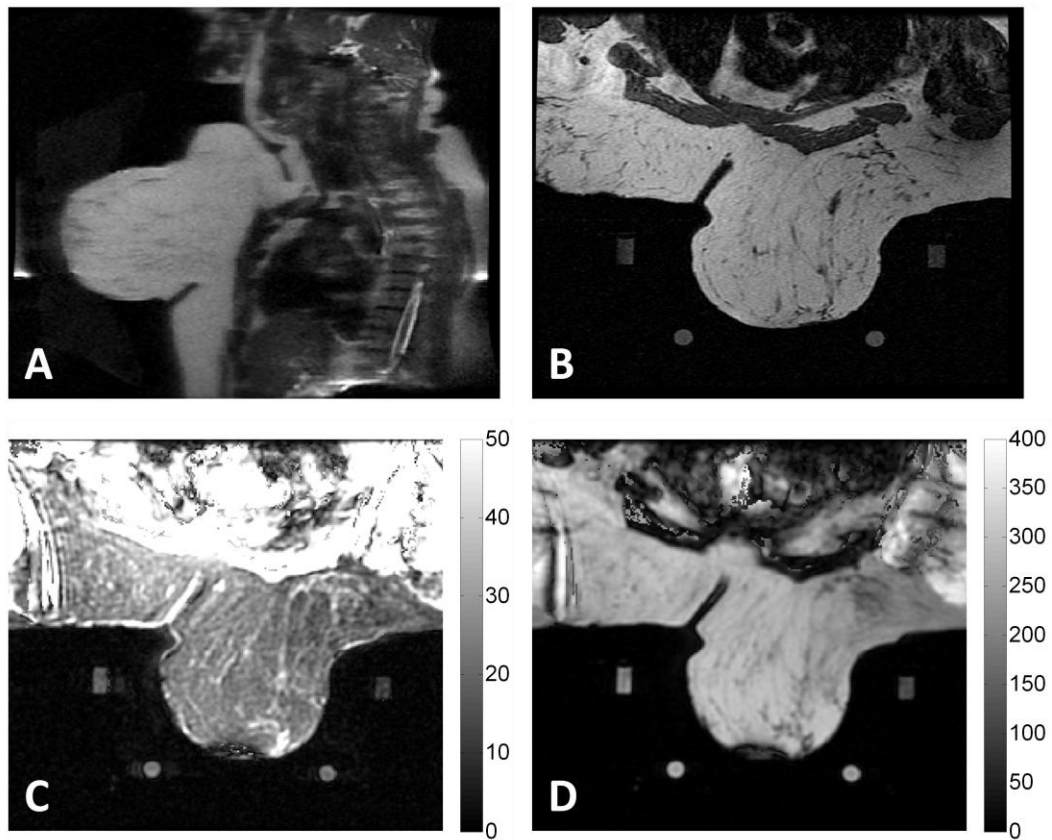


**Figure 2.7:** (A) Sagittal image of the right breast of subject #6 in the applicator. The subject's head and neck is at the top of the image (B) Axial image of the breast in the applicator. (C) Water signal in the axial image of the breast. (D) Fat signal in the axial image of the breast. Images (C) and (D) demonstrate that the water-fat separation is reasonable.

The water signal percentage (as a percentage of the fat and water signal combined) was then calculated in the fatty and glandular tissue for each volunteer. The values in the



glandular tissue were only calculated when a clearly defined region of glandular tissue could be found in the image. These results can be found in Table 2.3.

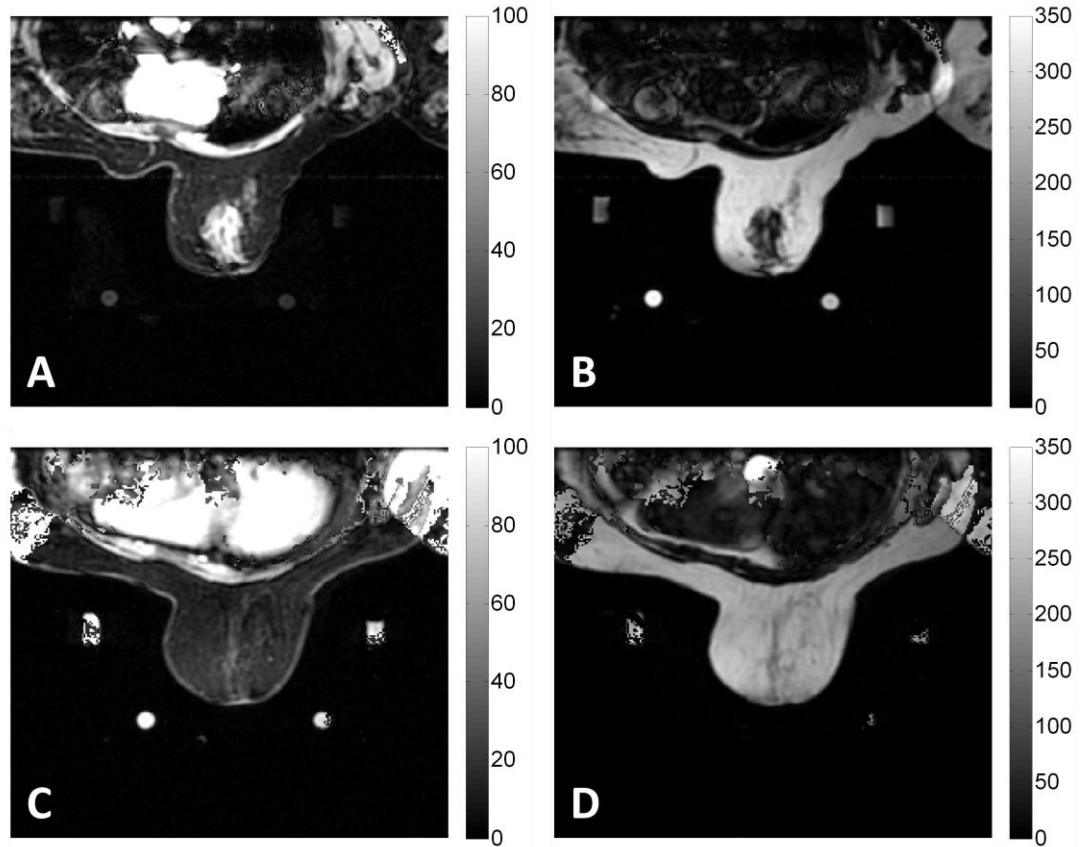


**Figure 2.8:** (A) Water signal in the axial image of the right breast of volunteer #7. (B) Fat signal in the axial image of the breast of volunteer #7. (C) Water signal in the axial image of the breast of volunteer #9. (D) Fat signal in the axial image of the breast of volunteer #9. The water and fat images are from sequence #9 in the comfort study protocol. All images show that the water-fat separation during the comfort study is reasonable and that the water signal is very low in the fatty tissue.

**Table 2.3:** Water signal percentage values calculated in the fatty and glandular tissue of the breast. Values in the glandular tissue are not shown when the volunteer did not have a clearly defined region of glandular tissue. Volunteer #6-10 use an equivalent TE = 7.8ms while volunteer #5 uses an equivalent TE = 16.6 ms. These results show that the fatty tissue contains a small but present level of water signal while the glandular tissue does have some fat signal.

Volunteer #	Average water signal percentage in fatty tissue	Highest water signal percentage in glandular tissue	Lowest water signal percentage in glandular tissue
5	8.4%	76.7%	33.2%
6	8.8%	-	-
7	6.9%	83.9%	36.7%
8	9.6%	77.1%	39.9%
9	7.9%	-	-
10	6.5%	-	-

#### 2.3.4. Local Imaging Coils

A picture of the prototype coils with copper tape can be found in Figure 2.9. A picture of the etched coils can be found in Figure 2.10. A picture with the etched coils on the breast applicator is shown in Figure 2.11.



**Figure 2.9:** Pictures of both prototype local imaging coils

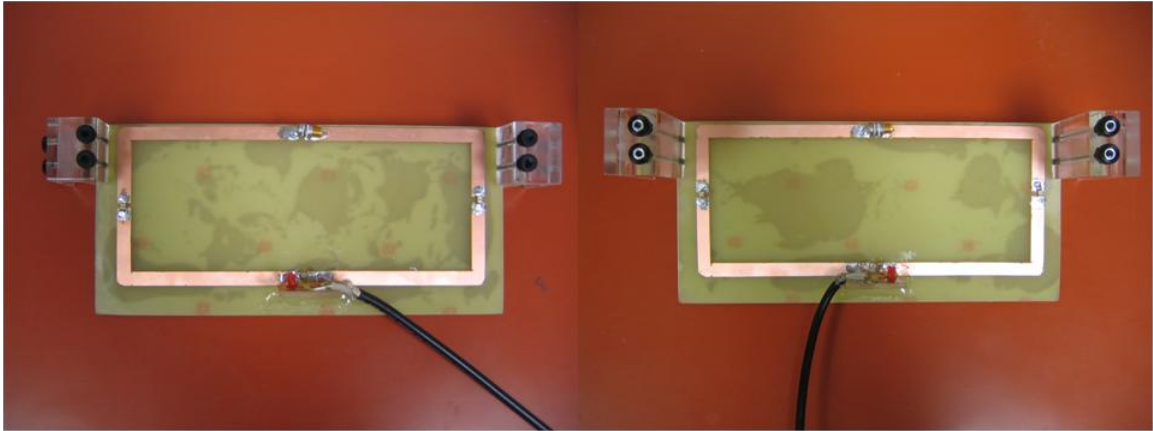


**Figure 2.10:** Pictures of both etched local imaging coils. Notice the plastic coil holders on the sides of each coil.

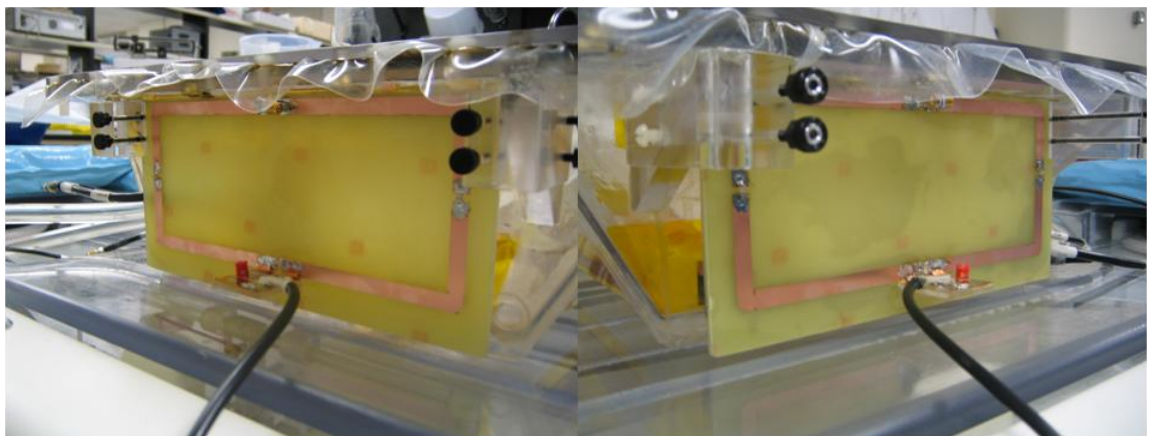


**Figure 2.11:** Pictures of the etched local imaging coils on the breast applicator. Notice how the coil holders screw into the sides of the applicator, holding the coils close to the applicator.

Results from the SNR measurements can be seen in Figure 2.12 for single echo sequence and in Figure 2.13 for the 15.4 ms echo of the multi-gradient echo sequence.

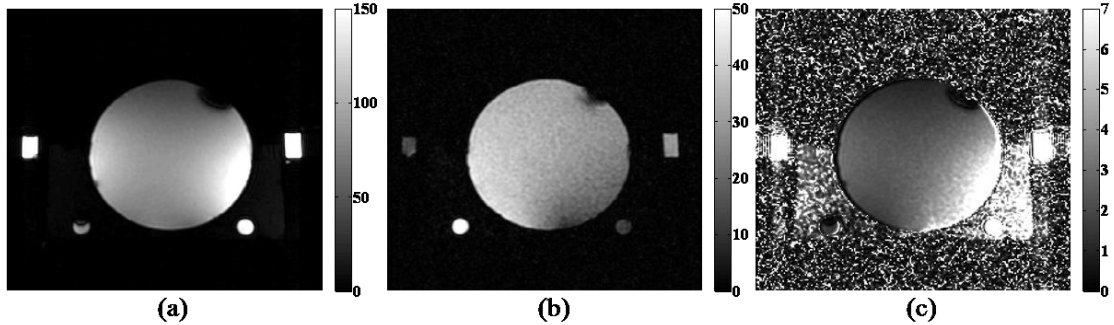


**Figure 2.12:** For the single echo sequence (a) SNR of the local coils (b) SNR of the body coil (c) Ratio of SNR of the local coils to SNR of the body coil. Notice the difference in the color bars, with the local coils having much larger SNR than the body coils. The decreased SNR is apparent in (b), where the increased noise is seen in the phantom compared to (a). Lastly, the SNR of the body coil should be very uniform but has some spatial variation in (b). These variations are most likely due to interactions with the RF antenna of the applicator.

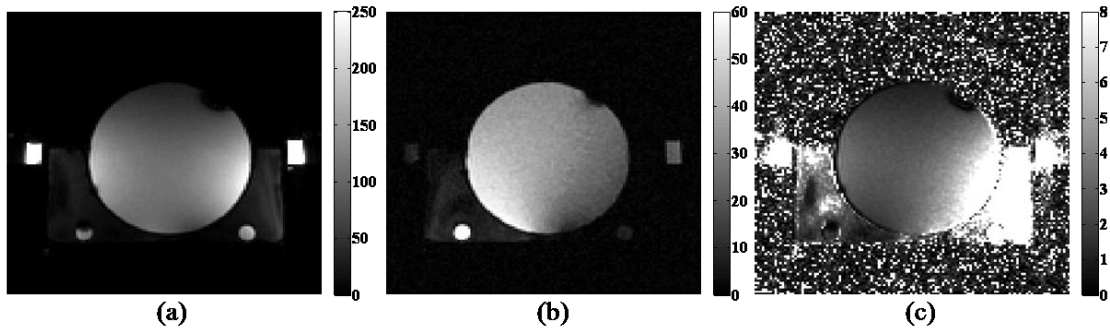


**Figure 2.13:** For the 15.4ms echo of the multi-gradient echo sequence (a) SNR of the local coils (b) SNR of the body coil (c) Ratio of SNR of the local coils to SNR of the body coil. Notice the difference in the color bars, with the local coils having much larger SNR than the body coils. The decreased SNR is apparent in (b), where the increased noise is seen in the phantom compared to (a). Lastly, the SNR of the body coil should be very uniform but has some spatial variation in (b). These variations are most likely due to interactions with the RF antenna of the applicator.

## 2.4 Discussion

As seen from the results, we have created an improved patient support and imaging system for MR thermometry of the hyperthermia treatment of LABC.

First, the improvements to the breast applicator have allowed for its use with the MR system. The leak proofing of the box has made it feasible to fill it with  $D_2O$ , which

must be kept sealed from air to prevent it from absorbing water from the atmosphere. The removal of the valves and the ferrous particles near the bottom antenna made for artifact-free images. The inclusion of oil references allowed for us to have frequency references for use with the technique discussed later in this thesis.

Secondly, the newly made patient support allows for increased comfort inside the MR scanner bore while also providing an increased feeling of support. The results in Table 2.2 show that on average, the volunteers found the system comfortable and that little pain was felt. None of the 10 volunteers in the comfort study reported any significant pain in their chest or other areas. The most complaints were discomfort in the back, shoulders, and opposite breast. The opposite breast was hard to address since the applicator will block any hole created for that breast to drop into. The chest pain discomfort was a focus of the new system and was addressed as much as possible, based on discomfort observed with the prior comfort systems. However, a compromise was needed between chest comfort and positioning of the breast into the applicator. If maximum chest comfort was obtained, then the breast would not protrude very far into the applicator, reducing the effectiveness of the heating antennas. Thus, the system as designed allows for a good compromise between the two, with good coverage and minimal discomfort.

The images obtained during the comfort study were useful for improvement of the patient support and for characterization of the water/fat content of breast tissue. In the initial 4 volunteers, the main focus of the study was to determine how well the breast was positioned inside the applicator and how the breast was affected by the water bolus. Attempts were made to acquire enough fat-water images to assess the fat/water ratio of

the tissue, but were not successfully acquired due to technical problems and time constraints.

However, for volunteers 5-10 the focus switched from anatomical imaging to fat-water imaging, which was possible due to improved time efficiency of the study and less evaluation of changes to the comfort system. The fat-water results show that there is approximately 8% water signal in the fatty tissue and high water/fat ratio in the glandular tissue. These results confirm previous studies[3, 7]. The water/fat measurements may have some limitations due to the fact all of the fat-water images were acquired during free breathing. Each image at a different TE was acquired over 20 seconds, which is time for approximately 4-6 breaths, the effects of which would be all averaged into one image. As discussed in the introduction, free breathing will produce significant phase artifacts due breathing motion of the lungs. The phase changes could affect the phase differences between different TE images, thus affecting the calculated fat and water images. However, since there were no visible artifacts in the fat and water images and the fat/water ratios were in agreement with other values, they appear to be useful for breast fat-water estimates for MR pulse sequence parameter selection. Other errors in the fat-water imaging could be due to the multiple peaks of fat and J-coupling. Both could cause some fat signal to be fit as water signal. However, this error is often less than 10% of the fat signal, which would only affect our fat/water ratio results by approximately a few percent.

Lastly, the local imaging coils show improved SNR over the body coil. From the images in Figures 2.12 and 2.13 show that the local coil to body coil SNR ratio is at least 2 in all areas of the phantom (with the lowest values in the top of the phantom). In the

center, the ratio is approximately 3 while near the edges of the phantom the ratio is approximately 8. Thus, these coils provide a large improvement. While the coils do display a spatial variation of the signal that is common to local MR coils, these variations can be addressed with normalization methods [139-141]. Many commercial scanners now include a form of normalization software that can be applied to most pulse sequences.

## **2.5 Conclusion**

In this chapter, a new system for the hyperthermia treatment of locally advanced breast cancer was described. The system provided improved comfort over previous systems and included oil references for correction of field drift (discussed further in Chapter 3). Local MR imaging coils have been developed that provide improved SNR over the body coil and fit directly onto the breast applicator. These coils provide at least twice the SNR and up to 8 times the SNR of the body coil. This system will provide the ability to treat LABC patients inside the MR scanner and allow for the use of the MR thermometry techniques discussed later in this thesis (Chapter 4 and 5).

## 3 Field Drift Correction with Oil References in the Extremity and Breast

### 3.1 Introduction

As discussed in the introduction of this thesis, the thermometry errors caused by field drift during a hyperthermia treatment can be very large. In this chapter, we described the performance of oil filled references for field drift correction inside of hyperthermia applicators containing phantoms and in vivo tissue. A major advantage of oil references is that their MR resonant frequency change with temperature is nearly zero[110] in comparison to that of water. Thus any change in their MR resonant frequency will be due only to magnetic field drift and not due to temperature dependence. Key to the method is that the drift measured at the position of the references (which are positioned outside of the treatment region that is occupied by the patient or phantom) must be extrapolated using spatial fitting methods to estimate the drift in the treatment region. Since the temperature sensitivity of water is known precisely, the experiments can be performed without heating in order to focus the investigation on the adequacy of the oil references for field drift correction. In addition, to guide future use of oil references for B<sub>0</sub> drift correction, the use of four, eight, and twelve oil references was investigated to determine the effect of more oil references on the magnitude of the correction error. Lastly, different field fitting methods are compared to determine if there is a difference in their correction of the field drift, as averaged over the entire image. The work presented in this chapter was published in the International Journal of Hyperthermia[142].



## 3.2 Theoretical Development

### 3.2.1. Field Fitting Methods

Three methods were used to fit the phase differences in the oil references to a function that could be used to estimate phase or frequency drift at any point in the image field-of-view, (a map of the phase changes due to field drift). The first method used was linear least-squares fitting. The three variable linear fit accounts for a constant background term and linear x and y terms, the equation for which is

$$\Delta B_0(x, y) = a_0 + a_1x + a_2y \quad (3.1)$$

where  $\Delta B_0$  is the frequency offset from the main magnetic field (Hz) and x,y are points along the two axes of the image. The second method is a second-order least-squares fit to six variables which was adopted from the field fitting equation of El-Sharkawy [107]:

$$\Delta B_0(x, y) = a_0 + a_1x + a_2y + a_3x^2 + a_4y^2 + a_5xy \quad (3.2)$$

The third method used was that of minimum curvature surface fitting. This method fits a minimum curvature spline surface to the data using a basis function described by Franke [143] and a fitting method derived from the IDL function `min_curve_surf` (ITT Visual Information Solutions, Boulder, CO). For n data points (references in this case), n+3 equations are solved simultaneously using back substitution, solving for the following coefficients and equation

$$\Delta B_0(x, y) = a_0 + a_1x + a_2y + \sum c_i C(x_i, x, y_i, y) \quad (3.3)$$

with

$$C(x_0, x_1, y_0, y_1) = d^2 \log(d) \quad (3.4)$$

where d is the distance between  $(x_0, y_0)$  and  $(x_1, y_1)$ .

### **3.3 Materials and Methods**

#### **3.3.1. Phantom Creation**

Two phantoms were made for this experiment, both made using the recipe by Wyatt, et al.[142] and based on the recipe by Madsen [144]. The homogenous phantom was composed of only water and gelatin, lacking the oil of the Madsen phantoms so that no error in the PRFS technique would occur. The phantom was contained in a 4.25” diameter and 14” long plastic cylinder with one #19 gauge catheter (to accommodate the fiberoptic temperature probe) through the center. An inhomogenous phantom was made to simulate a human leg more closely, to determine if there were any effects on drift correction due to the inhomogeneity of the leg. A 0.25” layer of vegetable shortening was evenly distributed around the edges of a 4.25” diameter and 11” long polycarbonate cylinder. A sterilized beef bone (Dentley’s Natural Item #03277 from Pacific Coast Distributing Inc., Phoenix, AZ, USA) was then filled with an oil-in-water gelatin material (Madsen recipe) that contained equal amounts of fat and water. The bone was placed inside of the cylinder near the top of the phantom (to mimic the leg), which was then filled with the same water gelatin material used for the homogenous phantom. A diagram showing the construction and materials of each phantom can be found in Figure 3.1. Lastly, both phantoms lacked the propylene glycol called for by Madsen, which is intended to increase the stability of the emulsion. However, the phantoms were stable over a period of months, as long as the phantoms remained sealed.

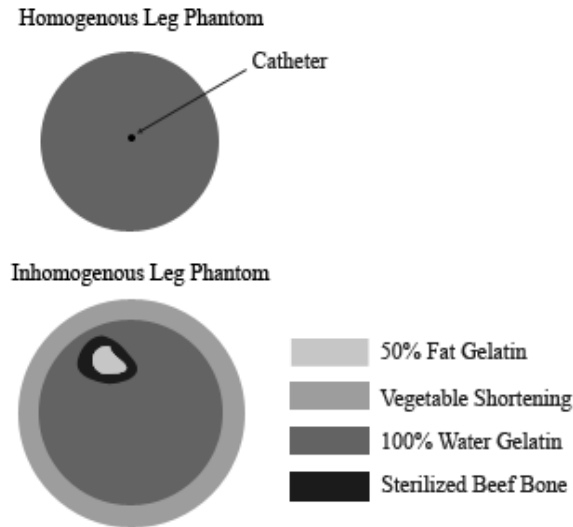


**Figure 3.1:** Construction and materials of the phantoms used in the experiments. The 50% fat gelatin and sterilized beef bone were placed in the inhomogenous leg phantom to mimic the bone marrow and bone of a human leg, respectively.

### 3.3.2. Field Drift Characterization

To determine the general nature of the magnetic field drift over a long period of time, a 52 hour field drift experiment was performed. A large water-only gelatin phantom was allowed to equilibrate overnight in the magnet, at which point it was scanned with a frequency drift mapping method approximately every 2 minutes for 52 hours.

The field drift mapping method used for this paper is an extension of that used by El-Sharkawy and is designed to provide optimal field resolution without phase-wrap artifacts in water. For every experiment, a one centimeter thick slice was imaged on a 1.5T GE Signa HDX (General Electric, Milwaukee, WI, USA) with a 2D axial SPGR (spoiled-gradient echo) sequence with repetition time=38.5ms, Flip angle=30°, bandwidth=15.6 kHz, FOV = 30 cm, image matrix=128x128, and four signal averages.

This slice was imaged at three different echo time (TE) values, 11, 12.5, and 20 ms (“triplet sequence”). The phase difference between the 11 and 20 ms images (divided by the echo time difference) produces a frequency offset image with a range of  $\pm 55.5$  Hz. The 11ms to 20ms TE difference allows for adequate frequency resolution but also the range to accommodate for B0 field drift without phase wrap. The time for each scan was 20 sec, with the entire triplet sequence lasting approximately 1 minute.

### **3.3.3. MAPA Phantom Experiment**

Another study was performed to evaluate drift correction in the same applicator used for heating human extremity tumors: a mini-annular phased array (MAPA) that consisted of 4 twin dipole antennas [145, 146]. A photograph of the MAPA applicator can be seen in Figure 3.2. This applicator uses a water bolus for dielectric match between the applicator antennae and the phantom (or leg). The MAPA had eight permanently attached references filled with silicone oil (Thomas Scientific #6428R25, Swedesboro, NJ, USA) with four located inside the bolus (2” diameter, 3.5” from center) and four directly outside the bolus (2”x0.5”, 5” from center). There were also eight temporary references (1.125” and 0.625” diameter, 5” from center) that were taped to the outside of the MAPA to assess the effectiveness of various reference configurations. The typical location of the oil references for each trial is shown in Figure 3.2.

Five trials were performed, but only four were used due to insignificant drift ( $< 2$  Hz) during the discarded one. At the beginning of each trial, a gelatin-water phantom that had equilibrated with the MR room overnight was placed into the MAPA. The bolus was then filled with 99.8% pure D<sub>2</sub>O (Sigma Aldrich #617385, St. Louis, MO, USA).

While water is conventionally used for a bolus, it can create MR image artifacts due to convection and flow. Thus we used D<sub>2</sub>O, which does not create an MR image signal but otherwise functions as well as water in creating a dielectric match between the RF antennas and the object of interest. Care was taken to avoid contamination of the D<sub>2</sub>O with H<sub>2</sub>O by keeping the system sealed. The D<sub>2</sub>O was allowed to equilibrate with the control room temperature, which in general differed from the scanner room by approximately 1-2°C. By the time the water reached the bolus and the scanning begun, the difference in temperature between the bolus water and the phantom temperature was assumed to be less than 1°C. The phantoms were not heated for this test. Temperature was monitored in trial #4 using fiber optic thermal probes (Lumasense Technologies, Santa Clara, CA, USA) inserted into a catheter running through the middle of the phantom.

An image of a central slice of the phantom was acquired using the frequency drift triplet scanning sequence approximately every 2 minutes for total trial times ranging from 70 to 127 minutes. Since the purpose of this work was to evaluate drift correction, the region was not heated so that observed and reference predicted drift could be compared. Scans were performed for this duration to span the length of a typical hyperthermia treatment, where temperature monitoring normally continues for 60-80 minutes [78]. The homogenous phantom was used in trials #1, 2, and 4, while the inhomogenous phantom was used in trial #3. For phantom trials #1-3, two of the eight outside references were unusable for the data analysis after the trials were performed, due to an error in filling that was noticed only after the trials were performed. Thus, only 6 usable outside references were present. Phantom trial #4 did not have any outside oil references.

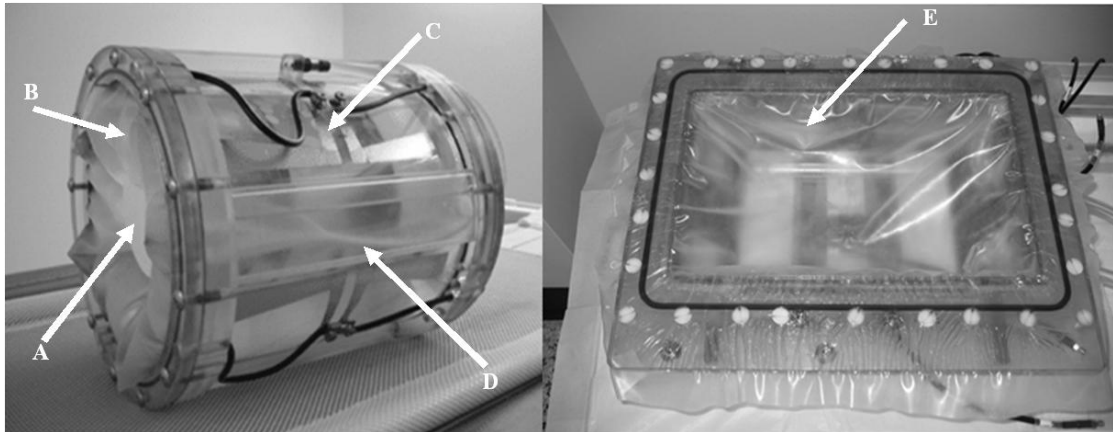


**Figure 3.2:** Pictures of the MAPA and breast applicators (*Left*) MAPA applicator (*Right*) Breast Applicator. A: cylindrical phantom in contact with bolus, B: membrane confining the bolus, C: heating antennae (one of 4) configuration and connections, D: one of 4 oil-filled “rect” reference sections, E: membrane in breast applicator separating breast from bolus (below membrane).

### 3.3.4 MAPA Leg Experiment

The same MAPA applicator used for the phantoms was used for a human leg experiment. For 15-20 minutes before each trial, the D<sub>2</sub>O bolus was preheated to 31-34°C, depending on the temperature of the scanner room and the temperature of the subject. The purpose of preheating the D<sub>2</sub>O was to keep the surface temperature of the leg as constant as possible during a trial. However, no RF heating was applied during any of the leg trials. All leg trials were performed with the same healthy human volunteer (Male, Age 24) using informed consent under an institutional review board (IRB) approved protocol.

Five trials were performed, but only four were used due to insignificant drift (<2 Hz) during the discarded one. For each trial, the right leg of the subject was placed into the center of the MAPA so that the knee was at the edge of the applicator. Once the leg

was situated and restrained with foam, fiber optic temperature probes were taped to the surface of the leg near the center of the applicator. The bolus was then filled with the preheated D<sub>2</sub>O and the subject placed in the magnet. A 1cm thick slice was imaged near the center of the applicator with the frequency imaging triplet sequence. The slice was acquired approximately every 2 minutes for total trial times ranging from 42 to 80 minutes. For leg trial #1, again, two of the eight outside oil references were found to have an error in filling (as mentioned previously), so only 6 usable outside reference were present. Leg trial #4 did not have any outside oil references.

### **3.3.5 Breast Applicator Phantom Experiments**

Drift correction was also investigated for a rectangular applicator for breast hyperthermia, containing five twin dipole antennas [42]. A photograph of the applicator is shown in Figure 3.2. Eight mineral oil references were placed on the inside and outside of the applicator, with their locations shown in Figure 3.3. Two trials were performed similar to the MAPA experiment, where a spherical water-based gelatin phantom was placed in the applicator, which was then filled with D<sub>2</sub>O so that the bottom portion of the phantom was surrounded by the bolus. One center slice was imaged with the same SPGR triplet sequence as the MAPA experiment. The slice was acquired approximately every 2 minutes for approximately 90 minutes for both trials. Fiber optic probe temperature data was acquired using three catheters placed near the center region of the phantom.

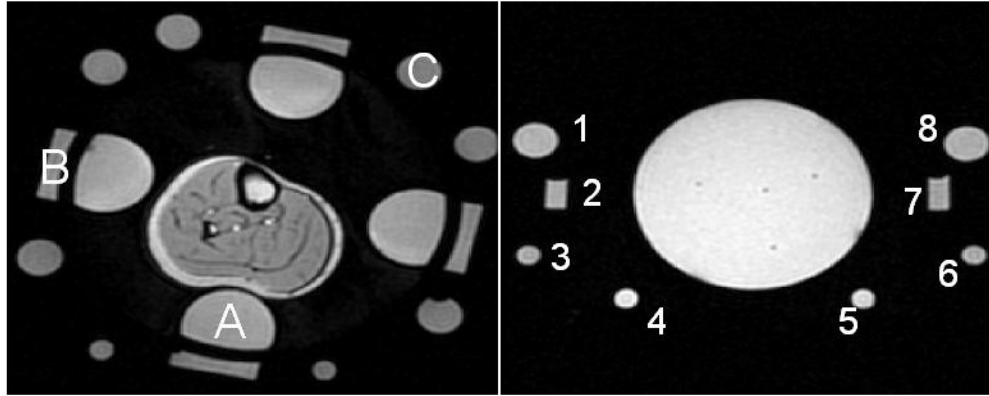


**Figure 3.3:** Images of the experimental setup (*Left*) Axial magnitude image of experimental setup and oil references for the MAPA experiments. (A) one of 4 “inner” references inside the D<sub>2</sub>O bolus, (B) One of 4 “rect” references outside water bolus, (C) one of 8 “outer” oil references outside water bolus. (*Right*) Axial magnitude image of experimental setup and 8 oil references for the breast applicator experiments. Notice that the breast applicator references are not symmetrically placed, unlike the MAPA. It is lacking reference in the top of the image since that would be where the patient would be in a treatment

### 3.3.6 Data Analysis

For all MAPA and breast applicator experiments, the field offset ( $\Delta B_0$ ) at each pixel was calculated for each time point in the series using the phase difference between the 11 and 20 ms images and the equations described by El-Sharkawy. These field values were then averaged across the entire object of interest (avoiding the bone and major blood vessels in the leg data) to obtain an average field value in the object at that time point. For each trial, the average drift rate was then found by taking the final total drift value and dividing it by the total time of the trial.

To calculate and correct the phase changes throughout the image, the pixel by pixel phase differences between consecutive TE=20 ms images were calculated. The mean of 5x5 pixel regions of interest (ROIs) in the center of each oil reference were then calculated for each phase difference. Phase difference prediction images were then



generated with these values using the three methods (linear and nonlinear least-squares as well as minimum curvature surface fits). All phase difference images and the phase difference prediction images were then converted to temperature units (in order to express the results in a scale that could be interpreted in terms of the expected temperature changes during hyperthermia of between 38°C and 43°C) using the standard PRFS formula (below) assuming that all phase changes are due to temperature change. The equation used to calculate temperature change from PRFS was as follows [89]:

$$\Delta T = \frac{\Delta \phi}{(f * TE * \alpha * 360)} \quad (3.5)$$

where  $\Delta T(^{\circ}\text{C})$  and  $\Delta \phi(^{\circ})$  are the temperature and phase changes respectively,  $f$  is the imaging frequency (Hz),  $TE$  is the echo time (ms), and alpha is the temperature coefficient (approximately equal to  $-0.01 \text{ ppm}^{\circ}\text{C}$  in muscle [147]). The absolute difference between the measured temperature difference image and the predicted temperature difference image was averaged across the entire phantom or leg for each time point. The absolute difference was used since both underestimation and overestimation of temperature are considered to be detrimental to proper thermal dosimetry of clinical hyperthermia. All calculations were done with Matlab (The Mathworks, Inc., Natick, MA, USA).

Three reference combinations were used to analyze the data. Referring to Figure 3.3, the four references closest to the leg (labeled as A) are called the “inner” references, the references behind (radially outside) the inner references (B in Figure 3.3) are the rectangular or “rect” references, and the eight circular references (C in Figure 3.3) as the

“outer” references. The combination of the inner and rectangular references is referred to as “inner-rect” while the inner and outer reference combination is “inner-outer”.

To gauge the effect of oil reference distance from the center of the applicator on correction performance, four of the rectangular references and four of the outside references were each used for correction without the inner references for the MAPA phantom and leg experiments. Also, four 5x5 pixel ROIs (spaced evenly around the leg) in the fat layer of each leg trial were chosen and used for correction to compare the fat correction method to the oil reference method.

The temperature error at the end of each trial was averaged across the entire leg or phantom to provide the total temperature error for each trial. The total temperature error for each combination of oil references was then averaged over all valid trials. For the leg experiment, the same procedure was followed except with the exclusion of leg trial #1, which was found to have large temperature changes over the hour long trial that appeared to be due to the real changes in temp or patient movement.

## **3.4 Results**

### **3.4.1 Field Drift Temporal Behavior**

The results of the long term frequency drift can be seen in Figure 3.4, which shows the principally cyclical (diurnal) behavior of the magnet drift. The peaks of the drift in Figure 3.4 coincide with periods of intense sunlight at a nearby observation center (Duke Forest). The MRI suite has a large skylight for light to shine through, suggesting

that temperature changes due to sunlight may be resulting in a large amount of the system drift.

The field drift plots for both the phantom and leg experiments (over the much shorter interval of 1 to 2 hours) can be found in Figure 3.5. Since 0.01ppm at 1.5T is 0.6357Hz, it is apparent that the drift is the equivalent of large temperature changes.

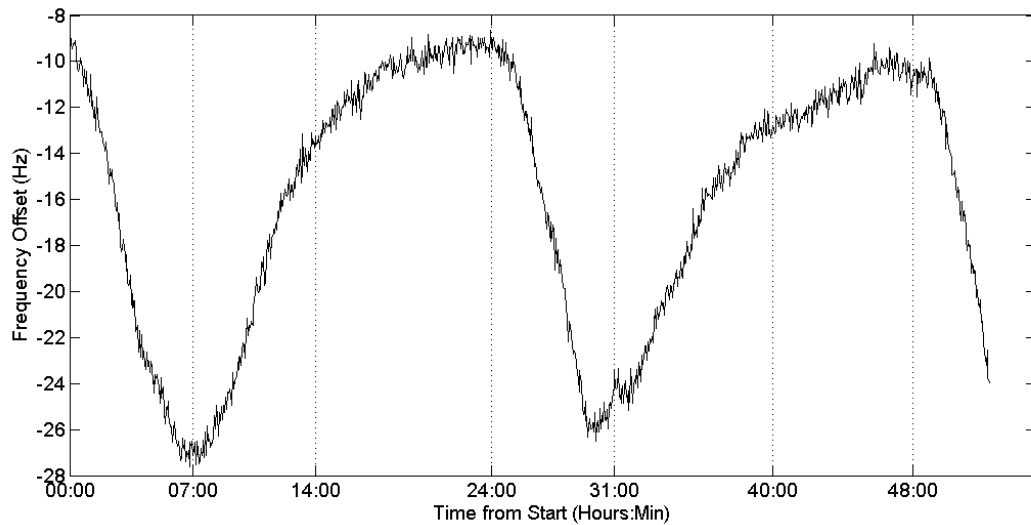


**Figure 3.4:** Long-term frequency drift of the 1.5T magnet, demonstrating the principally diurnal change as well as variable components that lead to poor predictability of the behavior.

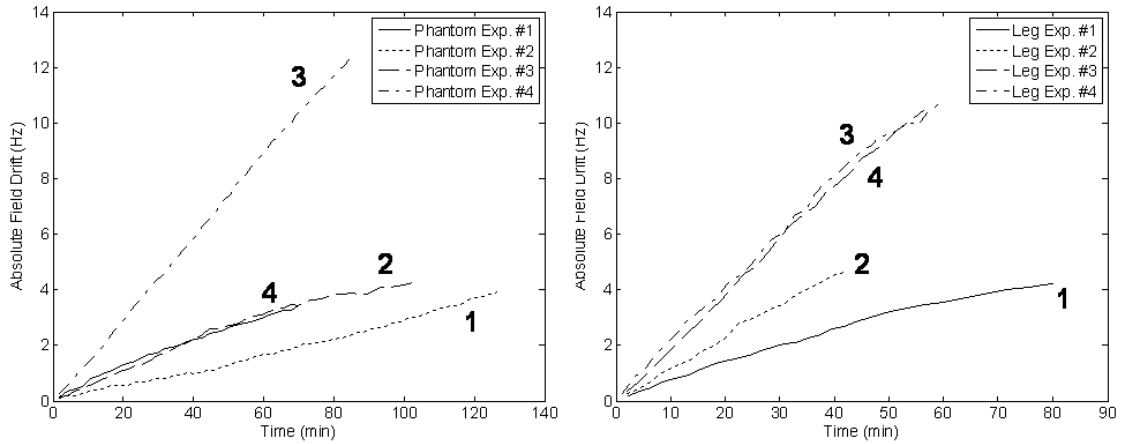


**Figure 3.5:** (*Left*) Frequency drift over time for all trials of the MAPA phantom experiment. (*Right*) Frequency drift over time for all trials of the MAPA leg experiment. These diagrams illustrate the variability and magnitude of the amount of drift that can be encountered during PRFS thermometry measurements. The temperature error for these experiments (in °C) would be even larger than the field values.

### 3.4.2 MAPA Phantom Results

An image of the temperature error at the end of trial #1 of the phantom experiment is shown in Figure 3.6. Correction with the inner and outer reference combination was applied to produce the image. A plot of the absolute average temperature error as a function of time for trail #1 is also shown in Figure 3.6. The temperature error before correction, the error after correction using inner only, inner-rect, and inner-outer configurations, and the best percent correction seen among those configurations can be seen for all four trials in Table 3.1. The outer references were not used in trial #4 due to the lack of valid outer references. All MAPA phantom results use the least-squares method of fitting since results using MCS were not significantly different. Lastly, the fiber optic probe observed approximately 0.3°C of temperature

change in trial #4, which is approximately the same increase seen in the error of the correction.

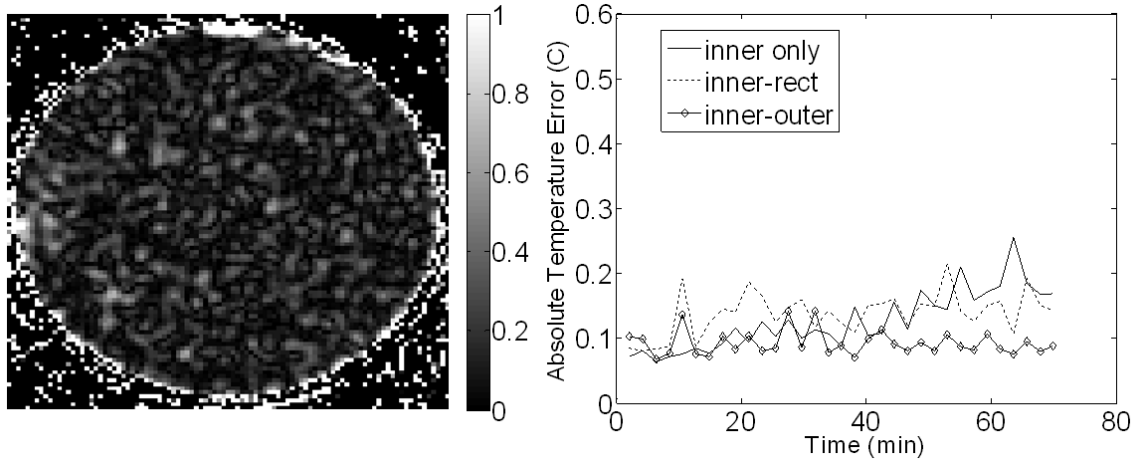


**Figure 3.6:** Results from the MAPA phantom experiment. (Left) Image of the final temperature error (in °C) after correction using the inner-outer reference combination. (Right) Plots of the absolute temperature error for each correction scheme over time. The definition of each reference combination can be found in the methods and Figure 3.3. All reference combinations provide good correction, with the inner-outer combination performing slightly better than the others. As seen in the left image, the correction is very spatially uniform.

### 3.4.3 MAPA In-Vivo Leg Results

An image after applying correction with the inner and outer reference combination for trial #3 of the MAPA leg experiment is shown in Figure 3.7. A plot of the absolute average temperature error as a function of time for trail #3 is also shown in Figure 3.7. The temperature error before correction, the error after correction using inner only, inner-rect, and inner-outer configurations, and the best percent correction seen among those configurations can be seen for all four trials in Table 3.1. All MAPA leg results use the least-squares method of fitting since results using MCS were not significantly different.

The averages of the final temperature error after correction for all trials of the phantom and leg MAPA experiments are shown in Table 3.2 for several reference configurations. Table 3.2 also includes an averaging of the MAPA leg trials that excludes trial #1, since there was significant temperature change inside the leg that skewed results. This was determined by the fiber optic temperature probe on the leg surface, which reported constant decrease in temperature, resulting in an overall temperature change of 0.95 °C. The temperature for the other leg trials was much more constant over the course of each trial.

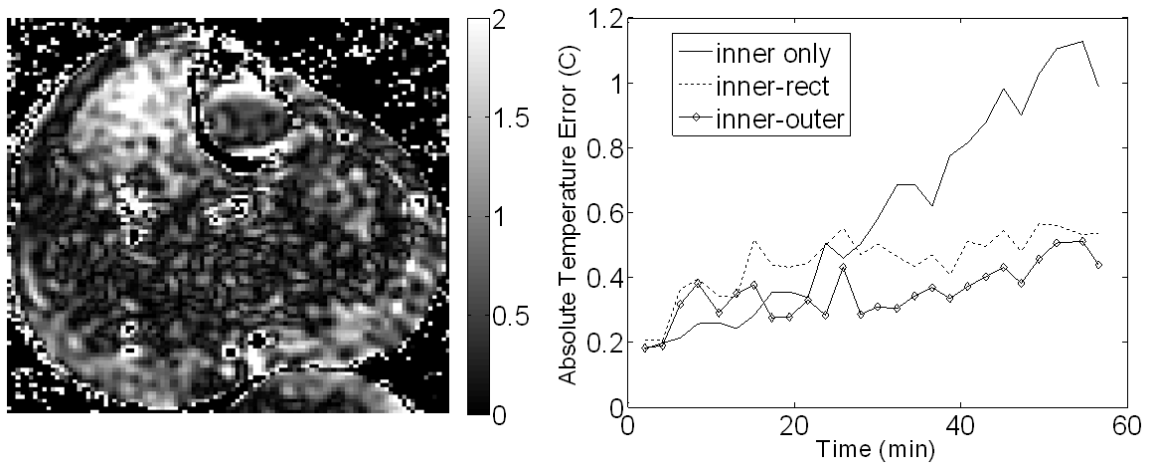


**Figure 3.7:** Results from the leg experiment. (Left) Image of the final temperature error (in °C) after correction using the inner-outer reference combination. (Right) Plots of the absolute temperature error for each correction scheme over time. The definition of each reference combination can be found in the methods and Figure 3.3. All reference combinations provide good correction, with the inner-outer combination performing slightly better than the others. As seen in the left image, the correction is spatially uniform except for the upper left portion of the leg. This inhomogeneity is most likely due to the effect of internal leg perfusion or muscle movement.

### 3.4.4 Breast Applicator Results

An image after applying correction with for trial #1 of the breast applicator phantom experiment is shown in Figure 3.8. A plot of the absolute average temperature

error as a function of time for trail #1 is also shown in Figure 3.8. The temperature error before correction, the error after correction using different reference configurations and the best percent correction seen among those configurations can be seen for both trials in Table 3.1. All breast applicator experiment results use the MCS method of fitting since the noise in the least-squares fitting results was much worse. Fiber optic temperature data showed no temperature change throughout both trials.

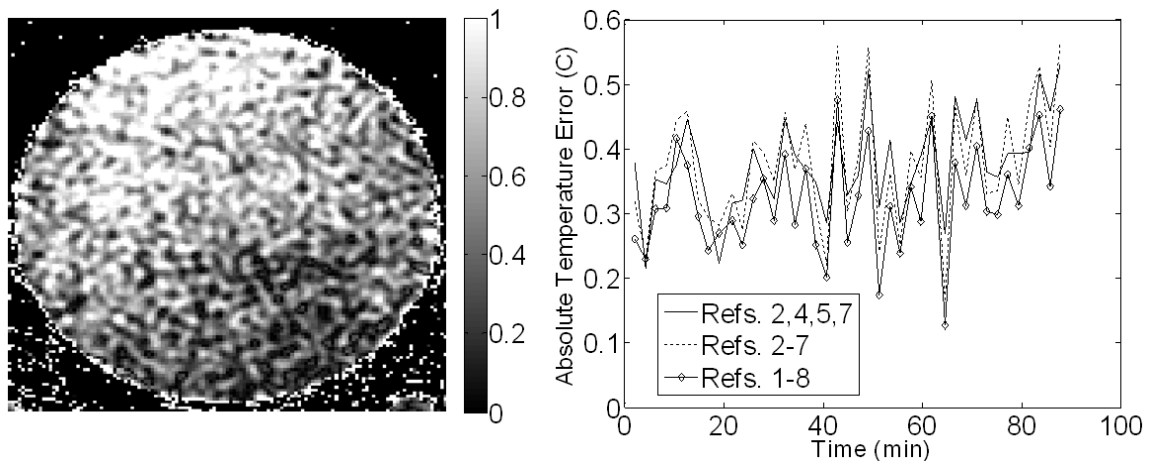


**Figure 3.8:** Results from the breast applicator phantom experiment. (Left) Image of the final temperature error (in  $^{\circ}\text{C}$ ) after correction using the inner-outer reference combination. (Right) Plots of the average absolute temperature error for each correction scheme over time. The location corresponding to the number of each reference is shown in Figure 3.3. All reference combinations provide good correction. As seen in the left image, the correction has worse correction at the top than the bottom, which is thought to be due to the lack of oil references near the top of the phantom.

**Table 3.1:** Final uncorrected temperature error (°C), final temperature error after correction (°C), and the best percent correction for every trial of each experiment of this study. The final temperature error after correction is shown for several reference combinations. Also, the best correction percentage seen out of all the reference combinations is shown, with the correction percentage being the percentage of the field error that was corrected.

MAPA Phantom	Uncorrected Temperature Error (°C)	Temperature Error After Correction (°C)			*Best Correction %
		Inner only	Inner-Rect	Inner-Outer	
Trial #1	5.37	0.17	0.14	0.09	98.3
Trial #2	6.15	0.18	0.11	0.10	98.3
Trial #3	6.68	0.11	0.16	0.18	98.3
Trial #4	19.48	0.66	0.38	N/A	98.1
<b>MAPA Leg</b>					
Trial #1	6.52	2.52	2.43	2.25	65.5
Trial #2	7.26	0.43	0.64	0.45	94.0
Trial #3	16.42	0.99	0.54	0.44	97.3
Trial #4	17.11	1.39	0.39	N/A	97.7
<b>Breast Phantom</b>		<b>References 2,4,5,7</b>	<b>References 2-7</b>	<b>References 1-8</b>	
Trial #1	9.46	0.53	0.57	0.46	95.1
Trial #2	11.17	0.29	0.20	0.16	98.6

\* The best correction % results use the best correction of the reference combinations shown for each trial.



**Table 3.2:** Average temperature error across all trials of the MAPA leg and phantom experiments for several reference combinations. Notice that with increased number of references, the average temperature error decreases in general. However, this tends to be a diminishing effect as you increase the number above eight. Lastly, using the in-vivo fat layer (with 4 reference locations) performs slightly worse than 4 oil references, as expected due to the presence of water in in-vivo fat.

Average Temperature Error (°C)			
Reference Configuration	All Leg Trials	*Leg Trials 2, 3, and 4	All Phantom Trials
Inner only	1.33	0.94	0.28
Rect only	1.75	1.53	0.51
Outer only	1.82	1.37	0.37
Inner-Rect	1.00	0.52	0.20
Inner-Outer	1.05	0.44	0.13
Inner and 10 or more Outer	1.09	0.51	0.19
In-Vivo Fat Layer only	1.41	1.10	N/A

\* Results excluding leg trial #1 are shown for comparison since large temperature errors were seen in that single trial that are most likely due to confounding temperature changes in the leg.

### 3.5 Discussion

In this work we have examined the performance of oil references located inside and outside of a hyperthermia applicator to correct for field drift of MR magnets over 1-2 hour periods. The long term frequency drift shown in Figure 3.4 indicates that real time frequency drift correction is needed for accurate characterization of temperature change over these time periods (error less than 1°C). The nonlinearity of the drift suggests that pre-calibration and extrapolation of the drift during the treatment will not work for all drift conditions. The diurnal character of the drift suggests it is likely due to environmental temperature changes in the MR system room which may have additional non-periodic variations throughout the year. While the total uncorrected drift over time for all trials was mostly linear, there were trials performed where the drift would plateau

at the beginning or end of a trial, resulting in insignificant drift. The sinusoidal nature of the plot in Figure 3.4 helps explain why these plateaus occurred.

The average temperature error due to uncorrected field drift in both phantoms and legs was determined along with the spatial distribution of the error. These results show that oil reference correction works very well with phantoms; with corrected images showing small average temperature error and good spatial correction. Our MAPA phantom experiment showed an average error in the range of 0.18-0.28°C and excellent spatial correction. Trial #4 had a large temperature error, but as a percentage of total drift the error was similar to others. For the first three phantom trials, the four inner references alone worked just as well as the eight-reference inner-rect or the inner-outer combinations. In trial #4, the inner-rect combination corrected noticeably better than the inner references alone, by almost a factor of two. Therefore, oil reference correction is very effective in phantoms, eliminating approximately 98% of the error due to drift, as seen in Table 3.1.

Unlike De Poorter, we have shown useful correction in the leg, with an average error of 1.33 °C and good spatial correction. Trial #1, however, did show large correction errors that are similar in magnitude to the errors seen in the one leg experiment performed by De Poorter, on the order of 2.5° C. The large error could be due in part to several uncontrollable factors, such as physiologic changes (perfusion, etc.), external heating from the bolus, or phase changes from subject movement. Internal perfusion changes are most likely, considering the substantial difference in drift between the muscle and fat tissues, suggesting an actual temperature change inside the leg. This coupled with the fact that trial #1 was the only trial in which the surface temperature of

the leg changed significantly (by approximately 1°C) suggests that real temperature changes were occurring inside the leg. Thus, if we exclude trial #1, the other three leg trials showed improved correction with four references, with an average error of 0.94°C. As seen from the best % correction results of Table 3.1, approximately 95% of the error created by field drift was corrected in leg trials #2-4, which is very similar to the % correction seen in the MAPA phantom experiment.

While the results of the MAPA leg experiment using only four references were very encouraging, the correction errors of the eight reference inner-rect or inner-outer combinations showed further improvement to 0.52 °C and 0.44 °C, respectively. These values are almost half the error seen using four references. On the other hand, the effect was not seen in all trials, with leg trial #2 showing almost no difference between the four and eight reference combinations. It was also not seen in most of the phantom and breast applicator trials. However, even when the improved correction was not seen, the correction with eight references was no worse than the correction with four references. Much of this variance could be due to the fact that the drift was markedly different across all trials and that some drift situations favored the extended reference placement of one combination over others. Thus, it can be concluded that eight references will likely perform as well or better than four references, depending on the drift behavior.

While eight references can improve correction, it can be seen from Table 3.2 that there was little improvement to the correction when using 10 or 12 oil references instead of eight. However, this could be due to the spatial location of the references or there could be a greater difference when a much higher number is applied. Thus, an improved

approach could be to have a very large number of spatially distributed ROIs by positioning an annulus of oil around the MAPA.

The effect of distance of the references from the object of interest was investigated by using only the outer or rect references. As seen in Table 3.2, the results show that on, average, the outer and rectangular references perform worse than the inner references, suggesting that distance to the object of interest is important.

Other researchers have suggested using the fat-tissue signal (skin on the leg) as a “reference” material even though this does contain tissue water and blood vessels[103, 108, 109]. To compare such methods with our oil references, four ROIs in the fat layer of each leg trial were used for correction to compare to the oil reference correction. From Table 3.2, it can be seen that there was a slight increase in the error using the fat correction compared to using only the inner references (inner-only) for correction. However, this was most likely due to increased noise in the fat tissue and is not an important difference. Also, it should be noted that if the leg tissue were being heated, fat may not be a good reference since it often contains small percentages of water (<10%). The phase of the water component of the fat will change with temperature as the leg is heated, adding to the phase of the pure fat signal. While small, this extra phase will add error when measuring the phase change of the fat due to field change. However, Gellermann et al. have shown that the technique can help during heating in soft tissue sarcoma of the pelvis[104].

In the MAPA leg experiment, the use of heated water ranging from 31-34°C could have significantly varied the temperature of the “inner” oil references as well as possibly heating the “rect” and “outer” references. Since all the references started at

room temperature, error could have resulted if water references were used, for reasons discussed in the introduction. However, since oil references were used, these errors could not occur since the oil is not temperature sensitive, which would explain the small temperature error measured in the experiment.

The MAPA phantom and leg experiments show results from using oil references that are symmetrically placed all around the object of interest. The breast applicator experiment had references that surrounded only about 60% of the phantom, with the top of the phantom having no references in the vicinity since that is where the subject's torso would be. From the results seen in Figure 3.8, there was a noticeable effect of having less oil reference coverage. The top of the phantom in each trial had worse correction than the bottom, with the error in the bottom region similar to the correction seen in the MAPA phantom experiment. Thus, we can conclude that references should be placed (if possible) on all sides of the subject to provide good spatial correction.

One limitation of this work is that we have not examined the effect of internal leg perfusion or muscle movement on temperature correction. It can be seen from leg trials #1 and #3 that there are localized regions of increased error in the upper corners of the leg muscle. These regions seem to be very isolated phase changes, almost too isolated to be from perfusion. We speculate that these effects are from slight internal muscle movement to maintain tone, which would cause a phase change that would be misconstrued as temperature change. This could have impact on future hyperthermia treatments of the leg, where these regions could be misconstrued as applied heat.

### **3.6 Conclusion**

In this chapter it has been shown that oil reference materials perform well in correcting MR system “drifts” during PRFS-based temperature measurements. Further, in the presence of large MR system drifts there is, in most cases, an improvement in drift correction by using 8 symmetrically placed oil references in the inner-outer configuration as compared to inner-only or outer-only. There appear to be diminishing returns after this “best” configuration for the cylindrical (MAPA) applicator. Using this combination for a common choice of imaging parameters at 1.5T we are able to achieve a correction of better than 0.5°C in a leg during the MR system drift over a period of an hour or more, typical of a hyperthermia session. For a non-symmetric situation such as a breast applicator, we are still able to achieve similar results (for a phantom) although there is some spatial dependence to the corrected data. For all experiments, the best results were achieved using a higher order interpolating function containing linear and quadratic terms. Finally, while these experiments were performed in only two applicators, the results should help guide application of oil-based referencing to almost any area of the body in which standard PRFS temperature measurement techniques can be applied.

## **4 Development, Characterization, and Optimization of MR Thermometry in Fatty Tissue using IDEAL Fat-Water Separation and Nonlinear Fitting Techniques**

### **4.1 Introduction**

As discussed in the introduction of this thesis, the thermometry errors when using the proton resonant frequency shift (PRFS) method in fat-containing tissue can be very large. In this chapter, two methods are developed to measure temperature in fatty tissue using multi-echo imaging based on the PRFS method and the separation of the fat and water components in the tissue. The first method uses a multi-echo fat-water separation algorithm called Iterative Decomposition of Water and Fat With Echo Asymmetry and Least-Squares Estimation (IDEAL)[138], which can be used to create water-only images that can then be used to calculate temperature changes using normal PRFS techniques [148]. In addition, it uses the fat signal as a reference material which only changes resonant frequency due to changes in the local magnetic field, so it can self-correct the water signal in each voxel for the  $B_0$  field changes discussed in Chapter 3, thus leaving only the temperature PRFS effect, as desired. Hence the IDEAL method involves at least two separate steps and does not directly fit for the temperature. An improved method is developed in this chapter that uses multi-echo methods but processes the data with a different signal model to allow a direct fit for temperature change while accounting for the fat in the voxel. The development and validation of these methods will be discussed in the first half of this chapter.

While these multi-echo techniques can be effective, they are heavily dependent on what echo times are sampled and the composition of the tissue. Since the goal is to measure temperature change, the approach adopted here is to determine a set of echo times to obtain the minimum temperature change noise, i.e., maximize the temperature change signal-to-noise ratio. These values can be found using Monte Carlo simulations, but this is very time consuming, particularly given the parameter space examined in this thesis. The approach adopted here is to use the Cramer-Rao Lower Bound (CRLB) to calculate the temperature noise using much less computational time. The CRLB is the lower bound on the variance of an unbiased estimate [149, 150]. An unbiased estimator is one in which the expected value of the variable (typically the mean) equals the true value.

In the second half of the chapter CRLB analysis is used to characterize the noise in the estimation of temperature using multi-echo fitting techniques. While IDEAL has been characterized with CRLB analysis [151], it was performed with a different signal model, which lacked an explicit temperature change term,  $T2^*$  decay terms, and the parameters accounting for the multiple peaks of fat. CRLB analysis has also been performed for temperature change [152]. However, that work also did not include temperature explicitly in the signal model, instead using the difference in the CRLB of the frequency values of fat and water. The model introduced here includes temperature change explicitly in the signal model and such signal parameters as the fat/water (f/w) ratio,  $T2^*$  of water and fat, TE values of each echo, and the magnitude of temperature change. Finally, the CRLB calculation is confirmed by comparison with Monte Carlo



simulations of a few selected situations and with experiments using phantoms containing solutions with various f/w ratios.

## 4.2 Theoretical Development

### 4.2.1 IDEAL Temperature Method Development

In its most commonly used form, the IDEAL technique uses complex MR image data acquired at three or more echo times to estimate the complex water and fat contributions and  $B_0$  inhomogeneity in each voxel. The complex water and fat signals in a voxel can be modeled by:

$$S(t_n) = (A_w \exp(i\phi_w) + A_f \exp(i\phi_f) \exp(if_{cs}t_n)) \exp(i\Psi t_n) \quad (4.1)$$

where  $A_w \exp(i\phi_w)$  and  $A_f \exp(i\phi_f)$  represent the complex signals from water and fat protons, respectively. The frequency difference due to chemical shift between water and fat is accounted for by the term  $\exp(if_{cs}t_n)$ . Global frequency changes (e.g.  $B_0$  field drift) are accounted for by the  $\Psi t_n$  term. A minimum of three echo times (three complex signal values yielding six real values) is required to solve for the five independent variables,  $A_w$ ,  $A_f$ ,  $\phi_w$ ,  $\phi_f$  and  $\Psi$ . Note that the estimated water and fat signals are complex, with independent phase.

Water protons display a marked frequency shift with temperature change while protons attached to fat do not. As the water frequency changes with temperature, this adds a frequency shift over time in the water term. Since the water signal in IDEAL processing is modeled as being on-resonance, temperature changes result in an apparent phase change in the fat term[153]:

$$S(t_n) = (A_w \exp(i\phi_w) + A_f \exp(i\phi_f) \exp(i\phi_{cs} t_n) \exp(-i\phi_{\Delta T_n})) \exp(i\Psi t_n) \quad (4.2)$$

The apparent phase change in the fat signal is  $\phi_{\Delta T_n} = \omega_{\Delta T} t_n$  where  $\omega_{\Delta T}$  is the frequency shift in radians due to temperature change. This apparent temperature dependent phase change in fat can be solved for by calculating voxel by voxel the fat signal phase angle difference between each reconstructed fat image. However, it was found that the calculation of the phase angle difference between the water and fat signals was more useful. This value references changes due to temperature to the fat signal in the voxel which inherently is not sensitive to temperature but accounts for phase changes due to all other mechanisms, such as  $B_0$  field drift.

The temperature dependency of water protons is approximately 0.01 ppm/°C [154], which in a 1.5T scanner results in a 0.64Hz/°C. The effect of this relatively small frequency shift can be amplified in gradient echo pulse sequence data by using longer echo times (TE) to acquire data. E.g. a TE=4ms yields 0.92 degrees of phase per °C; however, a TE=20ms gives approximately 4.6 degrees of phase per °C.

The complex fat signal is actually comprised of multiple spectral lines at different chemical shift offsets due to the variability of the magnetic microenvironment experienced by protons in the lipid chain. The phase of each fat resonance thus changes differently with time. A number of groups have shown that the accuracy of water-fat separated image methods improve when the fat signal model accounts for this spectral distribution [155, 156]. This is particularly important when acquiring data at longer TE values as the phase differential between lipid groups is further exaggerated. Thus we can

write the complex fat signal with  $N$  lines, relative amplitudes  $\beta_n$  and relative signal phases of  $\phi_n$  as[153]:

$$A_f \exp(i\phi_f) = A_f \sum_{n=1}^N \beta_n \exp(i\Delta\phi_{f_n}) \quad \text{where} \quad \sum_{n=1}^N p_n = 1 \quad (4.3)$$

#### 4.2.2 Nonlinear Fitting Method Development

The nonlinear fitting algorithm uses a Levinberg-Marquardt fitting algorithm to fit for temperature change and local B0 field of MR signal from multiple echoes. The assumed signal model used in the fitting algorithm contains three fat peaks such that the MR signal from a voxel containing both water and fat would be:

$$s(k) = \left( A_w e^{\frac{-TE(k)}{T2_w^*}} e^{2\pi i \alpha f \Delta T} + A_f e^{\frac{-TE(k)}{T2_f^*}} (\beta_1 e^{2\pi i TE(k) \varphi_{fw1}} + \beta_2 e^{2\pi i TE(k) \varphi_{fw2}} + \beta_3 e^{2\pi i TE(k) \varphi_{fw3}}) \right) e^{2\pi i TE(k) \psi} + \varepsilon \quad (4.4)$$

where  $A_w$  and  $A_f$  are the  $TE = 0$  (complex valued) amplitudes at the TR of interest for water and fat respectively.  $T2_w^*$  and  $T2_f^*$  are the  $T2^*$  values for water and fat respectively,  $\alpha$  is the PRFS thermal coefficient (0.01ppm/°C),  $f$  is the imaging frequency at 1.5T (63.87 MHz),  $\varphi_{fw}$  are the frequency differences between the fat peaks and the water peak at a “baseline” temperature,  $T_b$ ,  $\psi$  is the offset from the imaging frequency (magnetic field inhomogeneity affecting both fat and water in a voxel), and  $\varepsilon$  is Gaussian noise with mean=0 and variance= $\sigma_\varepsilon^2$ .  $\beta$  is the relative ratio of the area of each fat peak compared to the area of all fat peaks combined, with all values adding up to 1.  $K$  is the

echo number, for which there are a total of N echo times. The set of echoes described by  $s(k)$  will hereafter be referred to as a Echo Sampling Group (ESG). Finally,  $\Delta T$  is the temperature change from the baseline temperature at which the fat-water frequency differences  $\varphi_{fw}$  would be measured. Theoretically, absolute temperature can be measured by fitting for  $\Delta T$  for a known set of  $T_b$  and  $\varphi_{fw}$ , giving the measured temperature  $T=T_b+\Delta T$ . While the approach would be considerably simplified by using a single peak for the fat-water frequency difference, a number of reports have demonstrated the improvements in water-fat image separation gained by using a multi-peak representation of fat [157, 158].

### 4.2.3 Cramer-Rao Lower Bound model for nonlinear fitting of temperature

To calculate the CRLB, the Fisher Information Matrix (FIM) must be calculated. The FIM contains the sensitivity of the data to the parameters being estimated and the noise. The matrix can be found using the equation:

$$FIM_{kl} = \left\langle \frac{\partial}{\partial v_k} \frac{\partial}{\partial v_l} \ln Pr(s|v) \right\rangle \quad (4.5)$$

Where  $s$  is a vector containing the real and imaginary components of the signal in equation 4.4 and  $v$  is a vector containing the unbiased estimates of the unknowns. The model has four unknowns,  $A_w$ ,  $A_f$ ,  $\psi$ , and  $\Delta T$ , which are shown in the vector  $v$  below:

$$v = [\hat{A}_w \quad \hat{A}_f \quad \hat{\psi} \quad \hat{\Delta T}] \quad (4.6)$$

A matrix representation of the signal in equation 4.4 was derived and used to find the Fisher Information Matrix (FIM) using methods described by Pineda, et al. [151].

When put in matrix form, the signal from equation 4.4 becomes:

$$s(k) = A(\psi, \Delta T)\rho + \varepsilon \quad (4.7)$$

where

$$A = \begin{bmatrix} A_{11} & A_{12} & A_{13} & A_{14} \\ A_{21} & A_{22} & A_{23} & A_{24} \\ \vdots & \vdots & \vdots & \vdots \\ A_{N1} & A_{N2} & A_{N3} & A_{N4} \end{bmatrix}$$

For  $i$ =all odd numbers and  $j=2, 3, 4$ ,  $A_{i1} = e^{-\frac{TE_i}{T2_w^*}} \cos(2\pi TE_i(\alpha f \Delta T + \psi))$ ,  $A_{ij} =$

$$e^{-\frac{TE_i}{T2_f^*}} \beta_j \cos(2\pi TE_i(\varphi_{fwi} + \psi))$$

For  $i$ =all even numbers and  $j=2, 3, 4$ ,  $A_{i1} = e^{-\frac{TE_i}{T2_w^*}} \sin(2\pi TE_i(\alpha f \Delta T + \psi))$ ,  $A_{ij} =$

$$e^{-\frac{TE_i}{T2_f^*}} \beta_j \sin(2\pi TE_i(\varphi_{fwi} + \psi))$$

$$\rho = \begin{bmatrix} A_w \\ A_f \end{bmatrix} \quad s(k) = \begin{bmatrix} S_1^R \\ S_1^I \\ \vdots \\ S_N^R \\ S_N^I \end{bmatrix} \quad \varepsilon = \begin{bmatrix} \varepsilon_1^R \\ \varepsilon_1^I \\ \vdots \\ \varepsilon_N^R \\ \varepsilon_N^I \end{bmatrix}$$

where  $N$  is the total number of echo times acquired.

The matrix representation was used to find the Fisher Information Matrix (FIM) using the methods described by Pineda [151]. Using the unknown variables in  $\rho$  resulted

in a 4x4 FIM, which was calculated using the following equations that are the same as the ones calculated by Pineda.

$$\begin{aligned}
 F(k = 1,2, l = 1,2) &= \frac{1}{\sigma_{\varepsilon}^2} [A^t A]_{kl} \\
 F(k = 1,2, l = 3,4) &= \frac{1}{\sigma_{\varepsilon}^2} [A^t \frac{\partial A}{\partial v_l} \rho]_k \\
 F(k = 3,4, l = 3,4) &= \frac{1}{\sigma_{\varepsilon}^2} \rho^t \frac{\partial A^t}{\partial v_k} \frac{\partial A^t}{\partial v_l} \rho
 \end{aligned} \tag{4.8}$$

The derivations of these equations can be found in Pineda, et al.

The CRLB can be calculated using from the inverse of the FIM. In particular, the variance of the unbiased estimator is calculated from the diagonals of the inverse FIM, where  $\sigma_{v_k}^2 \geq FIM_{kk}^{-1}$ . This variance is valid for cases involving the calculation of temperature change ( $\Delta T$ ) from one set of TE images (or ESG). However, in this study it is assumed that any given  $\Delta T$  will need to have a baseline  $\Delta T_b$  subtracted and thus two time points are to be used to calculate temperature change. Thus, the temperature variance CRLB was calculated twice, often with the first calculation having zero temperature change (but subject to noise) and the second calculation having a nonzero temperature change (also subject to noise) but with all other parameters the same. The variance was then converted to a standard deviation to provide a conventional expression of the error. This standard deviation is referred to as the temperature noise CRLB for the rest of the dissertation.

## 4.3 Experimental Methods

### 4.3.1 Parameterization of Echo Times

For ease of notation, the echo times used were parameterized with three variables, all related to the phase angle between the water and fat signals. First, the starting angle dictates the angle between water and fat at the first TE value. The separation angle then dictates the angle between water and fat that is added to the starting angle for each subsequent TE value. Lastly, the rotation number dictates how many full 360° rotations have occurred between water and fat phases before the starting angle. The equation used to calculate the TE values using these parameters is shown below in equation 4.9.

$$TE(k) = \frac{\left( rotation + \frac{starting\ angle + (k - 1) * separation\ angle}{360} \right)}{\varphi_{fw1}} \quad (4.9)$$

For all the TE values in this dissertation, the  $\varphi_{fw1}$  was assumed to be 222 Hz (bulk methylene peak of fat at 1.5T) unless noted otherwise. A diagram illustrating the relationship between these three variables and the phase angle between water and fat is shown in Figure 4.1.

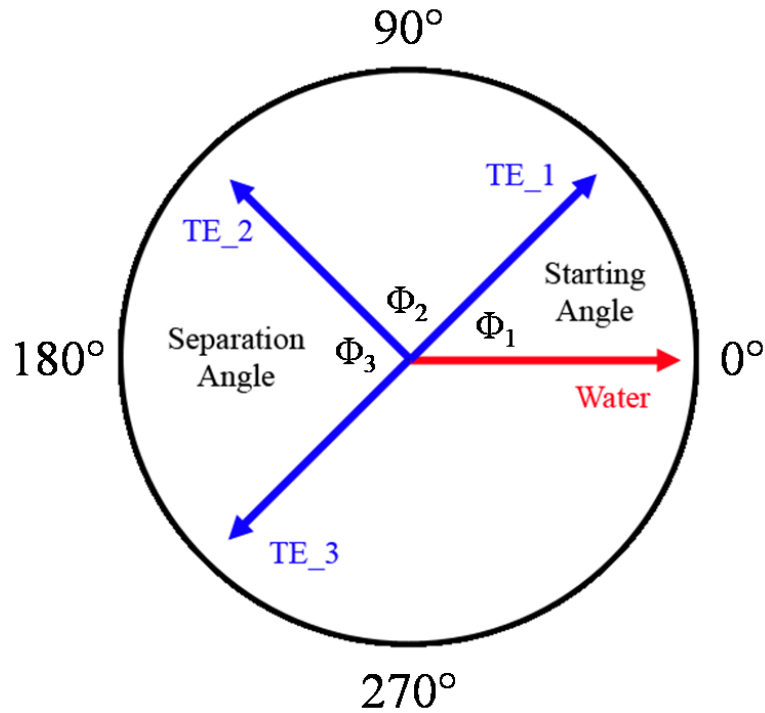


**Figure 4.1:** Diagram explaining the parameterization of the phase difference between the water and fat signals each TE value of an ESG. The red line is the water signal vector at all three echo times. For the purposes of this illustration, it is assumed that the water is on resonance for each TE image. The blue lines are the fat signal vectors at echo times of TE<sub>1</sub>, TE<sub>2</sub>, and TE<sub>3</sub>. The phase angle between the water and fat vectors at TE<sub>1</sub> is indicated by  $\Phi_1$  and is termed the starting angle. For TE<sub>2</sub>, the fat vector has developed an additional  $\Phi_2$  phase term, which is called the separation angle. The phase angle between water and fat at TE<sub>2</sub> is thus  $\Phi_1 + \Phi_2$ . Finally, for TE<sub>3</sub> the fat vector has developed an additional  $\Phi_3$  phase term from the phase in TE<sub>3</sub>. The phase angle between water and fat at TE<sub>3</sub> is  $\Phi_1 + \Phi_2 + \Phi_3$ . For all ESGs discussed in this text, it is assumed that  $\Phi_2 = \Phi_3$

#### 4.3.2 Characterizing the Bias of the IDEAL Method and Nonlinear Fitting Method with Simulation

Simulations were performed with the IDEAL algorithm to determine the noise and bias of the IDEAL algorithm when measuring the temperature change and B<sub>0</sub> field. Only Monte Carlo simulations were performed since it was found that significant bias exists at many starting/separation angles pairs, invalidating the use of the CRLB at those



locations. Similar Monte Carlo simulations were performed with the NLM-Temp algorithm. For each simulation  $A_w=4$ ,  $A_f=6$ ,  $T2^*_w=T2^*_f=40\text{ms}$ ,  $\psi=-12.5\text{Hz}$ ,  $f = 63.87\text{MHz}$ ,  $\phi_{fw1}=-222\text{Hz}$ ,  $\phi_{fw2}=-175\text{Hz}$ ,  $\phi_{fw3}=33\text{Hz}$ ,  $\beta_1=0.82$ ,  $\beta_2=0.11$ , and  $\beta_3=0.07$ . TE values of the ESGs used a rotation of 4 with starting and separation angles that ranged from  $1^\circ$  to  $360^\circ$ , resulting in starting TEs ranging from 18-22 ms and separation times of 1.25-3.75 ms. All echoes were evenly spaced based on a given separation. In that range, ESG starting and separation angle pairs were chosen that were evenly spaced between those ranges. This resulted in reduced matrices of  $72 \times 41$  for the IDEAL algorithm and  $36 \times 21$  for the NLM-Temp algorithm (reduced from the full  $360 \times 360$ ). The NLM-Temp algorithm used less points due to longer computational time. Each location in each matrix was simulated with 5,000 independent samples of equation 4.4 with two  $\Delta T$  settings,  $0^\circ\text{C}$  and  $6^\circ\text{C}$ . The temperature change and  $B_0$  field values at  $\Delta T=0^\circ\text{C}$  were subtracted from the values at  $\Delta T=6^\circ\text{C}$  (to mimic referenced temperature imaging) and the mean calculated. The matrices were then interpolated to provide a  $360 \times 360$  matrix with bias values at each ESG.

### **4.3.3 Characterizing the Nonlinear Fitting Method with Simulation and the CRLB**

#### ***Comparison of the Temperature Noise CRLB Calculation with Monte Carlo Simulation***

The calculated temperature noise CRLB was compared to Monte Carlo simulation results to provide a check on the accuracy of the CRLB calculations. Because the simulation calculation time is quite long for a single set of parameters, only a limited range of parameters was investigated. A nonlinear fitting algorithm based on the

Levinberg-Marquardt fitting method was used (henceforth referred to as NLM-Temp) to fit for temperature change and field offset directly by assuming that the signal is described by  $s(k)$  (equation 4.4). The nonlinear fitting algorithm was programmed in C and each fit was run until it converged to a stable solution.

For each of a number of ESG's, the NLM-Temp algorithm was used to calculate temperature and field offset for 5000 sets of simulated data each with a different noise set for a given ESG with  $A_w=5$ ,  $A_f=5$ ,  $T2^*_w=T2^*_f=40\text{ms}$ , field offset  $\psi = -12.5\text{Hz}$ , and  $\sigma_\epsilon^2=0.5$  (SNR=20 at TE=0). A three peak model for the fat was assumed with one peak at 1.22ppm (222 Hz at 63.85MHz), one at 1.96ppm (175 Hz at 63.85 MHz), and the other at 5.22ppm (-33 Hz at 63.85MHz). The relative ratios ( $\beta$ ) of each peak were 0.82, 0.11, and 0.07, respectively (based on measured ratios of fat peak areas taken from MR spectra of the peanut oil). There were two iterations of the 5000 simulated data sets for each ESG, one with  $\Delta T=0^\circ\text{C}$  and another with  $\Delta T=10^\circ\text{C}$ . The standard deviation of the temperature measurement was calculated by subtracting the 5000 values at  $0^\circ\text{C}$  from the 5000 values at  $10^\circ\text{C}$  and calculating the standard deviation of the resulting differences. This simulates referenced temperature measurement, where one of the measurements is a baseline before temperature change occurs. The standard deviation of the calculated temperature was then compared to the CRLB values calculated with the same signal values. The simulation was conducted for ESG's generated for five starting angles ( $60^\circ$ ,  $120^\circ$ ,  $180^\circ$ ,  $240^\circ$ ,  $300^\circ$ ) and for separation angles from  $1^\circ$  to  $360^\circ$  incremented by  $5^\circ$ . Similar to Dixon fat-water separation methods[138], there will be regions where the NLM-Temp algorithm will fail due to lack of information in the signal model. Thus, the

mean of the simulated results were also calculated to compare with the correct (input) variable value to check for areas of bias or instability of the NLM-Temp algorithm.

### ***Investigation of the Temperature Noise CRLB of Fat-Water Signals for Various Effects***

As shown in the section 4.4.2, the Monte Carlo simulations confirmed the accuracy and regions of applicability of the temperature noise CRLB method. This result motivates the use of the computational efficiency of the temperature noise CRLB method to investigate a wide range of factors that could affect the temperature measurement error:  $T_2^*$  effects, starting TE and TE separation, fat-water frequency difference, fat-water amplitude ratio, the combined effect of these factors and, separately, the number of echoes used. For all calculations (unless otherwise noted),  $\phi_{fw1}=-222$  Hz,  $\phi_{fw2}=-175$  Hz and  $\phi_{fw3}=33$  Hz, the ratios of each peak were  $\beta_1=0.82$ ,  $\beta_2=0.11$  and  $\beta_3=0.07$ , rotation=4 (see below), SNR=1,  $A_w/A_f=1$ .  $T_2^*_w=T_2^*_f=40$ ms, and  $\Delta T=10^\circ\text{C}$ . A SNR of 1 was chosen to allow scaling of the results in this investigation to other SNR values. Since the temperature noise CRLB standard deviation scales linearly with noise, the standard deviation of subsequent experiments can be obtained by dividing the values in this thesis by the SNR of the experiment. The following scenarios were investigated:

#### Examination of $T_2^*$ effects

- One ESG was selected for a range of rotation from 0 to 30
- Starting and separation angles were both to  $150^\circ$  (TE = 1.9-137ms )
- $T_2^*_w$  was kept constant at 40ms,  $T_2^*_f$  set to 20ms, 40ms, and 60ms

- Based on a minimum noise value near rotation=4, all other simulations (below) used a rotation=4 parameter to investigate the best case region

#### Effect of Starting TE and TE spacing

- Performed to gauge effect of uniform or non-uniform echo spacing on  $\Delta T$
- Uniform TE spacing was tested by varying starting and separation angles from  $1^\circ$ - $360^\circ$ , stepping by  $1^\circ$ , at a rotation of 4
- Non-uniform TE spacing was tested by varying starting and separation angles  $\Phi_2$  and  $\Phi_3$  (see to Figure 1) from  $1^\circ$  -  $360^\circ$ , stepping by  $1^\circ$ , independently at a rotation of 4
- Comparisons were made within and between the uniform and non-uniform results

#### Effect of Fat-Water Frequency Difference

- Performed based on report by McDannold et al. of frequency difference in breast between water and bulk methylene peaks from 3 to 3.75ppm (190-240 Hz at 1.5T) [159]
- Three  $\phi_{fw1}$  values were used: 202, 212 and 222 Hz
- Starting and separation angles were varied from  $1^\circ$  -  $360^\circ$ , stepping by  $1^\circ$ , at a rotation of 4
- Relative fat frequency offsets were preserved ( $\phi_{fw1} - \phi_{fw2} = -47$  Hz and  $\phi_{fw1} - \phi_{fw3} = -255$  Hz)
- $\Delta T$  was incremented from 0 to  $20^\circ\text{C}$  in increments of  $5^\circ\text{C}$  for  $\phi_{fw1}=222$  Hz

### Effect of Fat/Water Signal Ratio

- Performed due to variability of fat-water ratio in various areas of the body
- Initially, starting and separation angles were varied from  $1^\circ$  -  $360^\circ$ , stepping by  $1^\circ$ , at a rotation of 4 for various f/w ratios
- Based on equivalent noise changes for varying f/w ratios, an in-depth study was performed on just one starting/separation angle pair
- Starting and separation angles were set to  $150^\circ$ , rotation 4, while the f/w ratio was adjusted from 1% to 99% fat signal in increments of 1%

### Combined Effect of Fat-Water Frequency Difference, Fat/Water Ratio, and Temperature Change

- Performed to investigate which ESGs would minimize the large noise variations seen when each of these three parameters were varied individually
- Starting and separation angles were varied from  $1^\circ$  -  $360^\circ$ , step  $1^\circ$ , at a rotation of 4
- $\phi_{fw1}$  values were varied from 190 - 240 Hz, in 1 Hz increments
- Relative fat frequency offset were preserved ( $\phi_{fw1} - \phi_{fw2} = -47$  Hz and  $\phi_{fw1} - \phi_{fw3} = -255$  Hz)
- f/w signal ratios were varied from 10% - 90% fat, in increments of 10%
- $\Delta T$  was varied from  $0^\circ$  -  $15^\circ\text{C}$  in  $5^\circ$  increments
- The standard deviation of all CRLB values for a given ESG was calculated to find the ESG(s) that had minimum noise variation due all the permutations performed for the ESG

### Effect of Number of Echoes Used

- Number of echoes were varied from 3 – 15
- Starting and separation angles were varied from  $1^\circ$  -  $360^\circ$ , step  $1^\circ$ , at a rotation of 4

#### **4.3.4 Phantom Construction, Spectral and Fat-Water Composition Determination**

Phantom measurements were compared to the theoretical temperature noise CRLB calculations. Three different phantoms were constructed. Each phantom was an oil-in-water gelatin phantom using the recipe described in Wyatt et al. [142] as modified from Madsen et. al. [144]. Peanut oil was used since it has been used in previous papers [157] to mimic body fat and has a well-documented spectrum. The phantoms were made with different f/w concentrations, with ratios of 70:30, 50:50, and 30:70 water to fat. The first two phantoms were contained in 5 inch diameter HDPE cylinders of 10 inch length, while the 30:70 phantom was contained in a 4.25 inch diameter PVC cylinder of 7 inch length (the smaller volume was needed to create a homogenous phantom of this composition). Four catheters were inserted along the length of each phantom, one at the center of each cylinder and three near the outside edge of the phantom at  $120^\circ$  offsets from each other. The catheters allowed the insertion of invasive fiber optic probes (Lumasense Technologies, Santa Clara, CA) to measure absolute temperature inside the phantom.

The frequencies and relative amplitude ratios of the fat peaks were measured using single voxel, short echo time MR Point Resolved Spectroscopy (PRESS) to determine fat peak frequency values and relative amplitude ratios. Acquisition parameters

were TR=5s, TE=30ms, SW=2000Hz, 2048 points and 8 averages with no water suppression. PRESS voxels were acquired from  $1\text{cm}^3$  voxels centered at each of the catheter locations midway along the length of each phantom to determine the homogeneity of each solution. The SITools-FITT software package [160] was used to fit areas and frequencies beneath a single water peak, and six lipid peaks (Figure 4.2). The scanning was performed on a 3T Trio MR scanner (Siemens Medical Systems, Erlangen, Germany)[153].

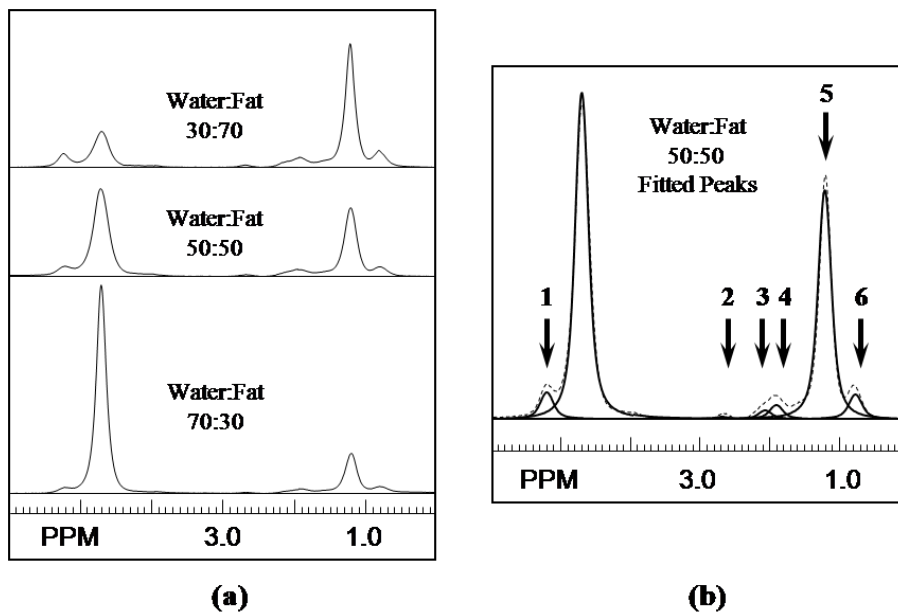


**Figure 4.2:** (a) PRESS spectra at the center of each phantom. (b) Fits to six spectral lines of the 50:50 spectrum. Notice in (a) how the ratios of the height of the water and fat peaks corresponds well with the ratios of the materials in the phantom

Data was also acquired for fitting of the  $A_w$ ,  $A_f$ ,  $T2^*_w$ , and  $T2^*_f$  values. Images of the phantoms were acquired for nine 3-echo ESGs chosen with a varying starting angles and a separation angle of  $120^\circ$ . TE parameters for these ESGs are shown in Table 4.1. TE values ranged from 6.3ms to 31.7ms. The parameters in Table 4.1 were chosen to

enable robust fitting of the  $T2^*$  and amplitude values of both the fat and water signals. Images were acquired from a 1 cm thick slice on a 1.5T GE Signa HDX (General Electric, Milwaukee, WI) with a 2D axial SPGR (spoiled-gradient echo) sequence with  $TR=51\text{ms}$ , Flip angle= $30^\circ$ ,  $BW=15.6\text{ kHz}$ ,  $FOV = 24\text{cm}$ ,  $128 \times 128$ , and  $NEX=2.0$ .

**Table 4.1:** TE parameters for the MP-IDEAL ESGs. All angle values are in  $^\circ\text{C}$ .

rotation	starting angle	separation angle
1	150	120
2	165	120
3	125	120
3	190	120
3	310	120
4	120	120
4	190	120
5	135	120
6	135	120

The nine 3-echo ESG images were processed with an offline implementation of the multi-peak IDEAL (MP-IDEAL) algorithm described by Yu, et.al. [157]. The  $A_w$ ,  $A_f$ ,  $T2^*_w$ , and  $T2^*_f$  values of each phantom were fit using a nonlinear Levinberg-Marquardt algorithm that used the nine water and fat images resulting from the IDEAL separation. All of these calculations were performed in Matlab (The Mathworks, Inc., Natick, MA). Referring to Figure 2b, only peaks 1, 4, and 5 were included. Peak 3 was combined with peak 4 and peak 6 was combined with peak 5. Peak 2 was ignored due to its small amplitude. These adjustments were made to simplify the MP-IDEAL calculations.



#### 4.3.5 Phantom Experiments to Validate IDEAL Method

Each phantom was actively heated, independent of the other two, in the MAPA applicator[161] with power applied to all 4 RF antennas. A water bolus sleeve (see Figure 3a) was used to improve coupling of the RF energy at 140 MHz into the water-fat phantom. D<sub>2</sub>O (99.8% pure, Sigma Aldrich #617385, St. Louis, MO) was used to fill the bolus sleeve to minimize image artifacts from convection currents. Four narrow, cylindrical references containing only silicone oil were located both inside the water bolus and along the sides of the MAPA. These references provide pure fat signals for B<sub>0</sub> field drift corrections during PRFS measurements, but were not necessary for this experiment. Each water-fat phantom was positioned in the center of the MAPA and RF heating was applied in an OFF-ON-OFF pattern. During the ON period, all four RF antennae were set to 15W continuous power to heat the phantom with a symmetric distribution. Fiber optic temperature probes (Lumasense Technologies, Santa Clara, CA) were centered within the MR slice and recorded temperatures every 10 seconds for the duration of the experiment. A text file record of fiber optic temperature measurements was saved offline for comparison to reconstructed temperature maps.

Complex MR image data was acquired on a GE Signa HDX 1.5T system (GE Healthcare, Waukesha, WI). Five gradient echo images (GRE) were taken at each time point. A single slice was positioned at the center of the MAPA/phantom with 6mm slice thickness, TE=[16.78, 19.84, 22.91, 25.98, 29.04ms], TR=34ms, FOV=30cm, 128x128 points, receive band width 32kHz and NEX=2. Nominal voxel size was 2.4 x 2.4 x 6mm. Five echo times were acquired to permit the temperature map algorithm to determine if a five echo fit permitted a better estimate than a three echo fit. Total data acquisition for the

five echoes was approximately two minutes. Over 52 minutes, 25 time points were acquired with approximately 20 minutes heat OFF, 20 minutes with heat ON (15W x 4 channels), and 12 minutes heat OFF. Complex image data were transferred offline and temperature maps reconstructed using in-house software written in IDL (ITT-VIS, Boulder, CO).

Standard IDEAL image reconstruction, without  $T_2^*$  correction, yielded complex image estimates for water and fat using both three and five echo reconstruction algorithms. Heating resulted in the addition of an apparent complex phase component to the fat image. In each voxel, the phase accumulation due to temperature was calculated by taking the difference between the current water-fat phase angle,  $\text{atan}(\phi_w - \phi_f)$ , and the water-fat phase angle for the previous image acquired. The total phase change due to heating was calculated as the sum of the changes at each time point. Based on the assumption that the phase change due to temperature  $\phi_{\Delta T n} = \omega_{\Delta T} t_n$  was small between the  $N$  echoes acquired for the IDEAL reconstruction, the temperature change was be calculated via  $\phi_{\Delta T} \sim \omega_{\Delta T} TE_{N/2}$ , where  $TE_{N/2}$  was the middle TE value collected for IDEAL reconstruction. Each IDEAL image reconstruction was performed independent of all other time points. The above assumptions were made based on an expectation for smoothly distributed temperature changes. Because image noise from each data collection can lead to small variations in IDEAL image reconstruction, variations in temperature measurements should also be independent of time points and related to image noise.

#### **4.3.6 Experimental Confirmation of Temperature Noise CRLB for Nonlinear Temperature Algorithm**

##### *Temperature Noise Measurements*

Phantom comparisons to theoretical CRLB and Monte Carlo estimates were performed using several selected TE spacing combinations that distinctly illustrate different noise behavior seen in the calculations. Phantoms were equilibrated overnight to MR scanner room temperature and were scanned using the standard GE CP head coil. Fiber optic temperature probes (Lumasense Technologies, Santa Clara, CA) were inserted into each of four catheters in the phantom and centered in the slice of interest. Temperature data was acquired from each probe every 10 seconds during the experiment. MR scan parameters were the same as those used above for the phantom composition measurements. ESGs were acquired for 3-echo, 5-echo and 7-echo combinations. The starting angle and separation angles of each ESG are shown in Table 4.2 (also indicated by asterisks in Figure 4.7). Each ESG was acquired six times consecutively, to allow for referenced temperature imaging and averaging of the results. No heat was applied to the phantom during these measurements.

**Table 4.2:** TE parameters for the ESGs to confirm the temperature noise CRLB values. These values match the points that are marked in Figure 4.7. For each of the ESG values, rotation=4 and  $\phi_{fw1}=222\text{Hz}$ . Equation 4.9 was used to calculate the TE values. All angle values are in  $^{\circ}\text{C}$ .

3-echo				5-echo		7-echo	
Starting Angle	Separation Angle	Starting Angle	Separation Angle	Starting Angle	Separation Angle	Starting Angle	Separation Angle
20	176	218	238	93	47	88	32
45	238	235	285	152	105	135	74
75	192	261	279	194	219	161	157
108	80	279	190	208	253	283	27
146	123	283	27	337	105	328	74
181	179	305	123				
197	84	345	184				

#### *Phantom Temperature Noise Data Analysis*

Images for the ESG's in Table 2 were analyzed with the NLM-Temp algorithm. The  $A_w$ ,  $A_f$ , and  $T2^*$  were fixed in the NLM-Temp calculation base on values from the MP-IDEAL measurements in the phantom composition analysis. The fat peaks values used for the fit were the same as the values used for MP-IDEAL.

The temperature change,  $\Delta T$ , was calculated for all six image sets of an ESG. The first temperature image was then subtracted from the other five to produce  $\Delta T$  images referenced to a baseline temperature. A 1000 pixel ROI (approximately 33x31) was chosen from inside the phantom. With no heat applied to the phantom and a small ROI, the temperature change in each of the five referenced images was assumed to be

approximately 0°C. Calculating the standard deviation across all pixels in all the images thus approximates the error of the  $\Delta T$  measurement. We report the average value of the standard deviation of the pixels in each of the five images as our final measure of temperature noise.

To express the error of our measured standard deviation values, the theoretical standard error was calculated using the standard formula given below [162]

$$\sigma_{theoretical} = \frac{\sigma_{CRLB}}{\sqrt{2P}} \quad (4.10)$$

where  $\sigma_{theoretical}$  is the standard error,  $\sigma_{CRLB}$  is the calculated CRLB standard deviation, and  $P$  is the number of samples (or pixels in this case). The number of pixels used for each ESG was 5000 (since there were five 1000 point samples).

## **4.4 Results**

### **4.4.1 Bias of the IDEAL algorithm**

Maps of the mean temperature and mean field differences for IDEAL and the nonlinear fit methods are shown in Figures 4.3 and 4.4. Temperature and field values measured with the IDEAL algorithm are biased in certain regions, varying from the respective true values of 6°C and 0 Hz. However, there are regions where the values are unbiased, but they are limited in range.

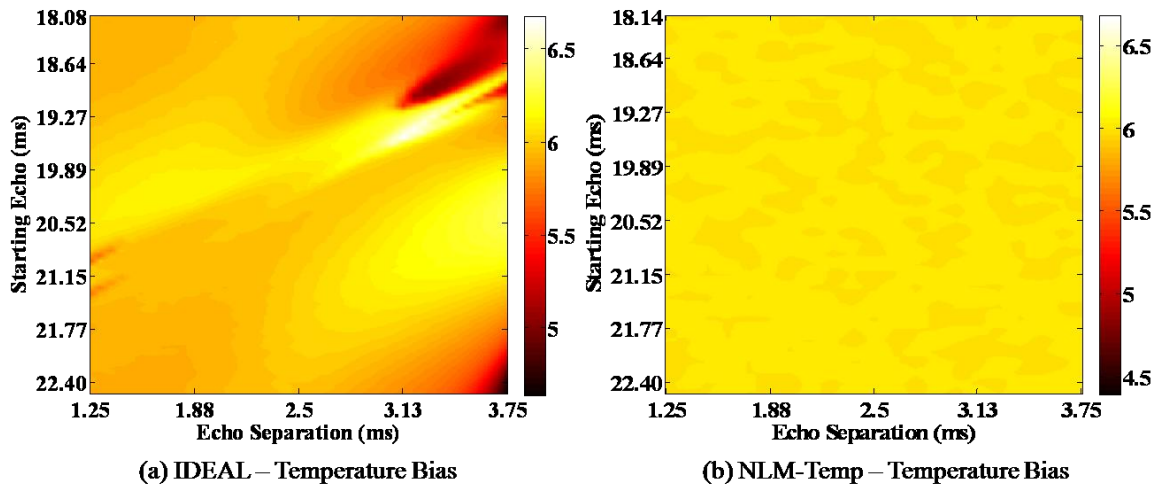


**Figure 4.3:** Temperature bias of (a) IDEAL and (b) NLM-Temp algorithm. Notice that that (a) has large bias in many regions while (b) is spatially uniform and non-biased.

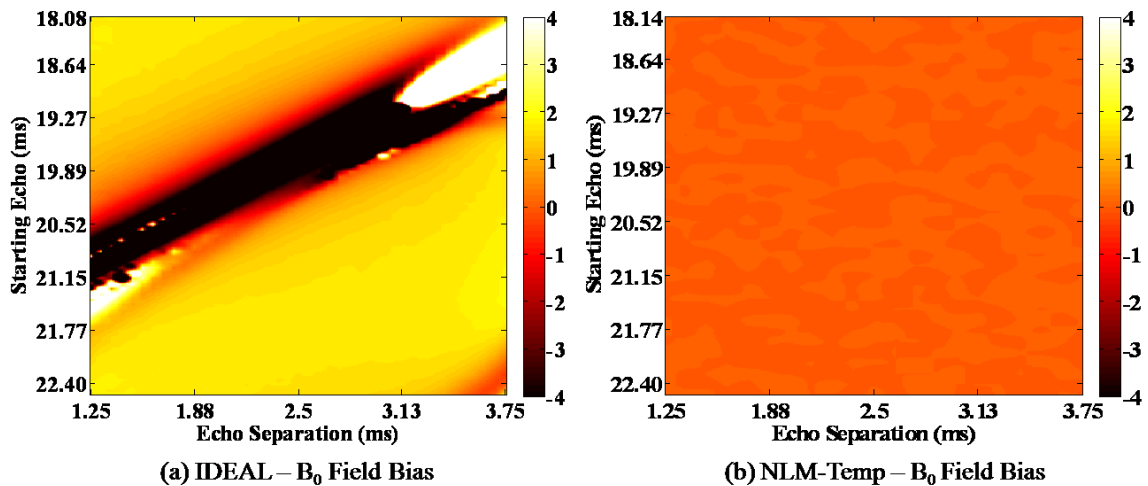


**Figure 4.4:**  $B_0$  field bias of (a) IDEAL and (b) NLM-Temp algorithm. Notice that (a) has large bias in many regions while (b) is spatially uniform and non-biased.

#### 4.4.2 Characterizing the Noise Behavior of the Nonlinear Temperature Algorithm

##### *Agreement of the Cramer-Rao Lower Bound Temperature Noise Calculation with Simulation*

An example of fat-water phantom PRESS spectra are shown in Figure 4.2(a) from center voxels positioned in the 30:70, 50:50 and 70:30 phantoms. Also shown in Figure 4.2(b) is an example of a fit of the spectrum from the 50:50 phantom to a set of Lorentzian functions. A total of twelve spectra were fitted across the three phantoms, one spectra at each catheter location. Six spectral lines were used to characterize the fat as indicated by the numbered arrows in Figure 4.2(b).

Fat peak areas were normalized to the total fat area. The mean chemical shift (PPM, referenced to water) and relative area ( $\beta$  in equation 1) of each fat peak found from the PRESS spectra were: 5.22, 2.69, 1.96, 1.21 and 0.78 PPM and 0.071, 0.012, 0.091, 0.734 and 0.092 for the respective peaks. Standard deviations for the fit values of  $\beta$  in the 50:50 phantom were on the order of 2-8% except for the smallest peak at 2.69 PPM with a 20% standard deviation. The fit values of  $A_w$ ,  $A_f$ ,  $T2^*_w$ ,  $T2^*_f$ , and average SNR for each set of experiments and phantoms are shown in Table 3. For each simulation  $\phi_{fw1}=-222.84$  Hz,  $\phi_{fw2}=-174.95$  Hz,  $\phi_{fw3}=33.2$ Hz,  $\beta_1=0.826$ ,  $\beta_2=0.103$ , and  $\beta_3=0.071$ . These were derived from the PRESS values discussed in the previous paragraph. These values were used in all subsequent Monte Carlo, temperature noise CRLB and phantom comparison investigations.

The comparison of simulation results using NLM-Temp and the temperature noise CRLB values are shown in Figure 4.5 for starting angles of 60°, 120°, 180°, 240°, and 300°.

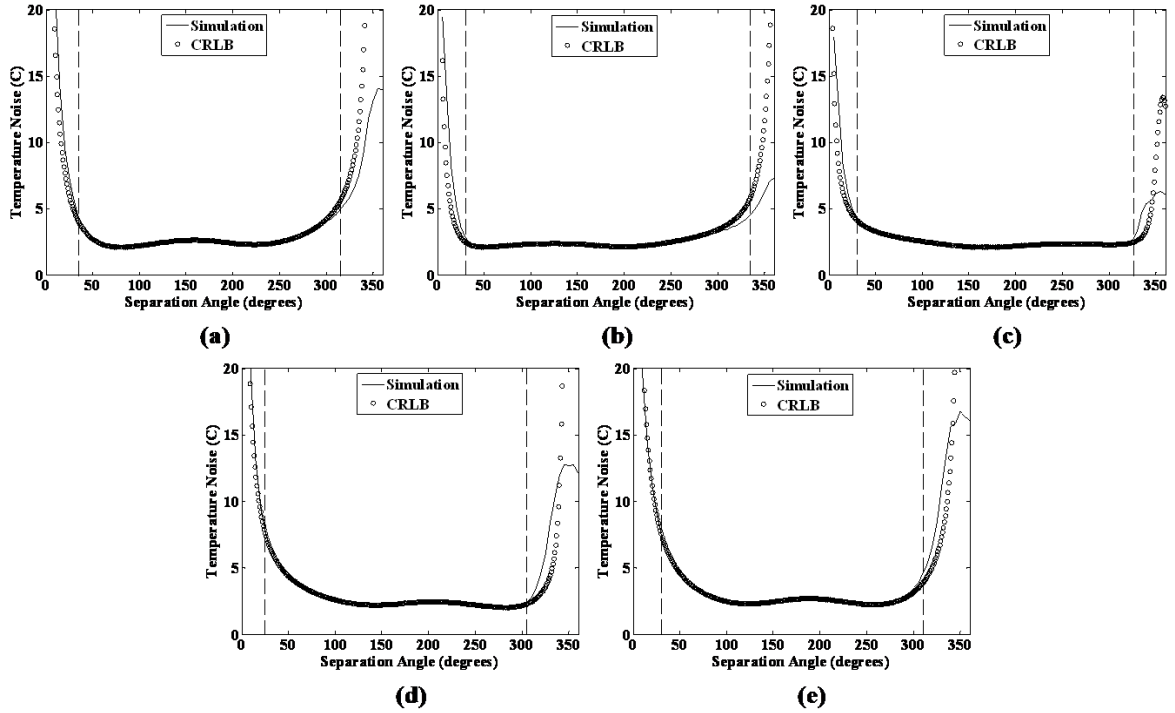


**Figure 4.5:** Simulation temperature noise values from NLM-Temp plotted along with the CRLB temperature noise calculations, both using the same input values. These are shown from separation angle to 1° to 360° and for starting angles of (a) 60° (b) 120° (c) 180° (d) 240° (e) 300°. The regions between the dashed lines and the edges are regions of estimation bias where the mean of the simulation deviated from the true value (by >1%). From all plots it can be seen that within the non-biased regions, the CRLB values match the simulated values.

### *Investigation of the Temperature Noise CRLB of Fat-Water Signals for Various Effects*

#### *Examination of $T2^*$ effects*

The temperature noise CRLB values as a function of rotation for varying  $T2^*_f$  values and a constant  $T2^*_w = 40\text{ms}$  are shown in Figure 4.6. The general trend indicates a minimum near rotation=4.



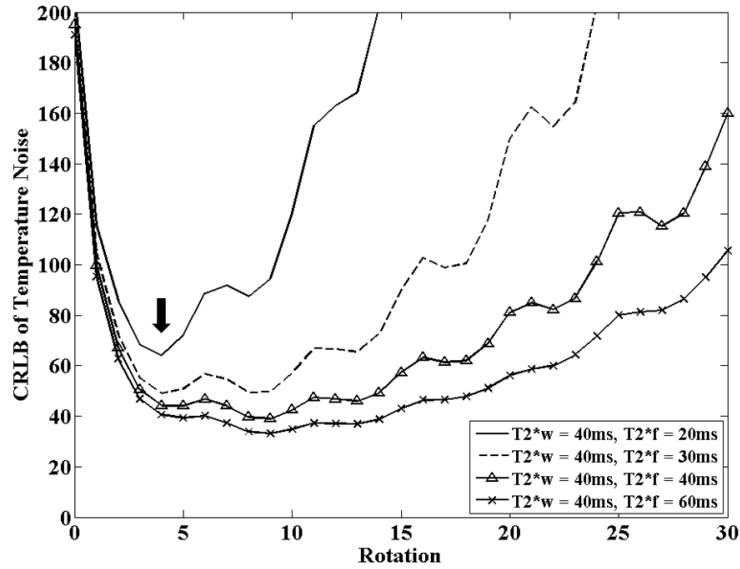


**Figure 4.6:** Temperature noise CRLB across several rotations for a constant  $T2^*_w$  and changing  $T2^*_f$ . Performed with  $SNR = 1$ ,  $A_w/A_f = 1$ ,  $\Delta T = 10^\circ C$ , and  $\psi = -12.5$  Hz. Note the minimum noise for all plots near rotation=4, as noted by the arrow in the figure.

#### *Effect of Starting TE and TE spacing*

The temperature noise CRLB values are shown as 2D intensity images in Figure 4.7 for 3-echo, 5-echo and 7-echo ESGs with rotation=4, starting and separation angles from  $1^\circ$ - $360^\circ$ , stepping by  $1^\circ$ . These images will be referred to as temperature noise CRLB maps. The white regions in Figure 4.7 are regions outside of the range of the colormap, since a narrow range was needed to emphasize the structure of the temperature noise CRLB maps in regions of low noise. The minimum temperature noise CRLB of the non-uniform echo spacing was only 2.4% smaller than the minimum temperature noise of the uniform echo spacing.

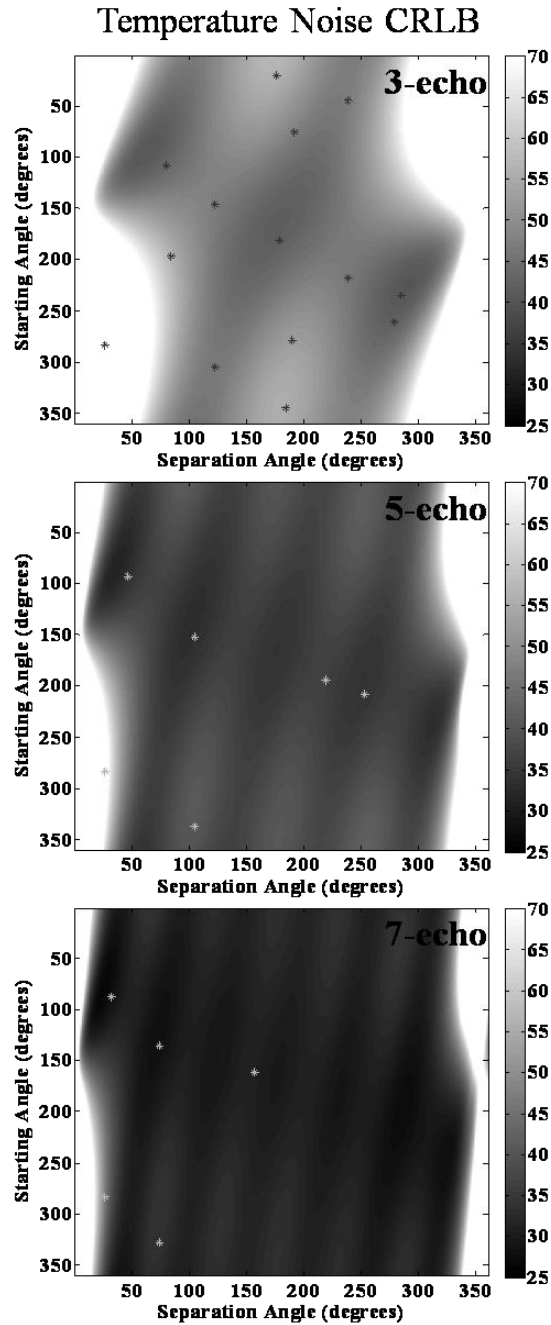


**Figure 4.7:** Temperature noise CRLB maps for 3-echo, 5-echo, and 7-echo ESGs with starting and separation angles ranging from  $1^\circ$  to  $360^\circ$ . The color bar is in units of  $^\circ\text{C}$ . The asterisks represent the ESGs sampled in the phantom experiments. Notice that each image has temperature noise minima and the number of minima corresponds to the number of echoes. Also, the temperature noise in all regions decreases with an increased number of echoes.

### Effect of Fat-Water Frequency Difference

The effects of different fat-water frequency values on the temperature noise CRLB values are shown in 2D temperature noise CRLB maps in Figure 4.8.

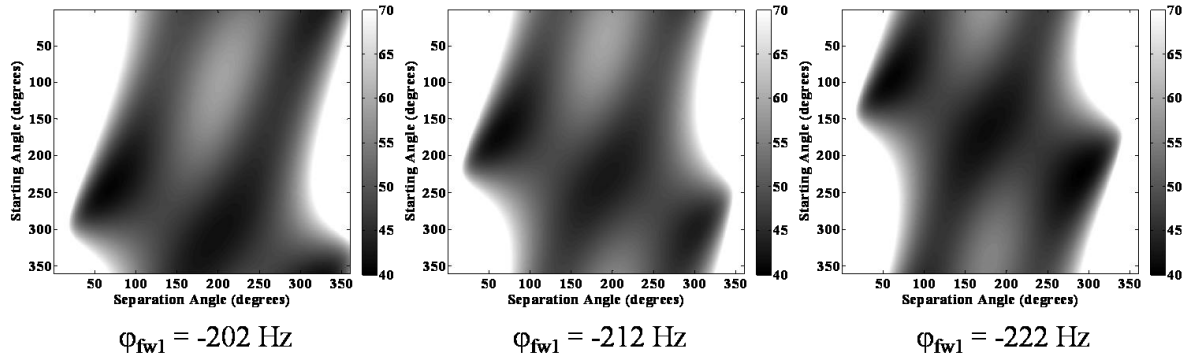


**Figure 4.8:** Temperature noise CRLB maps as a function of starting angle and separation angle with different values of fat-water frequency differences. The frequency difference between the fat peaks was preserved so that  $\varphi_{fw1} - \varphi_{fw2} = -47 \text{ Hz}$  and  $\varphi_{fw1} - \varphi_{fw3} = -255 \text{ Hz}$ . The color bar is in units of  $^{\circ}\text{C}$ . Notice the shift along the starting angle (vertical axis) with changes in the fat-water frequency difference. However, the overall shape of the temperature noise remains constant.

### Effect of Fat/Water Signal Ratio

The change of the temperature noise CRLB values with varying f/w ( $A_f/A_w$ ) signal ratio for angle =  $150^{\circ}$  and separation angle =  $150^{\circ}$  is shown in Figure 4.9.

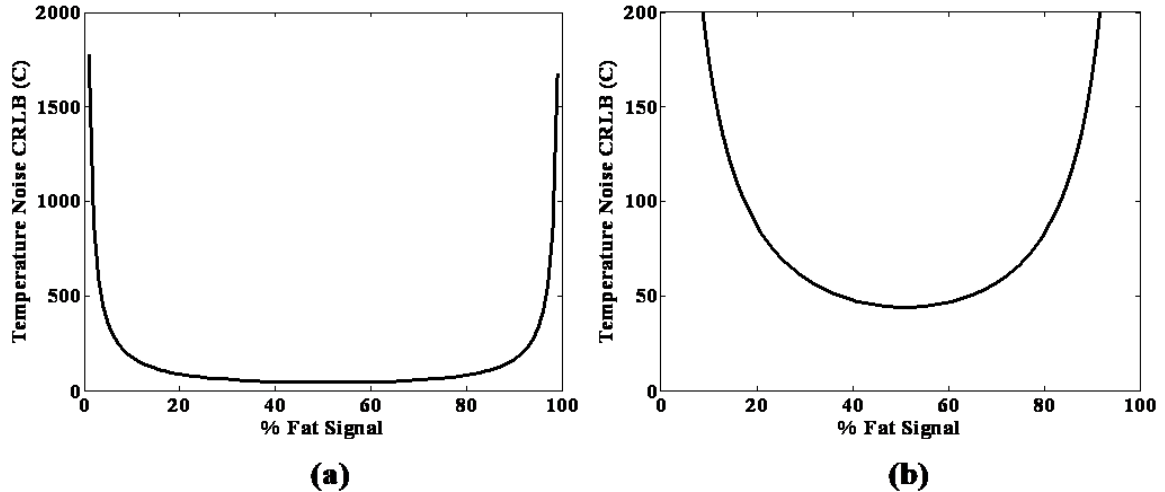


**Figure 4.9:** Temperature noise CRLB for starting angle and separation angle =  $150^\circ$  for a varying fat signal %. (a) behavior at the low and high % fat (b) zoomed in y axis to show the behavior at medium % fat. These plots demonstrate that the minimum temperature noise occurs with equal amounts of fat and water signal. Also, near the boundaries of pure water or pure fat, the temperature noise increases exponentially.

*Combined Effect of Fat-Water Frequency Difference, Fat/Water Signal Ratio, and Temperature Change*

Because the previously mentioned variables (fat-water frequency difference,  $\Delta T$ , and f/w signal ratio) have significant individual effects on the temperature noise CRLB, a multifactorial calculation was constructed to allow selection of a starting and separation angle pair that would produce minimal changes in the temperature noise across many situations (Figure 4.10). The standard deviation of the combined CRLB temperature values from varying  $\Delta T$ , f/w signal ratio, and fat-water frequency separation are shown. This map shows that the region with the least combined noise occurs near a starting angle =  $215^\circ$  and a separation angle =  $240^\circ$  with a combined temperature noise equal to  $45.58^\circ\text{C}$  (at SNR = 1).

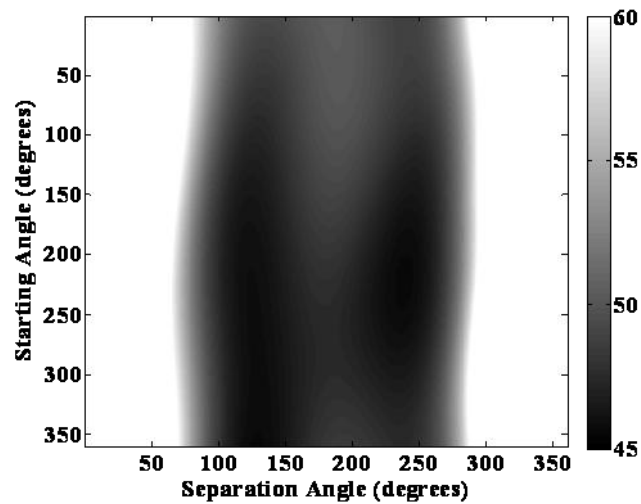


**Figure 4.10:** Multifactorial, combined simulation showing temperature noise CRLB as a function of starting angle and separation angle. Each point represents the combined temperature noise due to variation of  $\phi_{fw1}$  from -190 to -240 Hz by 1 Hz, fat-water signal ratios varied from 10% fat to 90% fat, in increments of 10% and temperature change varied from 0°C to 15°C in 5°C increments. The color bar is in units of °C. As seen in the figure, there is a temperature noise minima at starting angle = 215° and a separation angle = 240°.

*Effect of number of echoes used*

Lastly, the behavior of the temperature noise when the number of echoes was adjusted was examined. The minimum CRLB error with the number of echoes ranging of 3 to 15 echoes is shown in Figure 4.11.

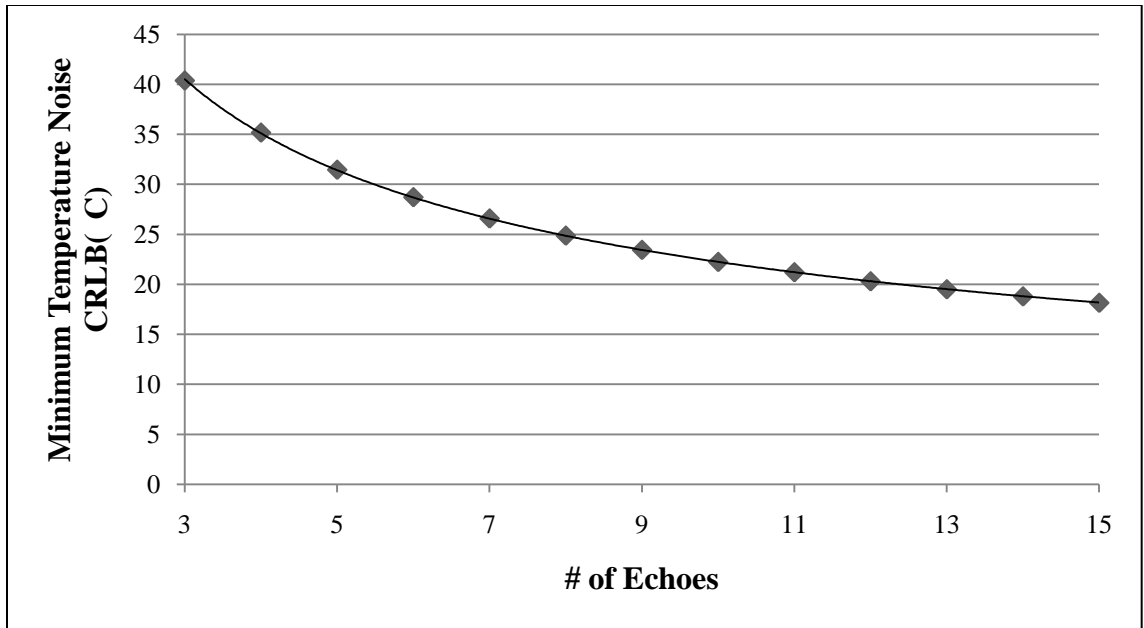


**Figure 4.11:** CRLB minimum temperature noise for number of echoes,  $N$ , varying from 3 to 15. The points follow a power function on the order of  $x^{0.5}$  ( $70.03x^{0.49}$  with  $R^2=1.0$ ), which is similar to the improvement seen when performing signal averaging.

#### 4.4.3 Phantom Construction, Spectral and Composition Determination

An example of water-fat phantom PRESS spectra are shown in Figure 1 from center voxels positioned in the (a) 30:70, (b) 50:50 and (c) 70:30 phantoms. An example of fitting the center spectrum from the 50:50 water-fat phantom is shown in Figure 2. A total of twelve spectra were fit across three phantoms. Six spectral lines were used to characterize the fat as indicated by the arrows in Figure 2. Due to their similarity, fat peaks 3 and 4 were combined to simplify the IDEAL calculation. Fat peak areas were normalized to the total fat area. The mean PPM and area of each peak was used in the IDEAL reconstruction, these were: 5.22, 2.69, 1.96, 1.21 and 0.78 PPM and 0.071, 0.012, 0.091, 0.734 and 0.092 for the respective areas. Standard deviations for fitted values in

the 50:50 phantom were on the order of 2-8% except for the smallest peak at 2.69 PPM with a 20% standard deviation.

The signal fit for the water and fat magnitudes is shown compared to the MP-IDEAL signal magnitude at each data point in Figure 4.12.

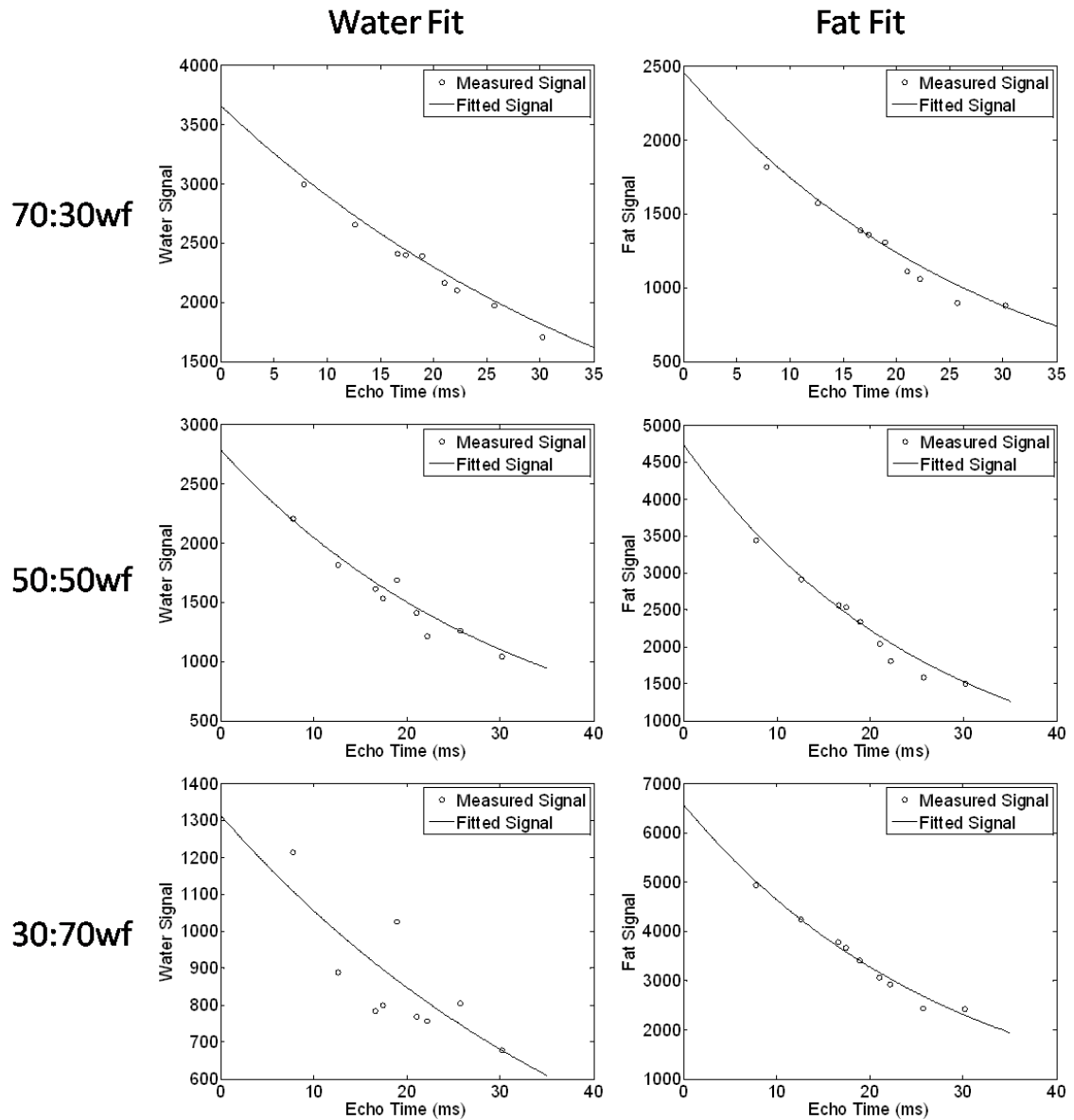


**Figure 4.12:** Measured vs. Fit water and fat signal for each fat-water phantom. These plots show that our fits of the water and fat magnitude and T2\* values are appropriate, since the fit line lies along most of the measured water and fat signal values.

A comparison of the total measured signal to the combined fit signal values is shown in Figure 4.13. The  $A_w$ ,  $A_f$ ,  $T2^*_w$ ,  $T2^*_f$ , and SNR values for each phantom can be found in Table 4.3.

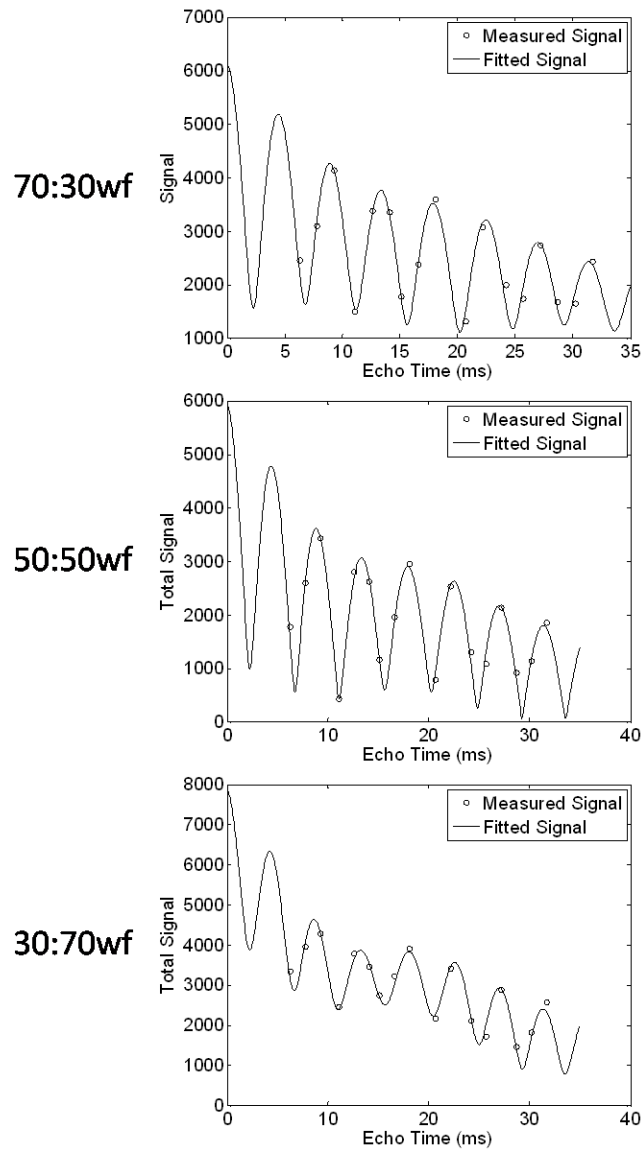


**Figure 4.13:** Measured vs. Fit total signal for each fat-water phantom. These plots show that our fits of the water and fat magnitude and  $T2^*$  values are appropriate, since the fit line of the total signal lies along the measured total signal values.



**Table 4.3:** Calculated  $A_w$ ,  $A_f$ ,  $T2^*_w$ ,  $T2^*_f$ , and SNR for all fat-water phantom experiments. SNR is calculated at TE = 0, so the equation is  $SNR = (A_w + A_f) / \sigma^2$ .

phantom	# of echoes	$A_w$	$A_f$	$T2^*_w$ (ms)	$T2^*_f$ (ms)	SNR
70:30	3	3662.9	2459.5	42.9	29.1	276.5
	5 and 7	3031.7	2114.9	41.3	27.2	312.5
50:50	3	2789.7	4737.1	32.3	26.5	331.7
	5 and 7	2120.1	3816.1	34.3	27.1	351.0
30:70	3	1275.1	6618.9	49.8	28.4	435.4
	5 and 7	1313.3	6567.8	45.6	28.7	429.3

#### 4.4.4 Phantom Experiments to Validate IDEAL Method

Figure 4.14 shows (a) the MAPA RF heating device and (b) a representative axial GRE image for TE=16.1 ms with the water-fat phantom (gray, center) supported by the D<sub>2</sub>O bolus sleeve (dark) with fat filled outer oil references (gray). The dotted yellow circle indicates outer diameter of the MAPA former. The red square indicates the region of the acquired images that was post-processed for temperature maps. Signal to noise (SNR) for all water-fat phantoms ranged between 12-100:1 depending on water-fat ratio and in/out phase characteristics due to TE. Figure 4.15 shows the results for IDEAL reconstructed (a,c) water-only images and (b,d) fat-only images for the 50:50 phantom. Figure 4.15 (a,b) were constructed from data with no heating applied. Figure 4.15 (c,d) were constructed from data taken at maximum temperature change at time equal approximately 42 minutes. Similarly homogeneous water-fat images were reconstructed for all phantoms, although, as in Figure 4(c), some slight shading was seen in the water

images in areas with the highest temperature changes due to  $T_1$  changes due to temperature.

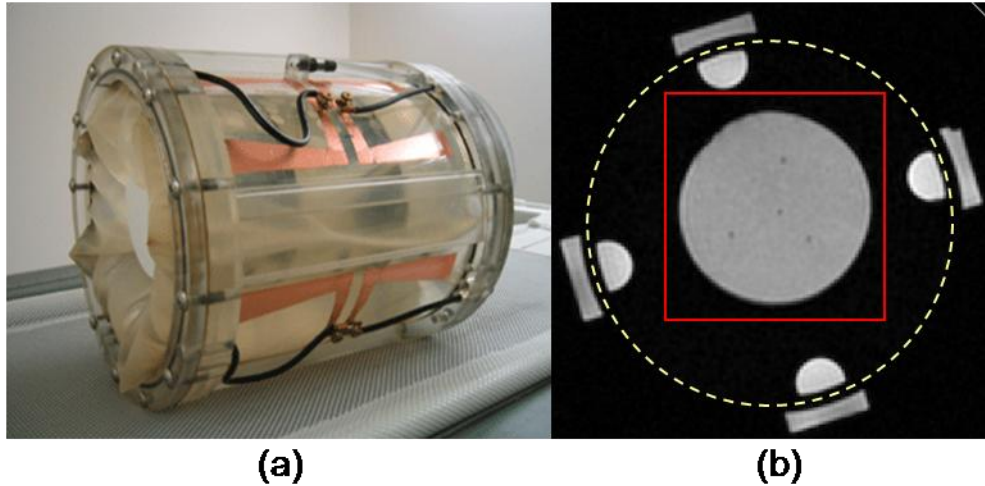


**Figure 4.14:** (a) Mini annular phased array (MAPA) RF heating device. (b) Axial magnitude GRE image with  $TE=16.1ms$  of 50:50 water-fat phantom (inner gray circle) surrounded by a  $D_2O$  filled bolus (black) with fat filled half-cylinder internal and rectangular outer references. The dotted yellow circle indicates outer diameter of the MAPA former. The red square indicates the region of the acquired images that was post-processed for temperature maps as displayed in subsequent Figures[153].

$B_0$  fields maps reconstructed from the IDEAL algorithm are shown in Figure 4.16 for both the three and five echo reconstructions of the 50:50 phantom at the first time point. Both maps (a,b) show spatially inhomogeneous fields with a range of approximately 20 Hz across the phantom.  $B_0$  field values at the locations of the four fiber optic temperature probes are shown in Figure 4.16 (c,d) for all time points of the experiment. These plots show that the spatially inhomogeneous pattern persists throughout the experiment but also displays a global drift with time.

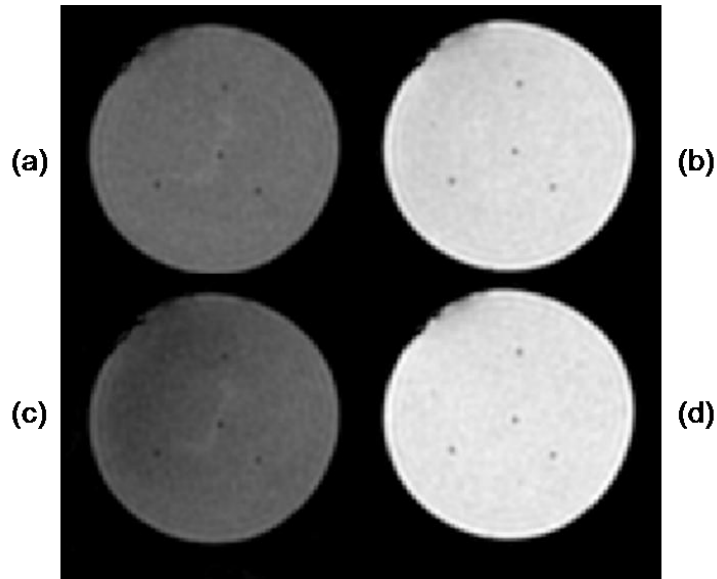


**Figure 4.15:** IDEAL reconstructed (a,c) water-only images and (b,d) fat-only images for phantom with 50:50 water to fat ratio. Images (a,b) were constructed from data with no heating applied. Images (c,d) were constructed from data taken at maximum temperature change, time ~ 42 minutes. Catheters for the four fiber-optic temperature probes can be seen as four small signal hypo-intense areas in the center and around the edge of each phantom[153].

IDEAL calculated temperatures are compared to fiber optic temperature measurements in twelve plots in Figure 4.17[153]. Each of the four fiber optic probe locations in a given phantom are shown vertically while the same fiber optic probe in each of the three phantoms is shown horizontally. The mean of the first 20 fiber optic temperatures has been subtracted from each overall fiber optic plot to enable the relative changes of the IDEAL temperature values to be compared to the absolute fiber optic temperature measurements.

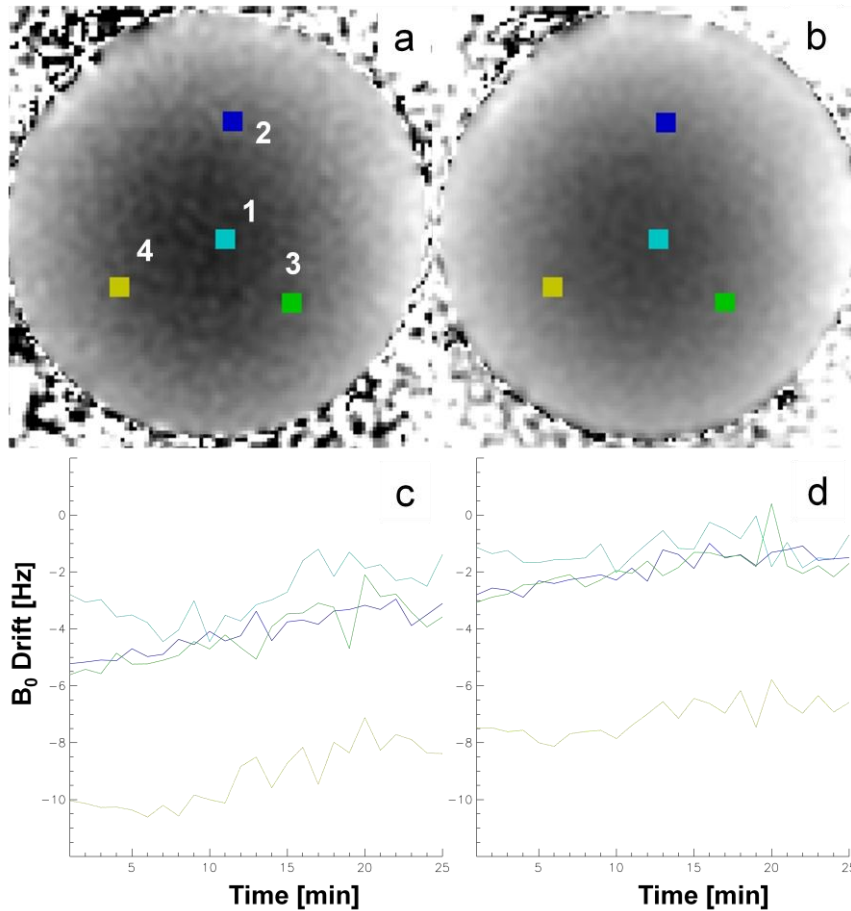


**Figure 4.16:** IDEAL calculated  $B_0$  field maps using (a) three and (b) five echoes in the 50:50 water-fat phantom. The four colored squares marked 1, 2, 3 and 4 show the placement of the 5x5 pixel ROIs that overlay the location of the fiber optic temperature probes. Pots (c,d) show the  $B_0$  field drift for all time points for the four ROIs marked. A spatially inhomogeneous field with a global range of approximately 20 Hz is shown. This pattern persisted through time but showed a global field drift[153].

The fiber optic temperature values show a flat baseline temperature change near 0°C during the initial period without heating (Off 1) and a smooth increase in temperature during heating (On). Maximum temperature change varied between 4-9 °C depending on probe location. IDEAL temperature plots show excellent agreement with the fiber optic temperature values, for all locations and phantoms. Table 4.4 shows the variability in IDEAL temperature calculations about 0 °C after subtracting out the “gold standard”

fiber optic temperature values. For the initial nine time points, corresponding to the no heat applied period, the temperature variability was  $-0.11 \pm 0.20$  °C for the three echo reconstruction and  $-0.06 \pm 0.17$  °C for the five echo reconstruction. For the all 25 time points, the temperature variability was  $-0.21 \pm 0.34$  °C for the three echo reconstruction and  $-0.03 \pm 0.29$  °C for the five echo reconstruction. Further breakdown by phantom ratios and grouped values are also shown

IDEAL temperature maps are shown in Figure 4.18 for all three phantoms at 6 time points, two in the initial no heat period (Off 1), three in the heating period (On) and a final one in the second no heat period (Off 2). Temperature maps show a smooth transition of values both spatially and temporally for all phantoms. Despite equal power on all MAPA RF elements the maps show asymmetric heat patterns. However, the same pattern is seen on all phantoms indicating that the asymmetry was likely due to a slight systemic miscalibration of the MAPA RF amplifiers.

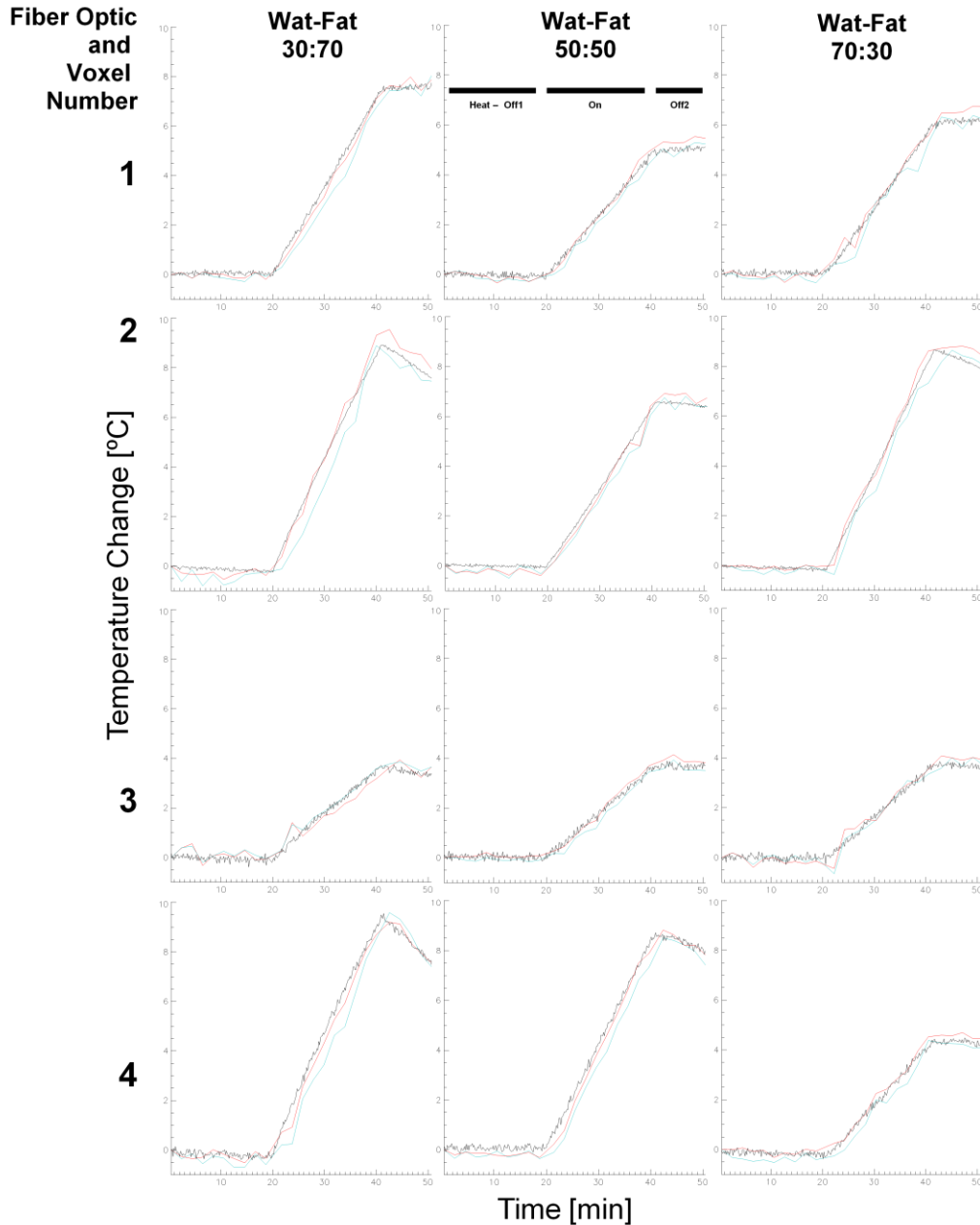


**Figure 4.17:** Plots of IDEAL temperature vs. Fiber Optic Temperature for All Fat-Water Phantoms. Temperature values from the ROIs indicated in Figure 4.15(a) that overlay the four Luxtron fiber optic temperature probe locations. IDEAL-Temp values calculated with three echoes are plotted in blue, values calculated with five echoes are shown in red. Luxtron values are plotted in black. RF heating (On) started at approximately 20 minutes into the experiment and was turned off at 40 minutes (Off2). Rows show the value for a given Luxtron location in the 30:70, 50:50 and 70:30 water-fat ratio phantoms, respectively. Columns show the results for the four Luxtron locations, 1-center, 2-top, 3-bottom right and 4-bottom left, in a given phantom[153].

**Table 4.4:** Temperature variation of IDEAL temperature values minus fiber optic temperature values for three echo and five echo reconstructions. Values are grouped for both reconstructions and broken down for individual and grouped phantoms. Results are further broken down for variations around the first 9 time points when there was no heating applied and then for all time points. Results show that both 3 echo and 5 echo reconstructions provide temperature that is very close to the fiber optic temperature values. However, the 5 echo results are closer to the fiber optic values than the 3 echo results.

<b>Time Points 2-18 minutes (heat OFF)</b>	<b>WAFI-MRI minus Fiber Optic temperature 3 echo reconstruct [°C] (mean ± stdev)</b>	<b>WAFI-MRI minus Fiber Optic temperature 5 echo reconstruct [°C] (mean ± stdev)</b>	<b>WAFI-MRI minus Fiber Optic temperature Both reconstruct [°C] (mean ± stdev)</b>
Water-Fat 30:70	-0.151 ± 0.246	-0.043 ± 0.185	-0.097 ± 0.225
Water-Fat 50:50	-0.100 ± 0.135	-0.079 ± 0.165	-0.090 ± 0.150
Water-Fat 70:30	-0.088 ± 0.202	-0.044 ± 0.175	-0.066 ± 0.189
All Phantoms	-0.113 ± 0.199	-0.055 ± 0.174	-0.084 ± 0.189
<b>Time Points 2-52 minutes (heat OFF-ON-OFF)</b>			
Water-Fat 30:70	-0.337 ± 0.428	-0.014 ± 0.298	-0.175 ± 0.402
Water-Fat 50:50	-0.153 ± 0.266	-0.029 ± 0.269	-0.062 ± 0.282
Water-Fat 70:30	-0.133 ± 0.279	0.071 ± 0.288	-0.031 ± 0.300
All Phantoms	-0.208 ± 0.344	0.029 ± 0.286	-0.090 ± 0.337

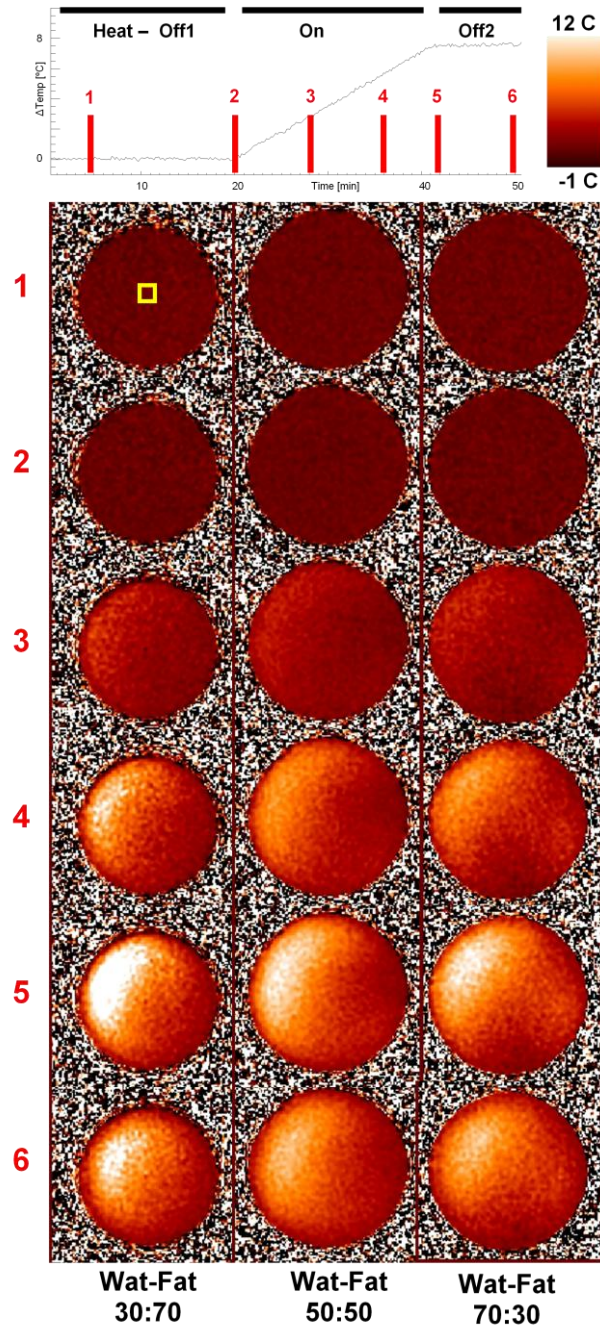


**Figure 4.18:** IDEAL Temperature maps for all water-fat phantoms at 6 time points during data acquisition. The yellow ROI indicated in the Time 1 map shows the location of the fiber optic probe whose values are plotted at the top. RF heating was set equally for all antennas at all time points during the ON period from minute 20 till minute 40 to ensure smooth heating[153]. These diagrams demonstrate the spatial coverage that MR thermometry can provide, identifying the location of hot spots (the white areas in the images).



#### **4.4.5 Experimental Confirmation of Temperature Noise CRLB for Nonlinear Temperature Algorithm**

The measured temperature noise of the 3-echo ESGs plotted against the expected CRLB standard deviations are shown for all three phantoms in Figure 4.19. Similar results for 5-echo and 7-echo ESGs are shown in Figures 4.20 and 4.21, respectively. The experimental measurements using fat-water phantom experiments show excellent agreement to the temperature noise CRLB calculations presented in this chapter. Due to the large number of samples acquired (5000) the error bars of the measurements are too small to be seen on the figures (on the order of  $0.001^{\circ}\text{C}$ ). On average the measured values vary from the temperature noise CRLB by less than 10.96%, 7.64%, and 8.31% for 3-echo, 5-echo, and 7-echo respectively.

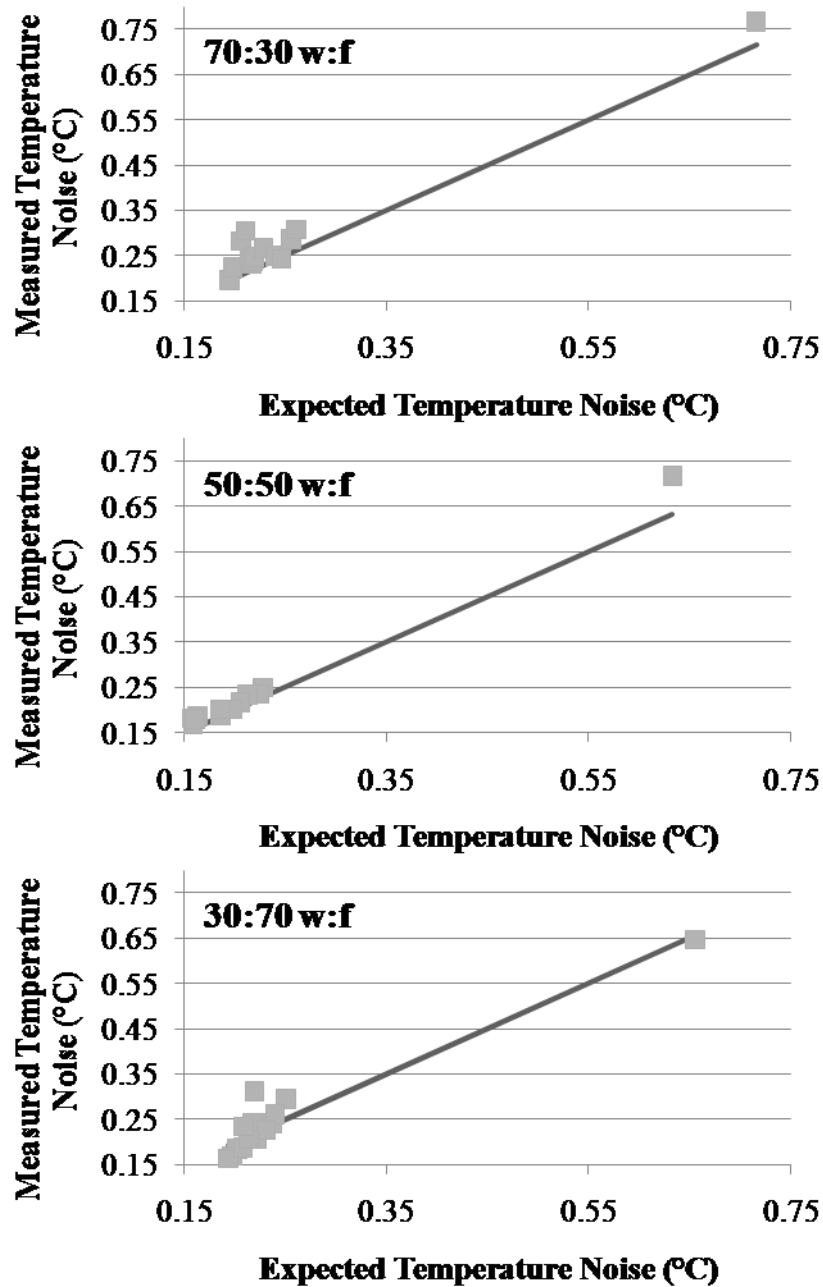


**Figure 4.19:** Phantom results of measured temperature noise and CRLB temperature noise for 3-echo ESGs. The black line is the CRLB temperature noise predictions plotted against themselves, while the gray markers are the measured noise values plotted against the CRLB temperature noise predictions. If the measurements match the CRLB, they should be on the black line, which is seen for most measurements. There is a lack of points at the higher temperature noise levels due to the difficulty of finding non-biased ESGs with high temperature noise.

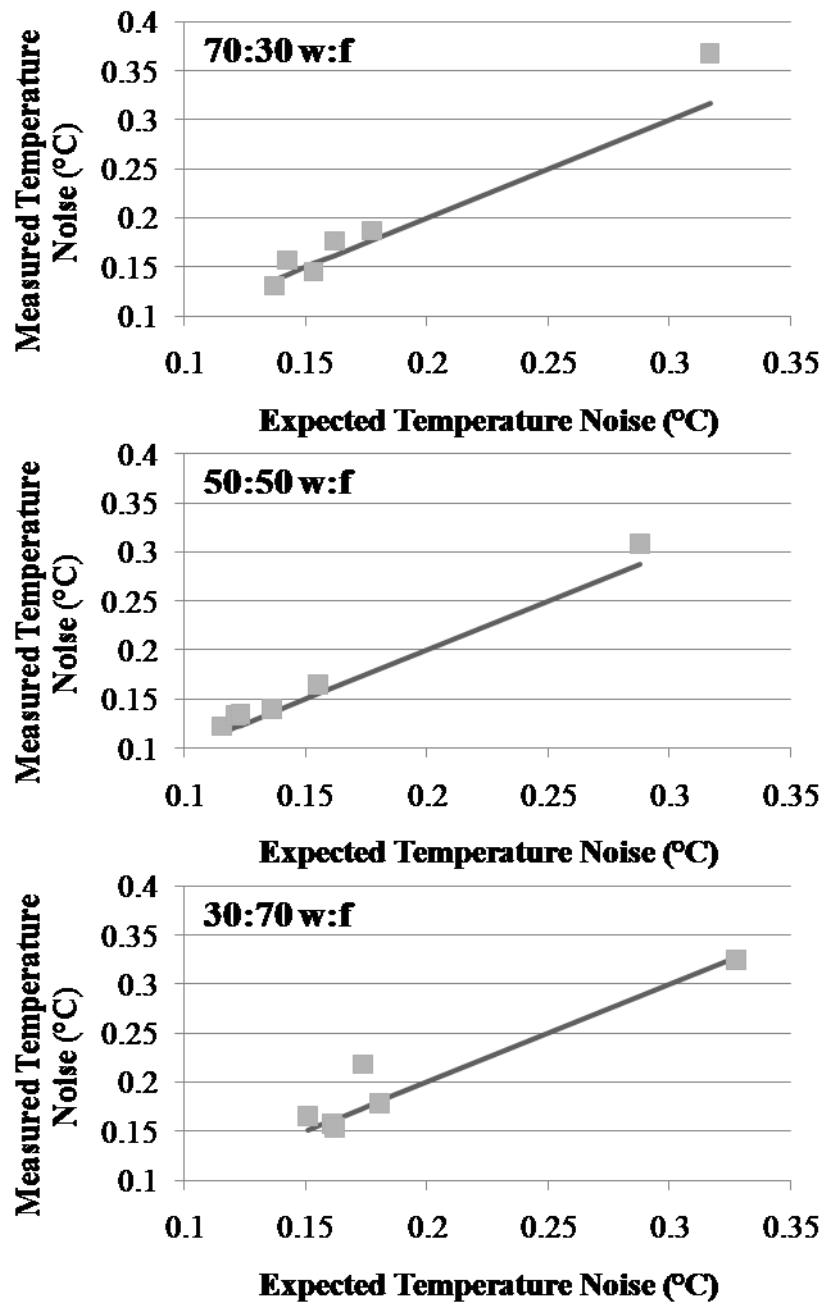


**Figure 4.20:** Phantom results of measured temperature noise and CRLB temperature noise for 5-echo ESGs. The black line is the CRLB temperature noise predictions plotted against themselves, while the gray markers are the measured noise values plotted against the CRLB temperature noise predictions. If the measurements match the CRLB, they should be on the black line, which is seen for most measurements. There is a lack of points at the higher temperature noise levels due to the difficulty of finding non-biased ESGs with high temperature noise.

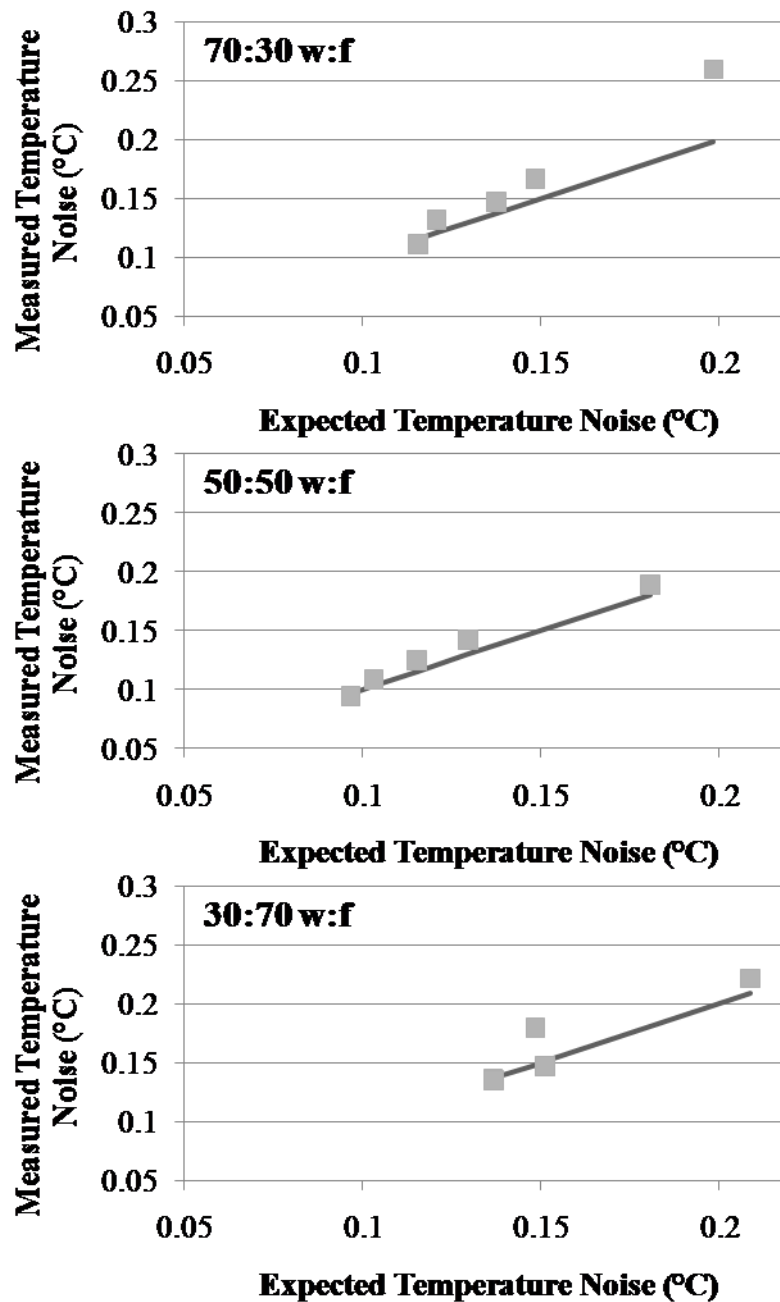


**Figure 4.21:** Phantom results of measured temperature noise and CRLB temperature noise for 7-echo ESGs. The black line is the CRLB temperature noise predictions plotted against themselves, while the gray markers are the measured noise values plotted against the CRLB temperature noise predictions. If the measurements match the CRLB, they should be on the black line, which is seen for most measurements. There is a lack of points at the higher temperature noise levels due to the difficulty of finding non-biased ESGs with high temperature noise.

## **4.5 Discussion**

### **4.5.1 Bias of the IDEAL algorithm**

From Figures 4.3 and 4.4 it can be seen that the temperature and field values measured with the IDEAL algorithm are biased in certain regions, varying from the respective true values of 6°C and 0 Hz. No bias was seen when using the NLM-Temp algorithm. However, there are regions where the IDEAL algorithm is unbiased, but they are very limited in range. Unfortunately, the location of these unbiased regions change with fat-water ratio and fat-water frequency difference, making it unlikely that reliably non-biased temperature measurement can be achieved in-vivo with the IDEAL method.

However, it was seen that there is no bias with either method when no temperature change occurs. Combined with the non-bias of the NLM-Temp algorithm, this evidence suggests that the bias of the IDEAL algorithm stems from the linearity of its signal model and exclusion of a temperature term.

### **4.5.2 Characterizing the Noise Behavior of the Nonlinear Temperature Algorithm**

#### ***Agreement of the Cramer-Rao Lower Bound Temperature Noise Calculation with Simulation***

As seen in Figure 4.5, the temperature noise CRLB shows an excellent match with the results of the NLM-Temp simulations in most situations. In regions of disagreement, the NLM-Temp simulation was determined to be biased because the mean of the predicted temperature change values was found to be significantly different from the correct (input) value of zero. Fortunately, these regions only occurred, for the ranges of parameters

studied, at very low or very high separation angle, where the NLM-Temp algorithm is expected to perform poorly since the phase separation between water and fat does not vary significantly in such regions, i.e., the model does not distinguish between fat and water well in those regions. The power of the temperature noise CRLB method is in the speed of its calculations. A wide range of parameter variations can be calculated in reasonable time. The significance of the initial comparison with Monte Carlo simulations was to help understand which ranges of parameter variations the CRLB method provides accurate values.

### ***Investigation of the Temperature Noise CRLB of Fat-Water Signals for Various Effects***

#### ***Examination of $T2^*$ effects***

The temperature noise CRLB values as a function of rotation for varying  $T2^*_f$  values and a constant  $T2^*_w = 40\text{ms}$  are shown in Figure 4.6. The general trend indicates minimum temperature noise near rotation=4. The minimum of the temperature noise CRLB occurs when the TE values of the ESG are approximately equal to the lowest value of  $T2^*_w$  and  $T2^*_f$ . This mimics behavior seen in normal PRFS thermometry, where imaging at the  $T2^*$  value provides a good compromise between obtaining a large temperature based phase accumulation (to improve temperature change discrimination) and loss of precision due to decreasing SNR at longer echo times [163]. However, trying to adjust the rotation of an ESG to the  $T2^*$  value seen in each hyperthermia heat treatment would not be feasible. Fortunately, low temperature noise CRLB values are consistently seen at rotation = 4 for all values of  $T2^*_f$ , as seen by the arrow in Figure 4.6.

While these values may not be the minimum temperature noise CRLB value for the simulations, they form a practical, good choice based on  $T2^*$  values typically observed in vivo for fat. Thus, choosing a rotation of 4 (approximately 18 ms for typical fat spectra at 1.5T) should provide a consistently low temperature noise CRLB regardless of  $T2^*$  values. A rotation of 3 could also work if shorter TE values are needed, with the penalty of slightly higher CRLB values. Note that with a  $T2^*_f$  less than  $T2^*_w$ , we observed sizeable, increasing fluctuations in the temperature noise CRLB with rotation number, possibly due to the presence of multiple peaks.

#### *Effect of Starting TE and TE spacing*

The temperature noise maps in Figure 4.7 display several interesting features. First, ESGs with very low or very high separation angle typically have a high CRLB, which most likely correlates with the fact that each echo in those ESGs differs little in phase. Also, each temperature noise CRLB map tends to have a several minima, with the number of minima equal to  $N$ . However, even with these minima, there is still a wide range of low temperature noise values typically centered on the separation angle of  $180^\circ$ . However, the width of this region extends when  $N$  increases.

#### *Effect of Fat-Water Frequency Difference*

The effects of different fat-water frequency values on the temperature noise CRLB values are shown in 2D temperature noise CRLB maps in Figure 4.8. In this experiment, the fat-water frequency separation was adjusted from 202-222 Hz to mimic the distribution of frequency differences seen from the spectroscopy of in-vivo breast. The temperature noise CRLB values shift diagonally across the map with changes in the fat-water frequency difference. In fact, from  $\phi_{fw1}=202\text{Hz}$  to  $222\text{Hz}$ , minima became

maxima and vice versa (starting angle=100° and separation angle = 200° is a good example). These result in changes in the temperature noise from 40° to 70°C, or 0.4°C to 0.7°C at SNR=100. These changes between different fat-water frequency values can be particularly problematic since the frequency values can vary between individuals or even between different regions of the body. These results show that variability of the temperature noise is expected when performing MR thermometry in the breast.

#### *Effect of Fat/Water Signal Ratio*

The change of the temperature noise CRLB values with varying f/w ( $A_f/A_w$ ) signal ratio for angle = 150° and separation angle = 150° is shown in Figure 4.9. The most obvious effect seen from permutations in the f/w signal ratio was the similar changes in the temperature noise CRLB values for all starting angle and separation angle pairs. These changes were investigated in detail for the starting angle =150° and separation angle = 150° pair. The temperature noise CRLB is centered around its minimum at  $A_f/A_w = 1$ , or 50:50 water:fat. However, large increases are not seen until the fat percentage gets above 80% or below 20%. This demonstrates that the CRLB is dependent on both the water and fat signals being present in reasonable amounts. Most likely this is due to the fact that the water signal is must be present in sufficient quantity for accurate temperature measurement and the fat signal must be present in sufficient quantity for accurate measurement of the B0 field offset.

#### *Combined Effect of Fat-Water Frequency Difference, Fat/Water Signal Ratio, and Temperature Change*

Because the previously mentioned variables (fat-water frequency difference,  $\Delta T$ , and f/w signal ratio) have significant individual effects on the temperature noise CRLB, a



multifactorial calculation was constructed to allow selection of a starting and separation angle pair that would produce minimal changes in the temperature noise across many situations (Figure 4.10). The standard deviation of the combined CRLB temperature values from varying  $\Delta T$ , f/w signal ratio, and fat-water frequency separation are shown. This map shows that the region with the least combined noise occurs near a starting angle =  $215^\circ$  and a separation angle =  $240^\circ$  with a combined temperature noise equal to  $45.58^\circ\text{C}$  (at SNR = 1). While this result was only calculated for N=3, it could be calculated for any N, likely with results that display more minima (as seen with the five and seven echo results).

*Effect of number of echoes used*

Lastly, the minimum CRLB error with the number of echoes ranging of 3 to 15 echoes is shown in Figure 4.11. As might be expected, the minimum temperature noise CRLB follows a power function on the order of  $x^{0.5}$ , as shown by the fit in Figure 4.11 ( $70.03x^{0.49}$  with  $R^2=1.0$ ). Thus, the improvements in the CRLB tend to closely mimic improvements from SNR due to signal averaging. For instance, the CRLB at N=6 is approximately  $\frac{1}{\sqrt{2}}$  times lower than the CRLB at N=3. The same improvement would be seen if all three of the echoes for N=3 were acquired again and the signals averaged, improving the overall SNR by  $\sqrt{2}$ . Conceptually, the SNR loss due to T2\* decay in the additional TE images are most likely counteracted by additional phase information in the images due to longer TE values. However, these beneficial effects are for extra echoes past rotation=4. Adding TE values that are below rotation=4 (rotations 0,1, and 2) results in much smaller improvements to the temperature noise CRLB than the improvements

seen in Figure 4.11. Thus, it is best to acquire as many of the echoes as possible around  $\text{rotation}=4$  to provide the maximum theoretical benefit to the temperature noise CRLB.

### **4.5.3 Phantom Construction, Spectral and Composition Determination**

As seen in Figures 4.12 and Figures 4.13, the fit values of the water and fat signal in each phantom were a close fit and were close to the measured values. Inaccuracies in fitting the water and fat signal parameters are most likely due to limitations in the model and in the measurement of the fat peaks. First, the model assumes that all the fat peaks had the same  $T2^*_f$ , which is not the case. Also, the model did not include J-coupling, which is present in varying amounts in all the fat peaks. The coupling was ignored since modeling J-coupling can be very complex, especially when peaks are combined together. However, the effect of not including J-coupling was probably a smaller effect since several of the peaks with a large amount of coupling were combined, while the frequency difference between the peaks was much larger than the J-coupling constant of fat (approximately 7 Hz).

Additional limitations in the phantom measurements could have been caused by the estimation of the fat peaks using PRESS. First, the relative ratios of each peak were determined from PRESS spectra taken at  $TE=30\text{ms}$ . However, the measurements used for the fitting ranged from 7.8ms to 33ms. Thus, the ratios calculated from the PRESS spectra probably did not match well at some of the earlier TE times used in the fitting. In addition, the assumption of the same  $T2^*_f$  for all fat peaks may have caused some of the discrepancies. Lastly, as seen in previous studies, the J-coupling present in all of the fat

peaks can create significant error in the areas under each peak (and thus the relative ratios) when using PRESS [164].

#### **4.5.4 Phantom Experiments to Validate IDEAL Method**

Both visual inspection and the temperature variations in Table 4.4 demonstrate that the IDEAL temperature method agrees very well with fiber optic temperature measurements. The mean temperature values for both the initial period without heat (Off 1) and the entire time course were within one standard deviation of 0 °C in all phantoms regardless of the reconstruction method. Mean temperatures for both the 3 echo and 5 echo reconstruction methods remained consistent throughout the data collection, but the standard deviations for the entire heating period (Off1-On-Off2) were almost double those for the initial (Off1) period alone.

As there was no heating in the Off1 period, the assumptions made for the IDEAL temperature method should not interfere with the IDEAL reconstruction. These temperature variations are likely the most representative of the error due to image noise and the water-fat estimation assumptions made by the IDEAL method and thus a limit of the IDEAL temperature method. Work has been done to determine optimized TE values for improving the accuracy of the water-fat IDEAL estimates; however, such optimization was beyond the scope of this work. The TE values chosen for this report were ones empirically shown to produce reasonable results.

A significant benefit of the IDEAL temperature method over the PRFS method is that it provides inherent independence from artifacts due to  $B_0$  field drift. The IDEAL temperature method calculates temperature changes using the phase angle between water

and fat. This allows the apparent phase change in the fat to be self-referenced in the same voxel to the fixed frequency water signal. Because both signals are affected equally by the  $B_0$  drift, and corrected equally by the IDEAL reconstruction estimate of  $B_0$  field changes both spatially and with drift over the 50 minute heating period (approximately  $\pm 40$  Hz spatially and  $\pm 5$  Hz/hr in this experiment), the method was not susceptible to artifacts due to  $B_0$  inhomogeneity as is the PRFS method. However, if significant  $B_0$  field changes occur within the total acquisition time of all echoes for an image, such as can occur in a breast during normal breathing [165], this could result in artifacts in both the water-fat and temperature images. One possible solution will be to use a high speed multi-echo acquisition to acquire data during a single breath-hold[153].

Temperature results in this thesis were similar for all phantoms regardless of water-fat ratio; however, the IDEAL temperature method is expected to fail as the voxel fat-water ratio approaches 0% or 100%. In organs containing compartments with both water and fat or just water, the data collected for IDEAL water-fat image reconstruction could also be used to perform a PRFS temperature change analysis. With the  $B_0$  field estimates created during the IDEAL temperature measurements, the  $B_0$  field drift found in water and fat compartments could also be used to estimate field drift corrections for the water only compartments using a PRFS measure. In both cases, it could be possible for the phase accumulated due to temperature change to exceed  $360^\circ$  and require phase unwrapping to differentiate actual changes. However, TE times can be selected for the IDEAL temperature method that can accommodate the range of temperatures expected to within one phase cycle. Also, by accumulating the change in phase between each

temperature time point, rather than by comparison with an initial baseline value, phase unwrapping is also not needed in a straight PRFS calculation either[153].

A drawback to the data collection method in this report was that the data was acquired using a single-echo sequence on the MR system, although multi-echo implementations of IDEAL have been described [156, 166]. Individual echoes were acquired sequentially and overall acquisition time was approximately 2 minutes for five echoes. This imposed some necessary limitations on spatial and temporal coverage. Two averages were acquired to ensure sufficient SNR to test the method. Based on the SNR of the data and because the IDEAL water-fat images are reconstructed from three images, averaging was not necessary. Also, only one slice was acquired to keep the scanning time short. A multi-echo sequence would have facilitated improved coverage. On higher field scanners (3T for example) where the chemical shift of water-fat is twice that at 1.5T it may be necessary to interleave two 3-echo acquisitions to acquire the TE spacing needed. However, these acquisitions could be reconstructed in a fashion similar to a moving window technique ( $TE_{\text{odd}1}$  with  $TE_{\text{even}1}$ , then  $TE_{\text{even}1}$  with  $TE_{\text{odd}2}$ , then  $TE_{\text{odd}2}$  with  $TE_{\text{even}2}$  etc.) to increase temporal resolution.

The data collection method can have subtle effects on the accuracy of the IDEAL temperature method. Because the “middle” echoes for each image set (the second and third echoes respectively) were acquired approximately 40 seconds apart the five echo image set shows a definite left shift and apparent overestimation of the temperature versus the three echo method. More importantly, higher variability was seen in temperature maps during heating and as the absolute temperature change got higher. This

effect is likely due to the assumption that  $\phi_{\Delta T} \sim \omega_{\Delta T} TE_{N/2}$  based on the time between echoes being small. Also it was assumed that the amount of temperature change during the entire data acquisition would also be small. At two minutes and low heating this may have been a reasonable assumption which broke down as the change in temperature increased. Again, the use of multi-echo data acquisition may alleviate this challenge. Water and fat in the same slice resonate at slightly different frequencies due to the chemical shift of fat protons away from the water frequency. This can cause a chemical shift artifact in the image where the fat appears displaced slightly away from its true anatomical location along the direction of the readout gradient. This effect can be minimized in a given sequence but needs to be accounted for by physically aligning the water and fat images prior to calculating temperatures. The in-plane shift for the data was approximately 1 voxel (2.4 mm) and temperatures changed smoothly and slowly in most locations for this experiment. Thus one can expect variability due to in-plane chemical shift to be small and could be further decreased via higher receive bandwidth or smaller field of view values. There is no solution for through plane shift except to use high bandwidth slice excite pulses and/or thicker slices[153].

Fat signals have the majority of their signal strength in peaks located around 1.2-1.4 ppm, however, a number of lipids (primarily olefinic, -CH=CH- signals) have appreciable signal components whose peaks are at approximately 5.3 PPM [167-170]. This signal contribution, which is very close to the water peak will also demonstrate no temperature dependent chemical shift. In tissues with high fat to water content, this resonance group could significantly mask the phase change of the water signal and lead

to temperature inaccuracies. The multi-peak model of the lipids in the phantoms accounted for this effect. Unpublished results from using only a single peak fat model have shown that temperature values can vary widely from Lumasense values and thus underscore the need for an accurate determination of the fat model. Fortunately, both water-fat imaging and MR spectroscopic techniques exist to allow investigators to determine the number of peaks, their frequency offsets and relative ratios. A possible source of error in the multi-peak fat model determination was the use of a single voxel PRESS spectrum with a TE=30 ms while the water-fat separated images were acquired with TE~20 ms. This could result in relative peak areas changing somewhat due to different  $T_2$  values and to a lesser extent due to J-coupling effects. For future development of water-fat temperature methods it may prove beneficial to determine relative ratios directly from a water-fat pre-calibration imaging set [156].

The IDEAL temperature method's use of longer TE values to amplify the temperature dependent phase angle between water and fat also increases errors in the water and fat signal estimations due to the lack of a  $T_2^*$  decay term in the model. While the phase angle between water and fat is not directly affected by  $T_2^*$  signal attenuation, the accuracy of the water-fat separated image reconstruction can be improved by including this effect [156, 171]. While this extension to the signal model would also increase the complexity of image reconstruction, it would likely improve temperature estimates in regions of severe  $T_2^*$  decay, such as occurs due to tissue iron loading[153].

#### **4.5.5 Experimental Confirmation of Temperature Noise CRLB for Nonlinear Temperature Algorithm**

As seen in Figures 4.17-4.19, the measured temperature noise values closely matched their CRLB counterparts, with the slope of the measured temperature values also matching the slope of the CRLB values. The 50:50 phantom results were closest to the CRLB predictions, while the 70:30 phantom results were less parallel to and farthest from the CRLB predictions. Most of the discrepancies seen in the figures are most likely due to model bias in the  $A_w$ ,  $A_f$ ,  $T2^*_w$ , and  $T2^*_f$  values obtained from fitting using MP-IDEAL. Inaccuracies in fitting the water and fat signal parameters are most likely due to limitations in our model and in our measurement of the fat peaks, the sources of which were discussed previously.

Lastly, while the six measurements of each ESG were taken consecutively, the time needed to acquire all six measurements was approximately six minutes for the 3-echo ESG and approximately 14 minutes for the 7-echo ESG. Since the measured standard deviations were so small and the differences between measured and CRLB even smaller ( $\sim 0.1$ - $0.2$  on average), a small variation in temperature across the phantom could have increased the measured standard deviation and produced errors. However, the fiber-optic temperature probe data indicates that temperature change was not a large source of error in this experiment. The data set with the largest temperature change over the experiment was the 50:50 3-echo experiment, which had an average temperature change of approximately  $0.041^\circ\text{C}$  over the six ESG measurements. The rest of the other experiments had much smaller temperature changes, an example of which is the 30:70 3-echo experiment, which had an average temperature change of approximately  $0.012^\circ\text{C}$



over the six ESG measurements. If these temperature variations were large sources of error, one would expect the 30:70 experiment to have a much larger temperature variation than the 50:50 experiment, since the error of the measurements from the CRLB predictions was much higher in that experiment.

Lastly, while the six measurements of each ESG were taken consecutively, the time needed to acquire all six measurements was approximately six minutes for the 3-echo ESG and approximately 14 minutes for the 7-echo ESG. Since our measured standard deviations were so small and the differences between measured and CRLB even smaller ( $\sim 0.1$ - $0.2$  on average), a small variation in temperature across the phantom could have increased the measured standard deviation and produced errors. However, the fiber-optic temperature probe data indicates that temperature change was not a large source of error in this experiment. The data set with the largest temperature change over the experiment was the 50:50 3-echo experiment, which had an average temperature change of approximately  $0.041^{\circ}\text{C}$  over the six ESG measurements. The rest of the other experiments had much smaller temperature changes, an example of which is the 30:70 3-echo experiment, which had an average temperature change of approximately  $0.012^{\circ}\text{C}$  over the six ESG measurements. If these temperature variations were large sources of error, one would expect the 30:70 experiment to have a much larger temperature variation than the 50:50 experiment, since the error of the measurements from the CRLB predictions was much higher in that experiment.

## 4.6 Conclusion

This chapter has developed and characterized two methods that can be used to measure temperature change in fatty tissue, IDEAL-Temp and NLM-Temp. While it was seen that both methods were effective at measuring temperature, there was significant bias seen in both B0 field offset and temperature measurement with the IDEAL-TEMP method. No significant bias was seen with the NLM-Temp method. The bias was verified by both simulation and experimental results.

Additionally, past temperature noise CRLB formulations for multi-echo fat-water imaging have been extended to include temperature change measurement, T2\* effects, and multiple fat peaks. This CRLB formulation was then verified with Monte Carlo simulations using a nonlinear fitting algorithm that directly fitted for temperature change and B0 offset from multiple echoes. Many variables of the CRLB calculations were altered to assess their effect on the CRLB. These variables included the number of TE values, the choice of TE values, T2\*, fat-water frequency difference, B0 offset, temperature change, and fat/water signal ratio. Finally, three fat-water phantoms of varying fat/water ratios were imaged with ESGs of 3, 5, and 7 echoes. The resulting measured standard deviation of the temperature change was then compared to calculated CRLB values to see if the CRLB values matched experimental values.

As well as can be determined, this is the first time that CRLB values have been experimentally verified in fat-water phantoms. Overall, it was found that the best compromise between low temperature noise and fast scanning is obtained at 1.5T using a rotation of four (with TEs around 18-20ms) and acquiring seven echo times. Also, very

little difference was seen in the temperature noise CRLB when using uniform versus non-uniform sampling of echo times. However, it was found that optimization must be performed to find sampling TEs that are minimally affected by changes in the temperature change, fat-water frequency difference, and fat/water signal ratio. For three echo scans, best noise characteristics are seen for a starting angle of  $215^\circ$  and a separation angle of  $240^\circ$ , resulting in TE values of 20.71, 23.71, and 26.71ms for a fat-water separation of 222 Hz. Using more than three echoes would result in better temperature noise, with seven echoes providing the best noise improvement to imaging time ratio. An examination of the best starting and separation angles for these higher echo numbers would be a good topic for investigation in future work.

## **5 Breath Hold Correction Technique for MR Thermometry of Locally Advanced Breast Cancer**

### **5.1 Introduction**

In the introductory chapter, MR thermometry errors due to breathing were discussed. These errors were also seen in the comfort study results from Chapter 2. One solution to reducing these errors was to image during breath holds. However, it was found that this technique can still cause significant error, due to the varying level of breath holds. In this chapter, a new method for correction of field changes between breath holds is developed and verified using phantoms and human volunteers. This method uses the fatty tissue as magnetic field reference materials in a manner similar to the methods developed in Chapter 2 to fit for field changes between breaths inside the LABC tumor. Heating and non-heating experiments were performed to validate the method using a phantom that mimics a large breast with an LABC tumor inside.

### **5.2 Materials and Methods**

#### **5.2.1. Creation of Multi-Gradient Echo Pulse Sequence**

In order to separate the fat and water to use fat as a reference material, multiple gradient echoes (3 or more) need to be acquired during a single breath hold for use with the IDEAL-TEMP and NLM-TEMP algorithms. This is not possible with the pulse sequences supplied with our commercial (GE Medical Systems) MRI system (although other vendors do have such pulse sequences). In previous experiments, multiple single echo scans were performed to implement the IDEAL method by changing pulse sequence

variables using a scripting language (unique to these GE Medical Systems MRI scanners). However, the scripting language had significant delays between scans, on the range of 5-10 seconds. For a three echo scan, this could result in delays of up to 30 seconds, which already approaches the upper limit for an acceptable breath hold for patients. When adding the time needed to acquire acceptable image data, the scan time can approach a minute or more, far longer than the average breath hold. Thus, a multi-echo sequence was developed to acquire all echoes within one TR period, effectively acquiring all echoes within the scan time needed for a single echo using the previous techniques.

The multi-echo sequence was programmed with the proprietary EPIC programming language (GE Medical Systems). When compiled, EPIC files are used by the scanner control computer to send instructions to the scanner hardware. The fast gradient recalled echo (FGRE) sequence file for software version 14x scanners was obtained from the vendor under a research agreement for modification. The FGRE sequence contains the code for FGRE, SPGR (spoiled gradient recalled echo), and GRE (gradient recalled echo) pulse sequences. In the original code, the sequences could only execute two echoes within one TR period. These two echoes were also bipolar, with the first echo having a positive read gradient and the second echo having a negative read gradient. Using bipolar echoes results in significant difference in image phase unless complex correction techniques are employed[172]. Monopolar echoes have consistent phase, but can create problems when using multiecho techniques to measure the local  $B_0$  field[173]. This is due to the long spacing between TE values that is often necessary to prevent overlapping gradients. The spacing can be reduced to typical values by

increasing the acquisition bandwidth, but with proportionally lower image SNR. With the long echo spacing, the phase difference between fat and water can “wrap” due to the periodic nature of the phase. It was discovered that this can allow the fitting algorithms to converge into false local minima. However, the true minimum can be found using the same techniques as those used for short echo spacing. Thus, a monopolar multiecho pulse sequence was designed.

To do this, the second echo of the FGRE sequence was made monopolar and a third monopolar echo was created. A diagram of the pulse sequence can be found in Figure 5.1. All parameters that are adjustable on the clinical console were made adjustable, such as TE values, to allow for flexibility in image acquisition. Also, the sequence was modified so that images would be reconstructed in the resolution in which they were acquired (normally a 256x256 or 512x512 image is reconstructed using zero-filling). This allowed the creation of smaller images, eg, 128x128 or 64x64 which improves image transfer speed to external computers for temperature change computation and display. Once compiled, the sequence was loaded onto the scanner and tested. The gradient waveforms were checked using the “plotter” command in the GE service window, which plots the waveform commands sent to the gradient hardware. Once the gradient waveforms looked correct, a 50/50 fat/water phantom was imaged using a ESG with TE = [19.9,26.3,32.7], TR=50ms, NEX=4, 128x128, FOV=20cm, slice thickness = 5mm, and flip angle=30°. Images were acquired with single echos and with the new multi-gradient echo sequence. Both data sets were processed with the single-peak IDEAL algorithm and the water, fat, and B0 map images were compared.

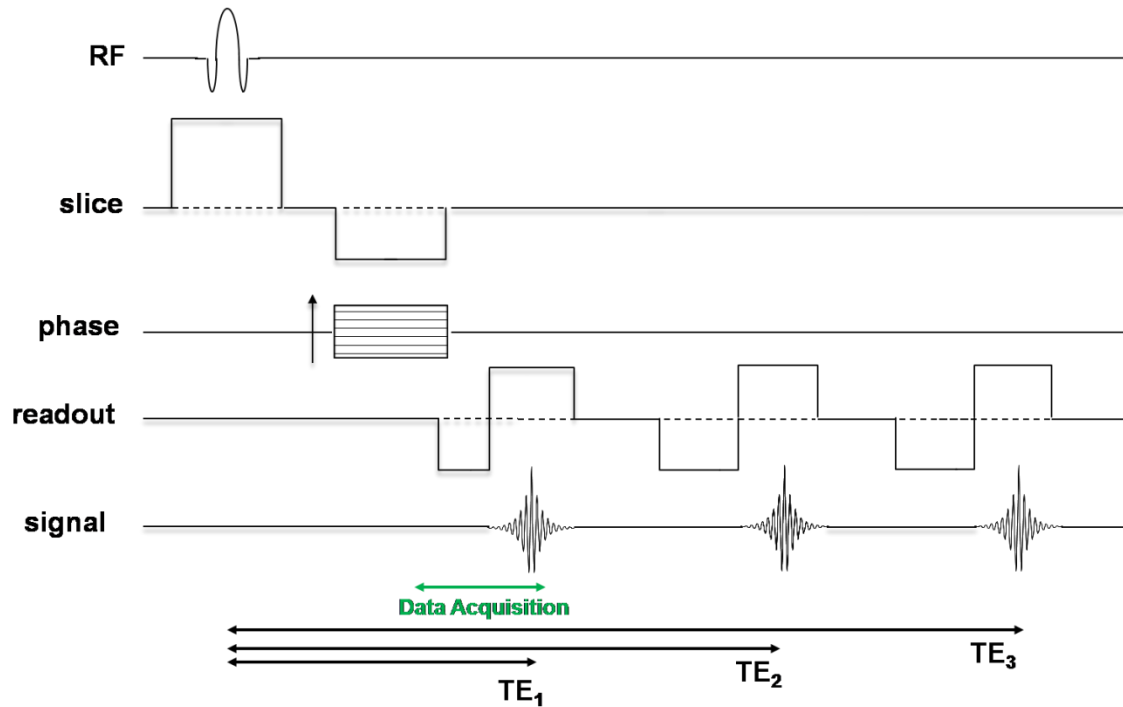


**Figure 5.1:** Pulse sequence diagram for the custom multi-gradient echo pulse sequence

### 5.2.2. Phantom Design and Construction

A phantom mimicking a large breast with LABC was constructed using the recipe used by Wyatt, et al.[142]. The phantom consisted of a 4.25”x5.875” container filled with 85:15 fat-water gelatin. A 2” cylinder was placed through the center of the phantom filled with 100% water gelatin (to mimic a tumor). Two versions of this phantom were made, one with and without catheters, for the heating and non-heating experiments respectively. The phantom with catheters had four #19 catheters inserted through the phantom, three placed around the tumor and the other catheter placed along the center of the tumor. A schematic showing the construction and materials of the phantoms can be found in Figure 5.2. A picture of the phantom is shown in Figure 5.3.

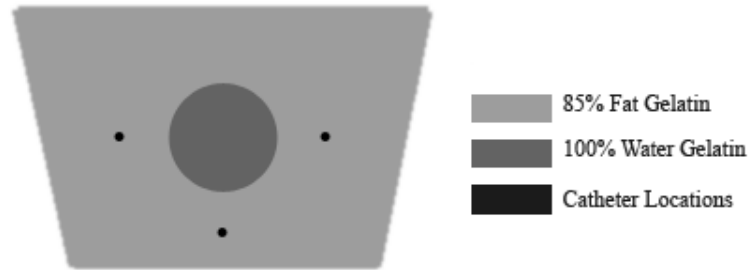


**Figure 5.2:** Construction of phantom mimicking a large breast with LABC



**Figure 5.3:** Picture of the fat-water phantom developed for the breath hold experiments

### **5.2.3. Phantom Non-Heating Experiment with Volunteer Breath Holds**

A phantom non-heating experiment was performed on a version of the breast phantom without catheters. Catheters and thus fiber optic temperature probes were not used due to the inability to insert the probes with the volunteer laying on top of the phantom. The phantom was placed into the breast applicator described in Chapter 2. This support consists of heat-formed plastic with a hole on one side to allow the breast to



extend into the applicator. The water bolus of the applicator was partially filled with 99.8% pure D<sub>2</sub>O (Sigma Aldrich #617385, St. Louis, MO, USA). The phantom was then placed inside the applicator and taped down across the surface of the patient support. This was done to prevent movement of the phantom on the bolus during the experiment. Once secured, the water bolus was filled until it surrounded the phantom. A thin foam pad was then placed over the top of the phantom to prevent it from pushing into the volunteer. The volunteer was then placed on top of the applicator so that their right pectoral area was situated on top of the phantom. Experiments were performed with two male volunteers recruited through an approved IRB protocol. One experiment was performed with volunteer #1, where the volunteer was instructed to breath hold at end inspiration. Two experiments were performed with volunteer #2, one experiment with breath holds on end-inspiration and the other with breath holds on end expiration. During each breath hold, a 5mm thick slice near the center of the phantom was imaged using the custom multi-gradient echo pulse sequence with TE = [15.4, 21.8, 28.2ms], TR = 50ms, Flip Angle = 30°, 128x128, FOV=28cm, BW=15.63 kHz, and NEX=2.0. Imaging was performed with the custom MR coils described in Chapter 2. The scan time and thus breath hold duration was 16 seconds. Volunteer #1 was scanned for 10 breath holds while volunteer #2 was scanned for 20 breath holds with end-inspiration and 12 breath holds with end-expiration. The experiments are labeled and summarized in Table 5.1.

**Table 5.1:** Description of experiment parameters for the non-heating phantom experiments

Experiment #	Volunteer #	Breath Hold Type	# of Breath Holds
1	1	End-Inspiration	10
2	2	End-Inspiration	20
3	2	End-Expiration	12

#### **5.2.4. Phantom Heating Experiment with Simulated Breath Holds**

Two phantom heating experiments were performed with the breast phantom with catheters using simulated breath-holding provided by a setup described further below. Due to the difficulty of shielding a subject from the heating radiations, the simulated breath-holds provided a close simulation of the system behavior breath-holding during heating. The phantom was placed into the same applicator and in the same position as used in the non-heating experiment. Fiber optic temperature probes (Lumasense Technologies, Santa Clara, CA, USA) were then placed into the catheters of the phantom so that the probes were within a 1cm of its center. The phantom was then placed inside the applicator and taped down similar to the non-heating experiment (section 5.2.3). Once secured, the water bolus was filled until it surrounded the phantom. A large bolus made of thin polyvinyl chloride (PVC) fabric filled with air was centered on top of the phantom. On top of the air bolus another PVC bolus was placed that was filled with deionized (DI) water. The air bolus was connected to a pump through a long tygon tube running through the wall of the MR suite. A picture of the experimental setup can be seen in Figure 5.10. The center of the phantom was imaged with one slice using a multi-echo GRE sequence. Scan parameters were TE = [15.4, 21.8, 28.2ms], TR = 50ms, Flip Angle = 30°, 128x128, FOV=28cm, BW=15.63 kHz, NEX=2.0, and slice thickness =

6mm. Imaging was performed with the custom MR coils developed in Chapter 2. Overall scan time was 16 seconds.

Several images were acquired without intervention. For subsequent time points, the air bolus was either deflated or inflated using the pump, which in turn adjusted the height of the water bolus above the phantom. This was done to simulate the field changes that can occur between breath holds. Between each inflation/deflation, an image was acquired for MR thermometry. This setup provides simulation of MR thermometry between breath holds and the problems associated with them. Once several simulated breath holds were performed, power was applied to the heating antennas. Approximately every 10 minutes, the power was turned off (to prevent reduced SNR due to RF noise) and a simulated breath hold was performed. Then, the same slice was imaged with the multi-echo sequence. Afterwards, the heat was turned back on. This was done until significant temperature change was observed in the fiber optic probes ( $\sim 7-8^{\circ}\text{C}$ ).

### **5.2.5. In-Vivo Breast Experiment**

An in-vivo experiment was performed to determine how well the method works in a human female breast with real breath holds. Thus, a healthy female volunteer (age 25) was enrolled under the comfort study protocol discussed in Chapter 2. In this case, the glandular tissue was assumed to be similar to the tumor of a LABC subject. The volunteer was positioned on the breast applicator support system so that their right breast was positioned inside the breast cup, which was filled with DI water to provide good RF coupling with the  $\text{D}_2\text{O}$  filled bolus (to simulate the situation required for heating). First, axial and sagittal T1-weighted images of the entire breast were acquired. Based off of

these images, one 5mm thick slice of the breast with a thick fat layer surrounding a modest amount of glandular tissue was chosen. This slice was then imaged using the custom multi-gradient echo pulse sequence using TE = [15.4, 21.8, 28.2ms], TR = 50ms, Flip Angle = 30°, 128x128, FOV=28cm, BW=15.63 kHz, and NEX=2.0. Imaging was performed with the custom MR coils developed in Chapter 2. Overall scan time was 16 seconds. Breath holds were performed on end expiration for the duration of each scan, for a total of 11 breath holds.

### 5.2.6. Data Analysis

The three echo data from each time point was analyzed with the NLM-Temp algorithm developed in Chapter 4. The water and fat signal model contained three fat peaks such that the MR signal from a voxel containing both water and fat would be:

$$s(k) = \left( A_w e^{\frac{-TE(k)}{T2_w^*}} e^{2\pi i \alpha f \Delta T} + A_f e^{\frac{-TE(k)}{T2_f^*}} (\beta_1 e^{2\pi i TE(k) \phi_{fw1}} + \beta_2 e^{2\pi i TE(k) \phi_{fw2}} + \beta_3 e^{2\pi i TE(k) \phi_{fw3}}) \right) e^{2\pi i TE(k) \psi} + \varepsilon \quad (5.1)$$

where  $A_w$  and  $A_f$  are the TE = 0 (complex valued) amplitudes at the TR of interest for water and fat respectively.  $T2_w^*$  and  $T2_f^*$  are the T2\* values for water and fat respectively,  $\alpha$  is the PRFS thermal coefficient (0.01ppm/°C),  $f$  is the imaging frequency at 1.5T (63.87 MHz),  $\phi_{fw}$  are the frequency differences between the fat peaks and the water peak at a “baseline” temperature,  $T_b$ ,  $\psi$  is the offset from the imaging frequency (magnetic field inhomogeneity affecting both fat and water in a voxel), and  $\varepsilon$  is Gaussian

noise with mean=0 and variance= $\sigma_\epsilon^2$ .  $\beta$  is the relative ratio of the area of each fat peak compared to the area of all fat peaks combined, with all values adding up to 1. The variable “k” is the echo number, for which there are total of three these experiments. The set of echoes described by  $s(k)$  will hereafter be referred to as a Echo Sampling Group (ESG). Finally,  $\Delta T$  is the temperature change from the baseline temperature at which the fat-water frequency differences  $\phi_{fw}$  would be measured. Theoretically, absolute temperature can be measured by fitting for  $\Delta T$  for a known set of  $T_b$  and  $\phi_{fw}$ , giving the measured temperature  $T=T_b+\Delta T$ .

For each data set, the three echoes at each time point were initially analyzed with the MP-IDEAL algorithm. The nine ESGs in table 5.2 were acquired in the center of the breast phantom and fit for  $A_w$ ,  $A_f$ ,  $T2^*_w$ , and  $T2^*_f$  in the 85% fat gelatin. These nine ESGs were also used to determine the relative amplitudes of the three fat peaks, with one peak at -222Hz, one at -175Hz, and the other at 33Hz.

For each time point after the first, the  $B_0$  values at the previous time point were used as the initial guess for the MP-IDEAL algorithm. The calculated  $B_0$  values from MP-IDEAL were then input into the NLM-Temp algorithm as the initial guess for the field value at each pixel. The initial temperature guess for each pixel was assumed to be 0°C. The differences between the field values at consecutive time points were then processed with a least squares fitting algorithm to fit the field differences and extrapolate them into the water-rich regions (100% water gelatin in the phantom experiments and glandular tissue in the in-vivo experiment), henceforth referred to as the Least Squares Single Pixel (LSSP) method.

**Table 5.2:** ESG values used for water and fat fitting with MP-IDEAL. All angle values are in °C.

rotation	starting angle	separation angle
1	150	120
2	165	120
3	125	120
3	190	120
3	310	120
4	120	120
4	190	120
5	135	120
6	135	120

The LSSP method uses the results of the MP-IDEAL method to determine the pixels in the area of interest (the phantom or the in-vivo breast/chest wall) that have a fat/water signal ratio that is greater than 50%. This is to ensure that all of the pixels used will have accurate  $B_0$  field measurement. Every pixel chosen through thresholding was then placed into a long 1D vector which then used as input for a fifth order least squares fitting algorithm which fit the values to the function

$$\begin{aligned}
 B_0(x, y) = & a_0 + a_1x + a_2y + a_3x^2 + a_4y^2 + a_5x^3 + a_6y^3 + a_7x^4 + a_8y^4 + a_9x^5 + a_{10}y^5 \\
 & + a_{11}xy + a_{12}x^2y + a_{13}xy^2 + a_{14}x^3y + a_{15}xy^3 + a_{16}x^4y + a_{17}xy^4 \\
 & + a_{18}x^2y^2 + a_{19}x^3y^2 + a_{20}x^2y^3 \quad (5.2)
 \end{aligned}$$

A 3<sup>rd</sup> order version of equation 2 was used for the in-vivo breast experiment since it was most stable. Once the values of  $\alpha$  were solved for, the values were then input into equation 2 to solve for the  $B_0$  field change for all pixels of the image.

The LSSP algorithm results in field change maps that predict the amount of field change that occurred between time points in the water-rich portions of the image. These

field maps are then converted to phase change maps at the first echo by multiplying the field map by the 1<sup>st</sup> TE value (15.4ms in all experiments). The predicted phase change maps are then subtracted from the phase change maps calculated from the changes in phase between time points at the 1<sup>st</sup> echo time. This results in corrected phase change maps that were converted to temperature maps using equation

$$\Delta T = \frac{\Delta\phi}{(f * TE * \alpha * 360)} \quad (5.3)$$

where  $f = 63.85\text{MHz}$ ,  $TE = 15.4\text{ms}$ , and  $\alpha = -0.01$ . Similar results can be calculated using the 2<sup>nd</sup> echo or the 3<sup>rd</sup> echo.

Additional calculations were performed to compare the new method of correction using field maps with the referenceless thermometry method discussed in the section 1.3.5 and the introduction to this chapter. The referenceless thermometry method was implemented by using the image phase change maps instead of field change maps as input into the LSSP method. The phase changes at the first echo time were used to avoid phase wrap problems.

## **5.3 Results**

### **5.3.1 Multi-Gradient Echo Pulse Sequence**

A comparison of single peak IDEAL fitting for the single echo and multi-echo sequences are shown in Figure 5.4.

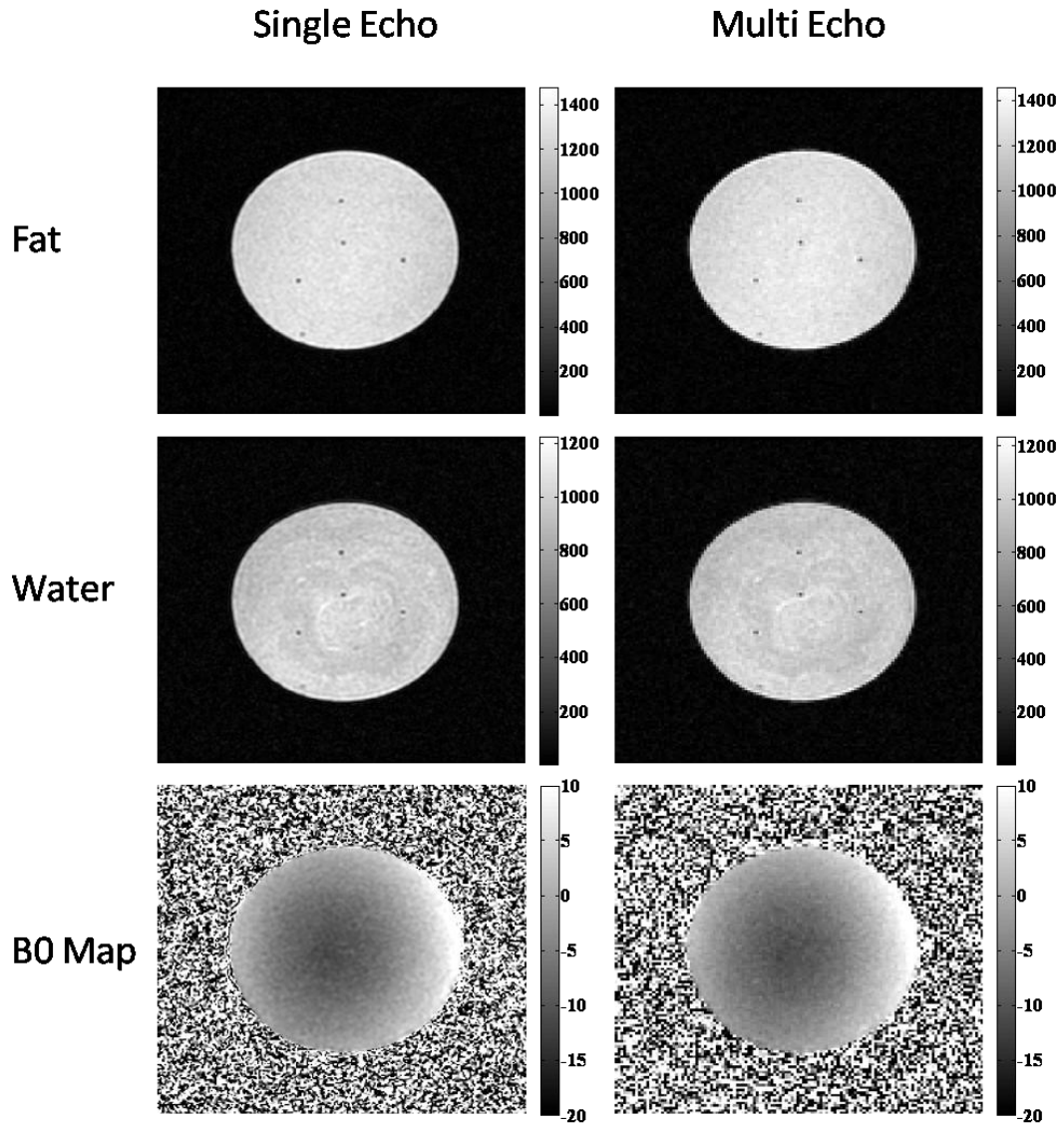


**Figure 5.4:** Comparison of IDEAL results for the single echo and multi echo sequences. The results are identical for single and multi echo sequences.

### 5.3.1. Phantom Non-Heating Experiment with Volunteer Breath Holds

The values from the MP-IDEAL fit and the input into the NLM-Temp algorithm were  $A_w = 552$ ,  $A_f = 6000$ ,  $T2^*_w = 46.2\text{ms}$ , and  $T2^*_f = 23.8\text{ms}$ . The relative amplitudes of the fat peaks were 0.773 for the -222 Hz peak, 0.149 for the -175Hz peak, and 0.078 for the 33 Hz peak.



A picture of the phantom secured inside the applicator is shown in Figure 5.5. A MR image of the phantom inside the applicator with the volunteer on top is shown in Figure 5.6. In Figure 5.7, a field change map between breath holds is shown overlaid on the magnitude image in Figure 5.6. Due to the left/right orientation of the phase encoding, significant motion artifacts from the heart prevent accurate imaging of the volunteer's chest. Figure 5.8(a) shows the field measured with the nonlinear fitting algorithm for the first volunteer while 5.8(b) shows the fitted field using the LSSP method with the field in (a) as input.

A plot showing the uncorrected PRFS temperature in the water gelatin and the temperature after correction with measured field changes fit using the LSSP method is shown in Figure 5.9 for experiment #1. Similar results are shown for the experiment #2 and #3 in Figures 5.10 and 5.11 respectively. The experiment numbers can be found in Table 5.1. The mean and standard deviation of the uncorrected and corrected data sets for each experiment are shown in Table 5.3. Corrected data sets shown include the correction with field changes and correction with image phase changes (the referenceless method).



**Figure 5.5:** Picture of phantom secured inside the breast applicator. Tape was used to secure the phantom inside the applicator and prevent its movement with the volunteer's breathing.

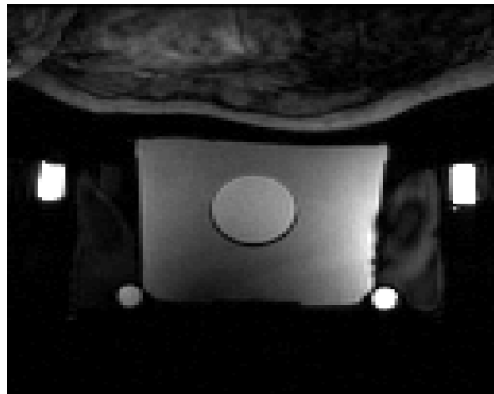


**Figure 5.6:** A MR image of the phantom inside the applicator with the volunteer on top

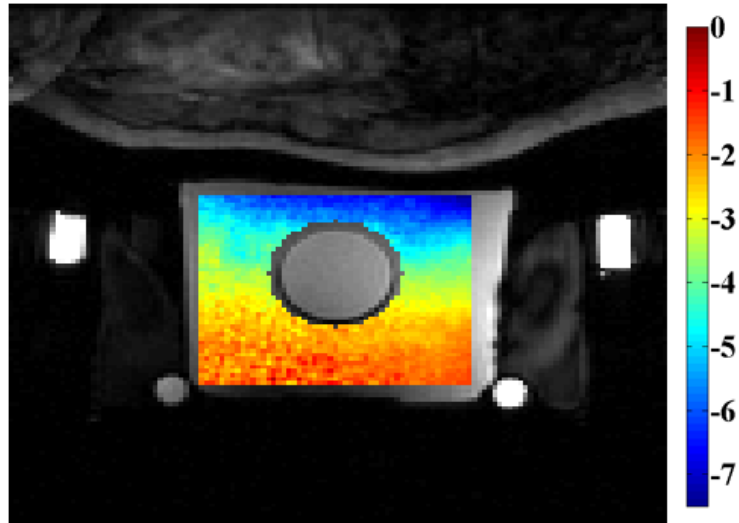


**Figure 5.7:** Overlay of a field change map on the magnitude image of the phantom in the applicator. The colorbar is in units of Hz. Notice the complex shape of the field changes and the severity of the changes near the top of the phantom.

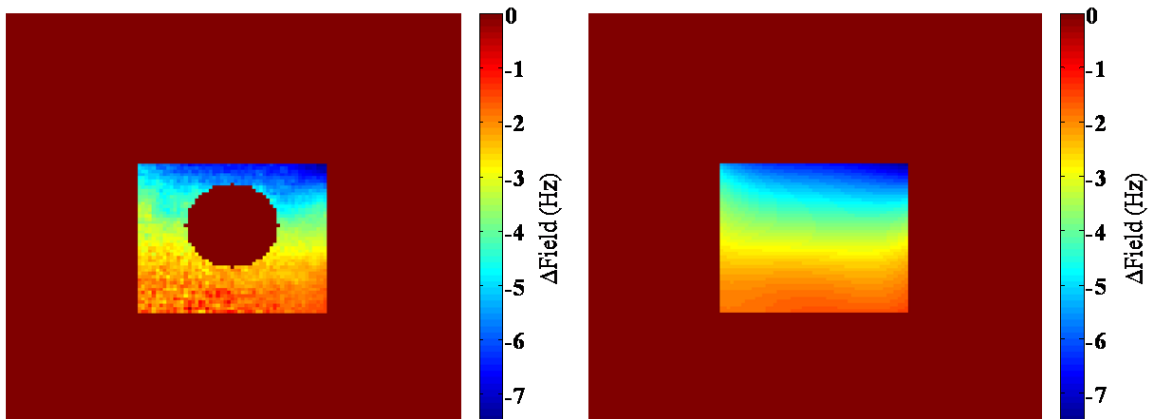


**Figure 5.8:** (a) Field measured with the nonlinear fitting algorithm for the first non-heating phantom experiment. Field measurements in the water-rich “tumor” region are ignored due to their unreliability during temperature changes. (b) Field fit using the LSSP algorithm with the field in (a) as input. Notice how the field is accurately extrapolated into the “tumor” region that previously lacked accurate field measurement.

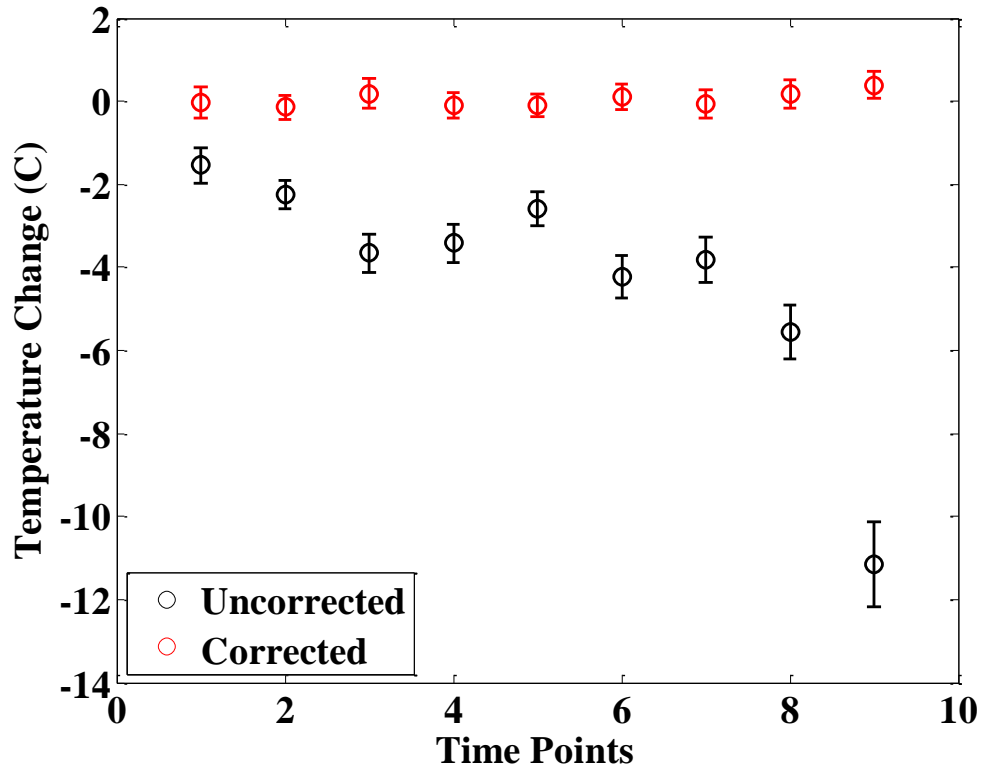


**Figure 5.9:** Uncorrected and corrected temperature change measurements in the water gelatin for experiment #1 of the non-heating phantom experiments. The values are referenced to the temperature image at the first breath hold. Since no heating was applied, the temperature change should be 0°C across all breath holds. This is seen in the corrected measurements, while the uncorrected measurements have large temperature error. Also, note the smaller error bars for the corrected measurements. This suggests that the correction method corrects for the spatial inhomogeneities induced by the breath hold field changes.

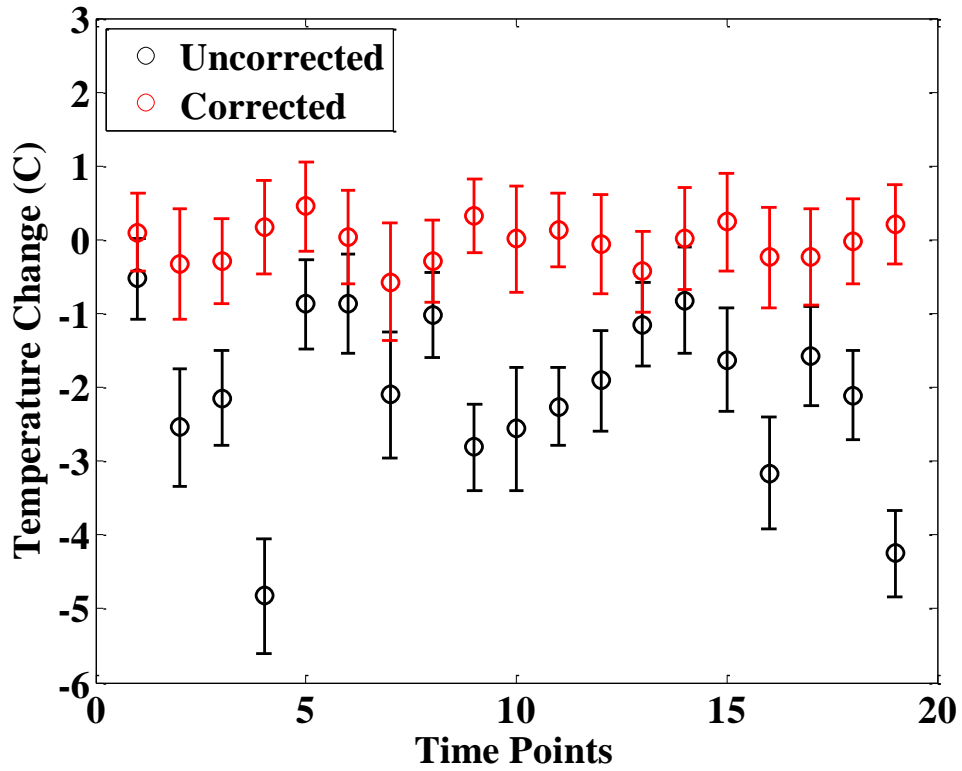


**Figure 5.10:** Uncorrected and corrected temperature change measurements in the water gelatin for experiment #2 of the non-heating phantom experiments. The values are referenced to the temperature image at the first breath hold. Since no heating was applied, the temperature change should be 0°C across all breath holds. This is seen in the corrected measurements, while the uncorrected measurements have large temperature error.

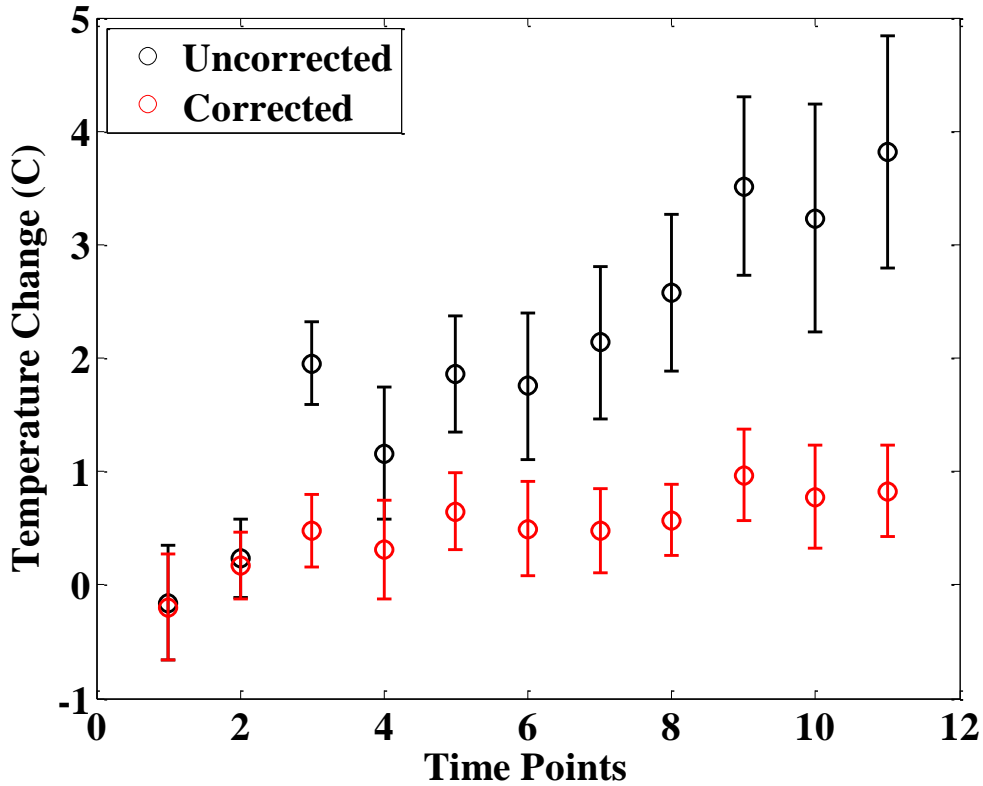


**Figure 5.11:** Uncorrected and corrected temperature change measurements in the water gelatin for experiment #3 of the non-heating phantom experiments. The values are referenced to the temperature image at the first breath hold. Since no heating was applied, the temperature change should be 0°C across all breath holds. This is seen in the corrected measurements, while the uncorrected measurements have large temperature error. Also, note the smaller error bars for the corrected measurements. This suggests that the correction method corrects for the spatial inhomogeneities induced by the breath hold field changes.

**Table 5.3:** Mean and standard deviation of all the time points in each experiment for both the uncorrected and corrected data sets. As seen here, the corrected method has not only corrected the mean, but also has significantly reduced the standard deviation (noise) of the measurement. All measurements are in °C.

Exp #	Uncorrected		Corrected with Field Maps		Corrected with Image Phase	
	Mean	Standard Deviation	Mean	Standard Deviation	Mean	Standard Deviation
1	-4.245	2.844	0.049	0.179	0.036	0.158
2	-2.061	1.150	-0.041	0.273	0.604	0.339
3	2.007	1.266	0.504	0.324	0.763	0.377

### 5.3.2. Phantom Heating Experiment with Simulated Breath Holds

Pictures of the phantom secured inside the applicator, the water bolus, and the air bolus are shown in Figure 5.12. A MR image of the phantom inside the applicator with the boluses on top is shown in Figure 5.13. Figure 5.14(a) shows the field measured with the nonlinear fitting algorithm for the first volunteer while 5.14(b) shows the fitted field using the LSSP method with the field in (a) as input.

A plot showing the fiber optic probe temperature, the uncorrected PRFS temperature in the water gelatin, and the temperature after correction with measured field changes fit using the LSSP method is shown in Figures 5.15 and 5.16 for the two experiments performed. The average root mean square deviation (RMSD) from the fiber optic temperature profile is shown in Table 5.4 for the uncorrected and corrected data sets. Corrected data sets shown include the correction with field changes and correction with image phase changes (the referenceless method).

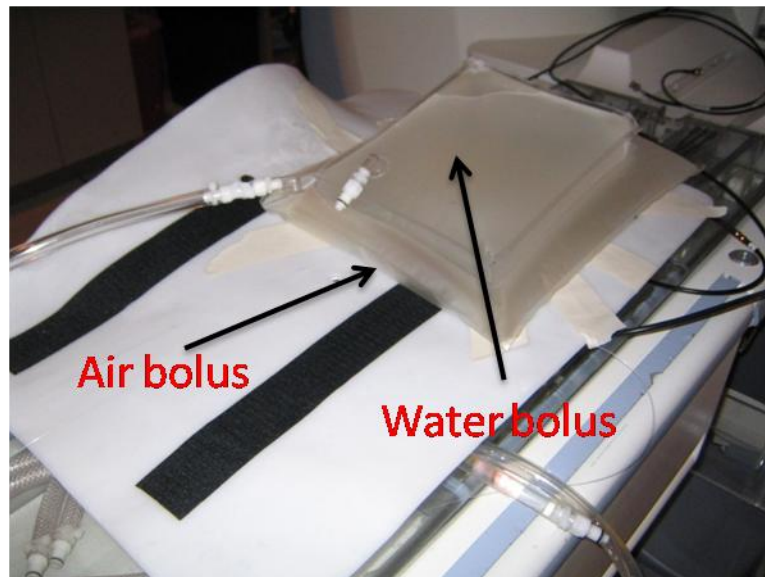


**Figure 5.12:** Experimental setup of the phantom in the applicator, the air bolus, and the water bolus. Tape was used to secure the phantom inside the applicator and prevent its movement during movement of the water bolus

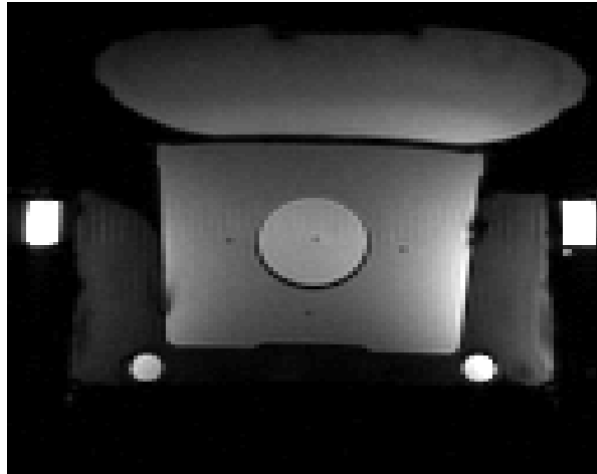


**Figure 5.13:** Magnitude image of the phantom in the applicator and the boluses on top

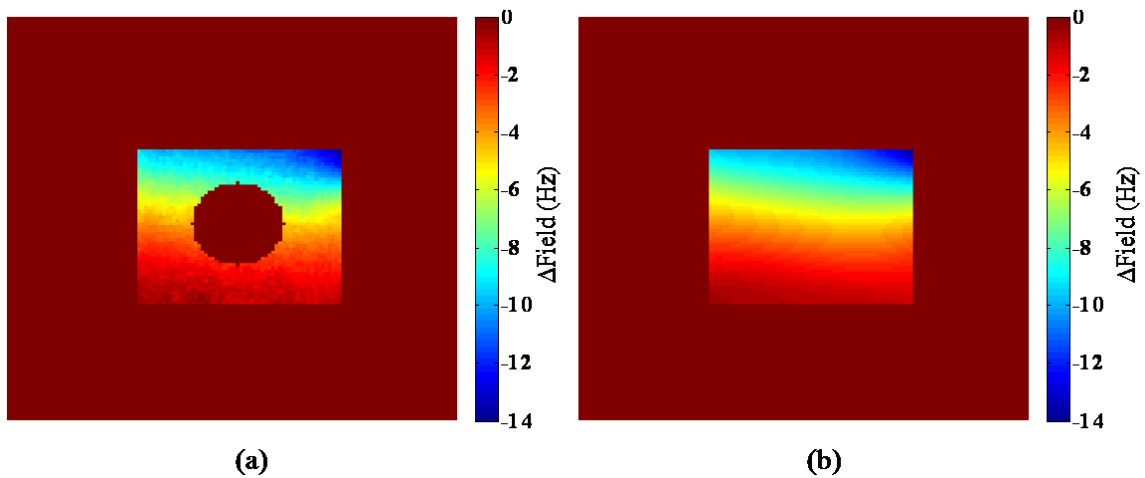


**Figure 5.14:** (a) Field measured with the nonlinear fitting algorithm for the first heating experiment. Field measurements in the water-rich “tumor” region are ignored due to their unreliability during temperature change (b) Field fit using the LSSP algorithm with the field in (a) as input. Notice how the field is accurately extrapolated into the “tumor” region that previously lacked accurate field measurement.



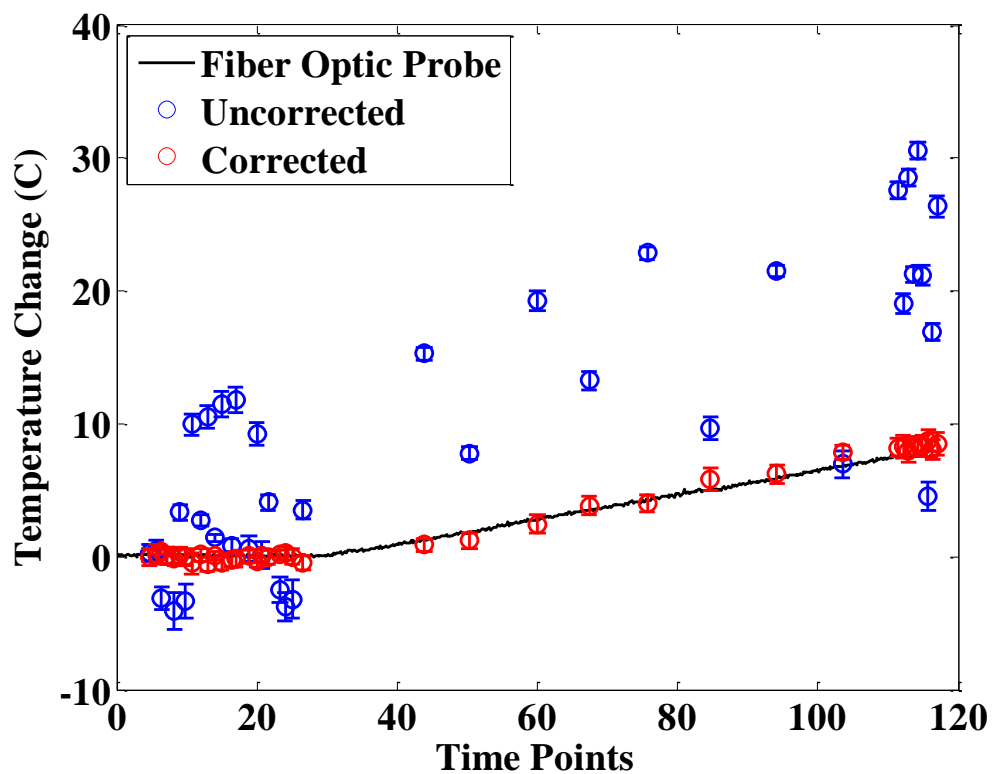


**Figure 5.15:** Uncorrected and corrected temperature change measurements in the water gelatin for the first phantom heating experiment. These are shown plotted against the temperature change measurements from the fiber optic temperature probes. Notice how the corrected temperature closely tracks the fiber optic temperature, while the uncorrected temperature has large errors. These errors are of greater magnitude than would most likely be seen in vivo, but can function as a worst case scenario.

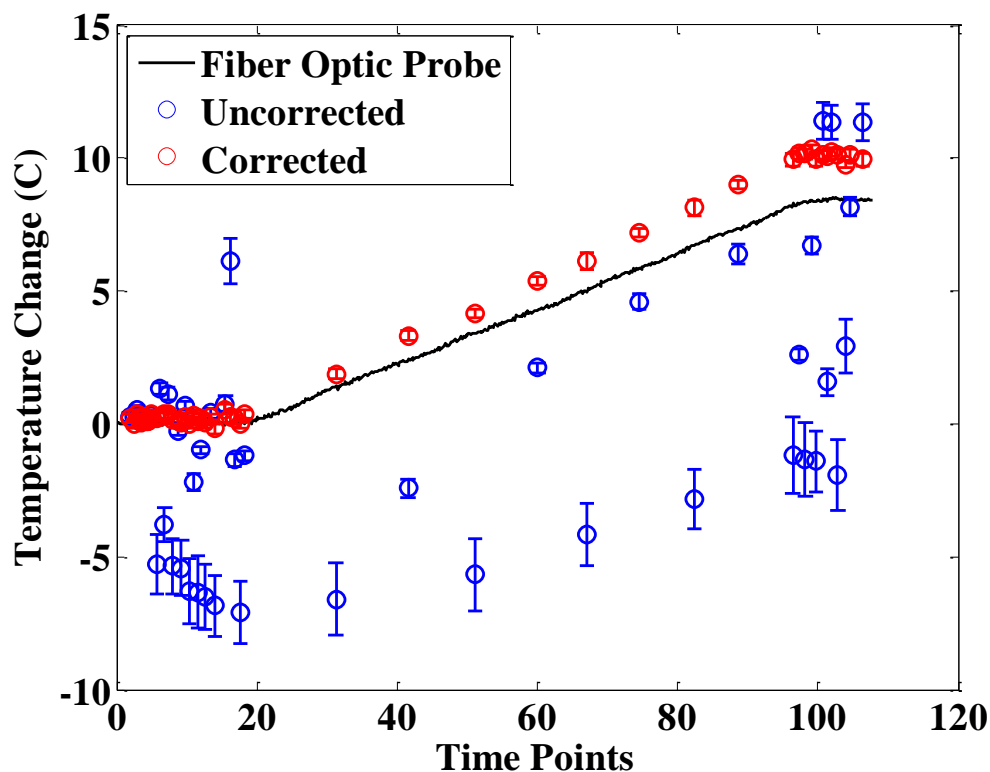


**Figure 5.16:** Uncorrected and corrected temperature in the water gelatin for the second phantom heating experiment. These are shown plotted against the temperature change measurements from the fiber optic temperature probes. Notice how the corrected temperature closely tracks the fiber optic temperature, while the uncorrected temperature has large errors. These errors are of greater magnitude than would most likely be seen in vivo, but can function as a worst case scenario. Also, note that the error bars are much smaller for the corrected data than for the uncorrected data. However, the error bars for the uncorrected data can be very small, which was found to occur during points in which the spatial inhomogeneity of the field changes in the tumor was small.

**Table 5.4:** Average Root Mean Squared (RMS) deviation across all time points of the two heating experiments. Notice the large decrease in the deviation in the corrected data compared to the uncorrected data.

Exp #	Average RMS Deviation (°C)		
	Uncorrected	Corrected with Field Maps	Corrected with Image Phase
1	10.394	0.539	1.172
2	5.047	0.982	1.797

### 5.3.3. In-Vivo Breast Experiment

A MR image of the volunteer's right breast inside the applicator is shown in Figure 5.17. Images of the MP-IDEAL separated water and fat components of the image are shown in Figure 5.18. An image of the field change map for the first time point is shown in Figure 5.19. The uncorrected and corrected temperature maps after all time points are shown in Figure 5.20. Finally, plots of the temperature over time are shown for two regions of the glandular tissue in Figures 5.21 and 5.22. The mean and standard deviation of the uncorrected and corrected data sets for the experiment are shown in Table 5.5.

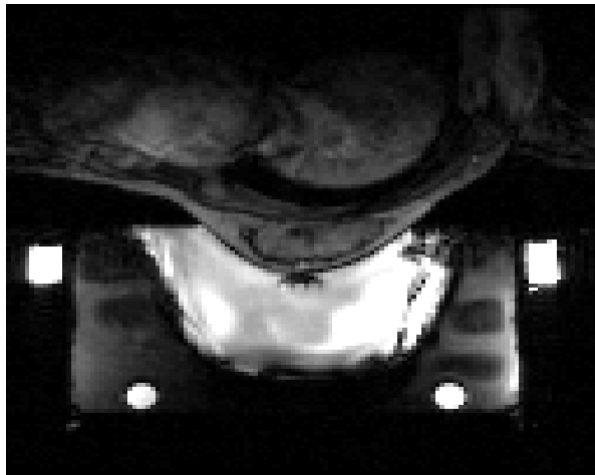


**Figure 5.17:** Magnitude image of the volunteer's right breast in the applicator

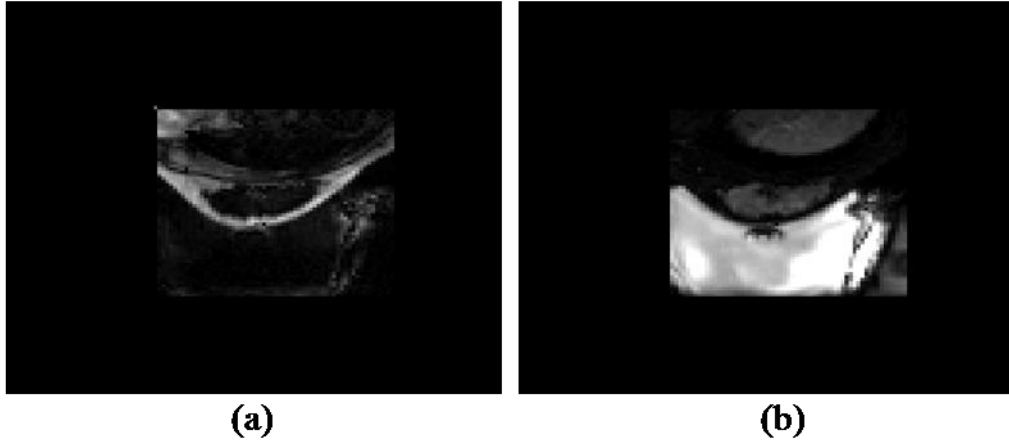


**Figure 5.18:** (a) Fat and (b) water separated images using MP-IDEAL



**Figure 5.19:** Field change map used in the LSSP method

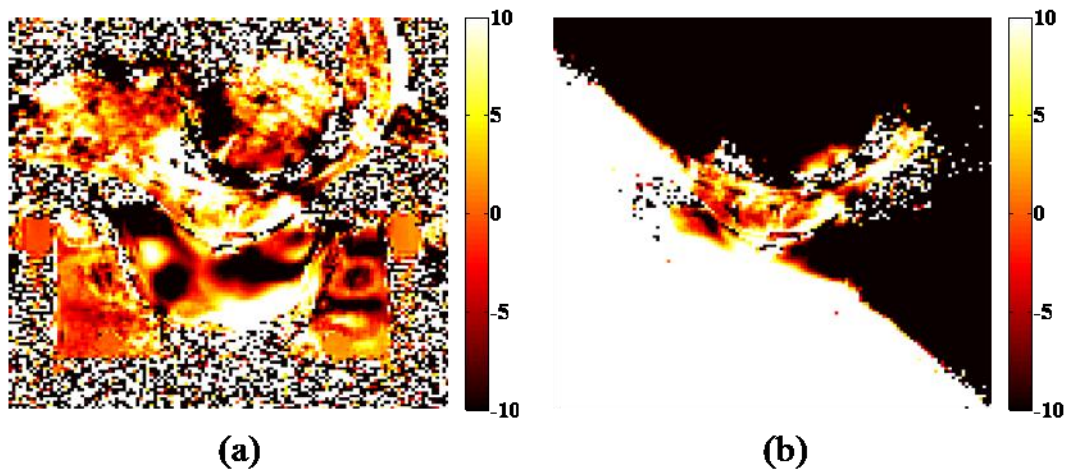
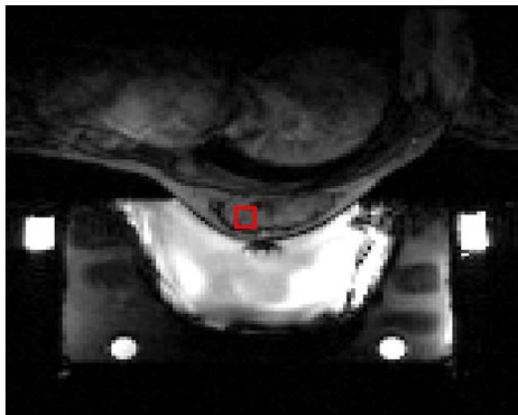
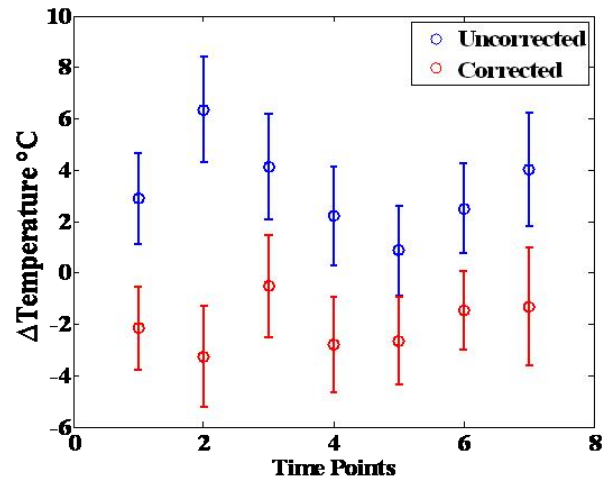


**Figure 5.20:** (a) Uncorrected and (b) corrected temperature maps at the last breath hold. Notice the reduced error across the entire breast.

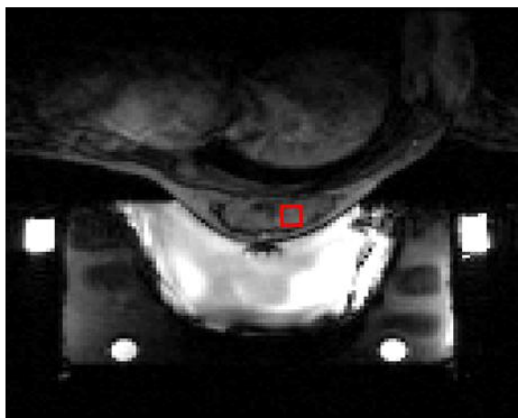


(a)

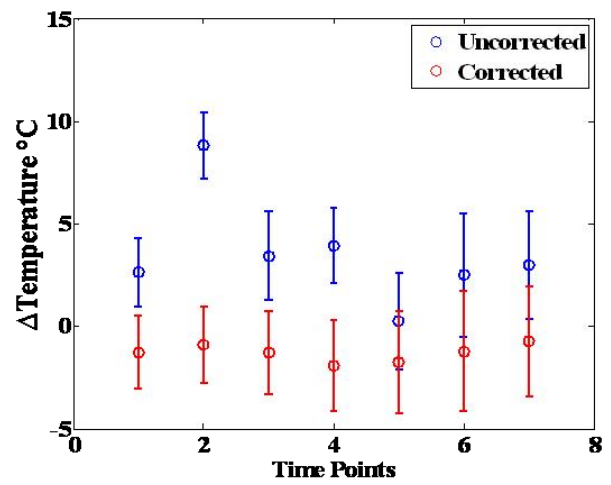


(b)

**Figure 5.21:** (a) ROI of pixels used in the left side of the glandular tissue used for sampling (b) plot of the uncorrected and corrected temperature change across all time points. Temperature change was calculated in reference to the temperature at the first breath hold.



(a)



(b)

**Figure 5.22:** (a) ROI of pixels used in the right side of the glandular tissue used for sampling (b) plot of the uncorrected and corrected temperature across all time points. Temperature change was calculated in reference to the temperature at the first breath hold.

**Table 5.5:** Mean and standard deviation of all time points of the uncorrected and corrected data sets for the in vivo breast experiment. Notice the reduction in the mean and in particular the standard deviation for the corrected data compared to the uncorrected data. All measurements are in °C.

	Uncorrected		Corrected	
	Mean	Standard Deviation	Mean	Standard Deviation
Left	3.29	1.75	-2.02	0.97
Right	3.52	2.62	-1.29	0.43

## 5.4 Discussion

The results of the non-heating phantom experiments (shown in Figures 5.9-5.11) show good correction of the field changes induced by real human breathing, reducing errors on the order of 5-10°C to less than 1°C. Table 5.3 shows that both correction methods result in a mean temperature much closer to 0°C, the value expected since no heat was applied during the experiments. Just as important, the standard deviation was largely reduced by correction. Sources of error could include heating or cooling of the phantom during the experiment. Due to the lack of fiber optic probes, this cannot be determined. However, the length of the experiments was never longer than 20 minutes, which is very little time for temperature changes to occur in the middle of the phantom where the correction was evaluated.

The results of the heating phantom experiments show that correction with field changes is effective even when temperature changes are present. The field changes induced by the simulated breath holds are spatially similar to the field changes observed with volunteer breath holds, as seen when comparing figures 5.8 and 5.14. However, particularly in the first heating experiment, the magnitude of the field changes was larger

than those seen in with volunteer breath holds. Figures 5.15 and 5.16 demonstrate that correction with field changes results in temperature values that are much closer to the fiber optic temperature values than without correction. Results in Table 5.4 demonstrate the temperature deviation from the fiber optic temperature was largely reduced by both correction methods. However, the correction with field changes performed much better than the correction with image phase (referenceless method), with almost half the error. This was expected, since the temperature increase induces phase changes in the water signal in the fat gelatin, producing error in the fit phase changes. Thus, these results demonstrate that the field fitting method provides more accurate correction under the presence of temperature changes. Finally, small errors between the corrected temperature and the fiber optic temperature can be seen near the end of the experiments. This could be due to the fiber optic probe being slightly out of the slice used for MR temperature measurement.

The in-vivo breast experiment shows that good correction can be achieved in the glandular tissue of the breast, as seen in Figures 5.21 and 5.22. The results in Table 5.5 show that while the mean was not corrected close to 0°C in some cases (as would be expected since no heat was applied), the standard deviation was largely reduced compared to the uncorrected temperature values. Good correction could not be evaluated in the middle of the glandular tissue due the presence of a strand of fatty tissue. Also, problems with the correction were present around the edges of the glandular tissue region. This is most likely due to the small amount of fat present. In particular, there was very little breast fat near the top of the breast. Most of the fat used near the top of the breast was chest wall fat, not breast fat. The SNR and field fitting in the chest wall

were worse than in the breast, which may have contributed some error. Also, the field fitting with the region growing method resulted in a small amount of pixels with inaccurate field values, which made for inaccurate field change values. A small amount of these pixels can be seen in Figure 9. Most of these were eliminated by removing pixels with changes of more than 25 Hz, which is more change than would be expected and at the boundary of field wrapping. However, with the large amount of pixels used in the fit, these would have a very small effect on the fit. Lastly, very slight movements of the breast were seen two of the time points, which could have contributed to some of the error. However, correction in the majority of the glandular tissue resulted in reducing errors of 8°C to less than 2°C. This correction is particularly good considering the non-ideal nature of the breast. In a typical LABC patient, there would be much more fatty tissue in the breast to use for fitting and most likely a smaller water rich region. However, the results shown here show great promise for this method in vivo.

## **5.5 Conclusion**

The work presented in this chapter has shown the feasibility and accuracy of using field changes measured using multi-echo fitting techniques in fatty tissue to correct for field changes in water-rich regions of the breast caused by breath holds. This technique has been validated in a number of situations, including non-heating phantom experiments with human breath holds, phantom experiments with heating and simulated breath holds, and in a healthy female breast. In all cases the correction method has been shown to drastically reduce temperature error in water-rich regions. The method has also been shown to be an improvement over similar methods that use image phase changes



instead of field changes, particular when temperature changes are induced. While the healthy breast results show good correction in the glandular regions, future work is needed to assess the accuracy of the technique in breasts with LABC.

## 6 Future Work

The previous chapters discussed the many tools developed in this thesis for the hyperthermia treatment of LABC and the monitoring of that treatment with MR thermometry. However, many of these systems and techniques have only been demonstrated in phantoms or healthy human subjects. While these experiments were successful at providing the means for MR thermometry, more experiments are needed to fully translate them into the clinic.

In chapter 2, a system was developed for providing hyperthermia treatment within the MR bore. While a comfort study showed that it was comfortable to healthy subjects for the typical duration of a hyperthermia treatment, there are more studies that can be done to test and evaluate its effectiveness. First, a comfort study needs to be performed with patients with untreated LABC. This will not only provide crucial comfort data but also MR data that can provide average fat/water ratio values that can be expected in that population. Currently, the comfort study protocol has been amended to allow for subjects with LABC. Unfortunately, no subjects with LABC have been recruited. Also, more heating experiments with the breast applicator and phantoms need to be performed to determine its heating performance and improve it if necessary.

In chapter 3, a technique for correcting magnetic system drifts using oil references was developed and characterized. While this was characterized in vivo and in phantoms, it was not characterized during heating. Performing heating experiments in vivo and with phantoms with oil references and water references could show the improvement that the non-temperature sensitivity of oil references provides over water references. Currently a

protocol for heating leg sarcomas in canines is open, which could provide a source of experimental confirmation of more oil reference configurations.

In chapter 4, techniques for measuring temperature in fatty tissue were developed and characterized. While it was found that these methods were effective in phantoms, no experiments were performed in vivo. Performing heating experiments in vivo would be ideal in helping translate these methods into the clinic. Currently, an IRB protocol for performing hyperthermia treatment of LABC has been submitted. However, before it can be started, an investigation device exemption (IDE) must be approved for the breast applicator. The process of obtaining an IDE has begun. Hopefully hyperthermia treatment of LABC can begin by the end of 2010 and MR thermometry of fatty tissue can be obtained during the treatment.

In chapter 5, a technique of correcting for the breath hold artifacts in the MR thermometry of hyperthermia treatment of LABC was developed. This technique was effective in phantoms and in a healthy volunteer. However, the healthy volunteer was a non-ideal case and it would be preferred to perform experiments in subjects with LABC. If LABC subjects are recruited under the comfort study in Chapter 2, then the breath hold correction technique will be tested on these subjects. Then, if hyperthermia treatment of LABC patients occurs, the techniques will also be used and evaluated in the tumor.

These results can not only be used in the breast, but also in the extremities or the abdomen. Results in Chapter 2 have shown the effectiveness of the oil reference correction method in the leg, and clinical studies have also shown its effectiveness. Thus, more studies need to be done in cancers of other areas of the body with a clinical need for hyperthermia. A new applicator for heating of the abdomen has been installed in the MR

suite and protocols are being prepared for hyperthermia treatment of the bladder and cervix. The oil reference and breath hold correction methods developed in this work could be used in for these treatments, where system drift and breathing artifacts are expected.

In summary, more clinical experiments are needed to evaluate the effectiveness of these systems and techniques during hyperthermia treatment. Many studies and protocols have been approved or are in the process of being approved that will provide us with these clinical opportunities.

## Appendix

### Magnetic Resonance Imaging Review

Magnetic resonance imaging (MRI) is an imaging modality that relies on the precession of nuclei in a strong external magnetic field ( $B_0$ ) to determine their spatial location. The precession is dictated by the Larmor equation, which is

$$\omega_0 = \gamma B_0$$

where  $\omega_0$  is the precession angular frequency (rad/s) and  $\gamma$  is the gyromagnetic ratio (rad/s/Tesla). Of particular interest are the hydrogen nuclei, whose natural abundance in the human body as well as its high gyromagnetic ratio (42.6 MHz/Tesla) makes it the ideal candidate for imaging of the body.

To familiarize the reader with the process of acquiring images from these nuclei, a gradient echo sequence will be examined in detail. First, the magnetization of the nuclei,  $M_0$ , must be rotated (or “flipped”) perpendicular to the main magnetic field vector using a radiofrequency (RF) pulse (or excitation) centered at frequency  $\omega_0$ . The RF pulse must be at the Larmor frequency, since the nuclei can only absorb energy near the resonant Larmor frequency. The flipping of the magnetization is needed to detect the magnetization without interference from the main magnetic field,  $B_0$ . Unfortunately, if only the RF pulse is applied then all of the magnetization in the body will be flipped and present in the image. However, in many imaging applications, 2D images of thin slices of the body are desired. To achieve this, a magnetic field gradient is applied perpendicular to the slice desired, creating a gradient of precession frequencies. To excite only a portion of the spins, the RF pulse is bandlimited so that it only flips the

spins at those frequencies. The bandlimited RF pulse is created in the form of a sinc pulse, whose Fourier analog is the rect function. Knowing the gradient applied and the bandwidth and center frequency of the RF pulse, any slice of any size within the body can be excited.

Once the spins of the slice are flipped, they precess in the plane of the slice. To produce an image, the spins must be spatially encoded before acquisition of the data. The spatial encoding is performed to acquire data in k-space. In one direction a gradient is applied briefly to create a gradient of phases in that direction. This is called the phase encoding step and is labeled in Figure A1. Another gradient is applied in opposite direction, with a negative amplitude. At a time  $TE$ , an echo in the signal is formed by applying a positive gradient that is twice as long as the initial gradient. In 2D image acquisition, magnetic field gradients are applied in the two transverse planes (x and y) to encode the spatial position of each spin. First, a phase gradient is applied to spatially encode the phase in one direction. In the other direction, a readout gradient is played out to frequency encode the spins. The rotating field in the transverse plane then induces electric current in RF coils tuned to  $\omega_0$ . However, signal is only acquired during a readout gradient, which takes place at times  $TE_1$ ,  $TE_2$ , and  $TE_3$ . Multiple excitations are needed to acquire all the data needed to acquire an image, one for each line of k-space. The time between excitations is known as the repetition time, or TR time. Once all k-space lines are acquired, the signal is then frequency demodulated and a 2D FFT is performed to produce an image. A pulse sequence diagram of the gradient echo sequence can be found in Figure A1.

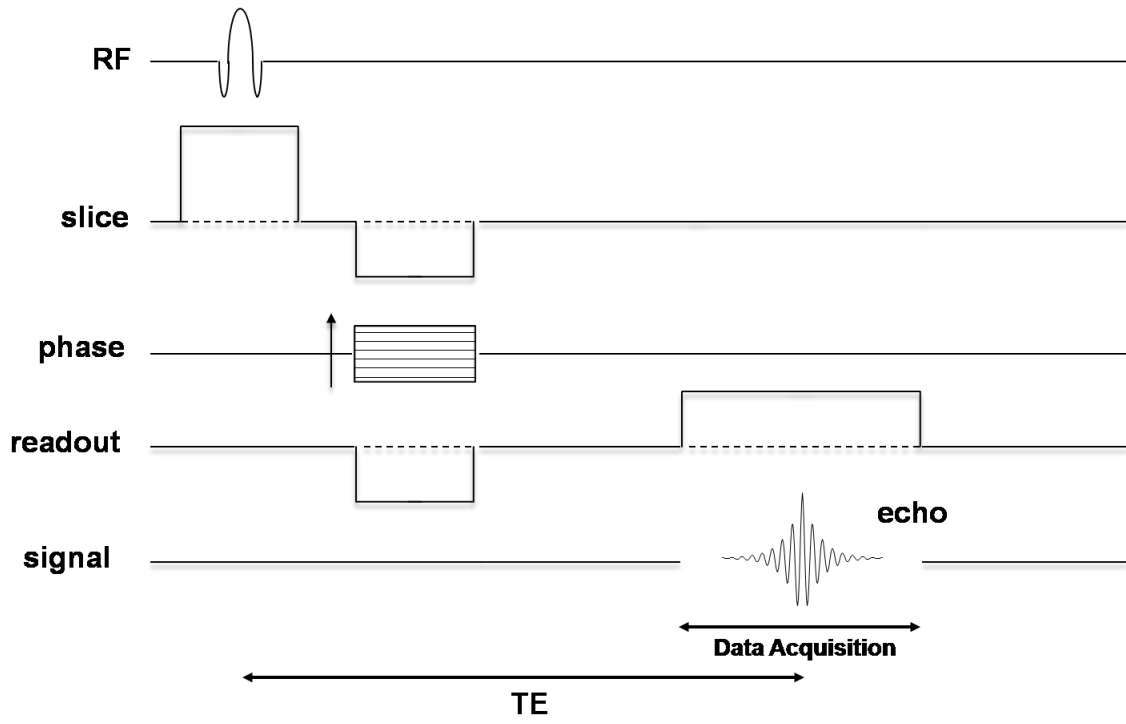


**Figure A1:** Gradient Echo Pulse Sequence Diagram

## MR Protocol for Breast Comfort Study

	Sequence	Volunteer number									
		1	2	3	4	5	6	7	8	9	10
1	3-Plane Localizer, TR=5, TE=1.7, FOV=36cm, Slice Thickness = 5mm, 10mm gap, Flip=30, NEX	X	X	X	X	X	X	X	X	X	X
2	Sagittal SSFSE sequence. 256x192 matrix. TR = min(~1000) TE = min(~61), slice thickness=4mm, spacing = 1mm, FOV = 36cm		X	X	X	X	X	X	X	X	FOV=44cm, spacing=5mm
3	Axial T1 weighted, freq A/P, BW=15.63kHz, TE=min full(16), TR=500, FOV=36cm, slice thickness=4mm, 1mm gap, 320x192 matrix, NEX=1, NPW, Fat Saturation			X	X	X	X	X	X	X	X
4	Axial SSFSE sequence. 256x192 matrix. TR = min(~767) TE = min(~28), slice thickness=5mm, spacing = 10mm, FOV = 36cm	X									
5	Sagittal T1 weighted, freq A/P, BW=15.63kHz, TE=min full(16), TR=500, FOV=36cm, slice thickness=4mm, 1mm gap, 320x192 matrix, NEX=1, NPW, Fat Saturation	X		X							
6	Axial GRE. TR=34, TE=3.1, slice thickness = 10mm, Flip = 30, 256x128 matrix, FOV = 40cm, spacing=11.5		X								
7	High Res T2 weighted scan: Axial FRFSE, phase A/P, BW=32 KHz, ETL=16, single echo, TE=min(~110), TR=4000, FOV=40cm, 4mm slice, 5mm spacing, 512x256, NEX=2, NPW, Fat Saturation		X	X	X						
8	Axial FSTIR, phase A/P, BW=32 KHz, ETL=16, single echo, TE=min(~62), TR=4000, FOV=36cm, 4mm slice, 5mm spacing, 512x256, NEX=1, NPW, Fat Saturation			X							
9	Triplet GRE images- freq A/P, TR = 34ms, Tes= 15.1, 16.6, 18.1, NEX=4, 128x128 matrix, FOV=40cm, Flip=30, slice thickness=10mm,		X		X	X	X	X	X	X	X
10	Triplet GRE images- freq A/P, TR = 500ms, Tes= 15.1, 16.6, 18.1, NEX=1, 128x128 matrix, FOV=40cm, Flip=30, slice thickness=10mm,				X						
11	Triplet GRE images- freq A/P, TR = 500ms, Tes= 51.2, 52.4, 53.6, 54.8, NEX=1, 128x128 matrix, FOV=40cm, Flip=30, slice thickness=10mm,				X						
12	Triplet GRE images- freq A/P, TR = 34ms, Tes= 6.3, 7.8, 9.3, NEX=4, 128x128 matrix, FOV=40cm, Flip=30, slice thickness=10mm,					X	X	X	X	X	X
13	Triplet GRE images- freq A/P, TR = 500ms, Tes= 6.3, 7.8, 9.3, NEX=1, 128x128 matrix, FOV=40cm, Flip=30, slice thickness=10mm,					X	X	X	X	X	X
14	Triplet GRE images- freq A/P, TR = 34ms, Tes= 20.7, 22.2, 23.7, NEX=4, 128x128 matrix, FOV=40cm, Flip=30, slice thickness=10mm,					X	X	X	X	X	X
15	Triplet GRE images- freq A/P, TR = 1000ms, Tes= 6.3, 7.8, 9.3, NEX=1, 128x128 matrix, FOV=40cm, Flip=30, slice thickness=10mm,					X	X	X	X	X	X
16	Triplet GRE images- freq A/P, TR = 34ms, Tes= 11.0, 12.5, 20.0, NEX=4, 128x128 matrix, FOV=40cm, Flip=30, slice thickness=10mm,					X		X	X	X	X
17	Performed #9 twice with large time period between them					X	X	X	X	X	X
18	Probe-P			X				X		X	



# Volunteer Questionnaire for Breast Comfort Study



**IRB #**

Pilot Study to Determine Prospective Patient's Level of Comfort when Using the Duke Breast Applicator System (DBAS) inside a 1.5T GE Magnetic Resonance Scanner

**COMFORT QUESTIONNAIRE**

We are interested in assessing comfort/discomfort aspects related to the imaging procedure you have just experienced. Please answer all the questions by circling a number that best applies to you. If you have additional comments about today's experience please enter them in the **Additional Comments** box.

Volunteer ID #: _____		Age _____		Today's Date: _____	
<p><b>1. How comfortable were you during the procedure?</b></p> <p>1                      2                      3                      4                      5                      6                      7            Very Uncomfortable                      Comfortable                      Very comfortable</p> <p>If 1 to 6, what was the source of your discomfort? (check all that apply)</p> <p><input type="checkbox"/> Enclosed space    <input type="checkbox"/> Body Position    <input type="checkbox"/> Breast Immersed in Water</p> <p><input type="checkbox"/> Requirement to Lie Still    <input type="checkbox"/> Other, specify: _____</p>					
<p><b>2. Did you feel any pain?</b></p> <p>1                      2                      3                      4            Not at all    A little    Quite a bit    Very much</p> <p>If 2, 3, or 4, explain: _____</p>					
<p><b>3. Did you feel tense?</b></p> <p>1                      2                      3                      4            Not at all    A little    Quite a bit    Very much</p> <p>If 2, 3 or 4, explain: _____</p>					
<p><b>4. Was the description of the procedure detailed enough to prepare you for the study?</b></p> <p>1                      2                      3                      4            Not at all    A little    Quite a bit    Very much</p> <p>If 2, 3 or 4, explain: _____</p>					
<p><b>5. Did you feel tired at end of the study?</b></p> <p>1                      2                      3                      4            Not at all    A little    Quite a bit    Very much</p> <p>If 2, 3 or 4, explain: _____</p>					
<p><b>Additional Comments:</b> _____</p> <p>_____</p>					
Study Supervised by: _____		Signature: _____			
Oana Craciunescu, Ph.D. DUMC, Radiation-Oncology, 5/22/07					

## References

1. *Image - Breast Anatomy*. March 14th, 2007 [cited 2010 April 2nd]; Available from: [http://www.breastcancer.org/pictures/breast\\_anatomy/image\\_1.jsp](http://www.breastcancer.org/pictures/breast_anatomy/image_1.jsp).
2. *Image - Axillary Lymph Nodes*. May 21st, 2008 [cited 2010 April 2nd]; Available from: [http://www.breastcancer.org/pictures/breast\\_anatomy/axillary\\_lymph\\_nodes.jsp](http://www.breastcancer.org/pictures/breast_anatomy/axillary_lymph_nodes.jsp).
3. Graham, S.J., P.L. Stanchev, J.O.A. Lloyd-Smith, M.J. Bronskill, and D.B. Plewes, *Changes in fibroglandular volume and water content of breast tissue during the menstrual cycle observed by MR imaging at 1.5 t*. *Journal of Magnetic Resonance Imaging*, 1995. 5(6): p. 695-701.
4. Kopans, D.B., *Breast Imaging, 2nd ed.* 1998, Lippincott-Raven: Philadelphia, PA. p. 3-27.
5. Wolfe, J.N., *Breast parenchymal patterns and their changes with age*. *Radiology*, 1976. 121(3 Pt. 1): p. 545-52.
6. Wang, J., P.-L. Torng, T.-P. Liu, K.-L. Chen, and T.T.-F. Shih, *Proton MR Spectroscopy in Normal Breasts Between Pre- and Postmenopausal Women: A Preliminary Study*. *Am. J. Roentgenol.*, 2008. 190(2): p. 505-510.
7. Shah, N., A.E. Cerussi, D. Jakubowski, et al., *Spatial variations in optical and physiological properties of healthy breast tissue*. *J Biomed Opt*, 2004. 9(3): p. 534-40.
8. *Stages of Breast Cancer*. *Breast Cancer Treatment* [cited 2009 12-14-2009]; Available from: <http://www.cancer.gov/cancertopics/pdq/treatment/breast/Patient/page2>.
9. Giordano, S.H., *Update on Locally Advanced Breast Cancer*. *Oncologist*, 2003. 8(6): p. 521-530.
10. Society, A.C. *Cancer Facts & Figures 2009*. 2009 [cited; Available from: [http://www.cancer.org/docroot/STT/content/STT\\_1x\\_Cancer\\_Facts\\_Figures\\_2009.asp](http://www.cancer.org/docroot/STT/content/STT_1x_Cancer_Facts_Figures_2009.asp).
11. Beckmann, M.W., D. Niederacher, H.-G. Schnürch, B.A. Gusterson, and H.G. Bender, *Multistep carcinogenesis of breast cancer and tumour heterogeneity*. *Journal of Molecular Medicine*, 1997. 75(6): p. 429-439.

12. Boecker, W., H. Buerger, K. Schmitz, et al., *Ductal epithelial proliferations of the breast: a biological continuum? Comparative genomic hybridization and high-molecular-weight cytokeratin expression patterns*. J Pathol, 2001. 195(4): p. 415-21.
13. Gao, Y., Y. Niu, X. Wang, L. Wei, and S. Lu, *Genetic changes at specific stages of breast cancer progression detected by comparative genomic hybridization*. J Mol Med, 2009. 87(2): p. 145-52.
14. Lee, S., S.K. Mohsin, S. Mao, et al., *Hormones, receptors, and growth in hyperplastic enlarged lobular units: early potential precursors of breast cancer*. Breast Cancer Res, 2006. 8(1): p. R6.
15. Sinn, H.P., *Breast cancer precursors: lessons learned from molecular genetics*. J Mol Med, 2009. 87(2): p. 113-5.
16. Osborne, C., P. Wilson and D. Tripathy, *Oncogenes and Tumor Suppressor Genes in Breast Cancer: Potential Diagnostic and Therapeutic Applications*. Oncologist, 2004. 9(4): p. 361-377.
17. Carroll, J.S., A. Swarbrick, E.A. Musgrove, and R.L. Sutherland, *Mechanisms of growth arrest by c-myc antisense oligonucleotides in MCF-7 breast cancer cells: implications for the antiproliferative effects of antiestrogens*. Cancer Res, 2002. 62(11): p. 3126-31.
18. Hollstein, M., D. Sidransky, B. Vogelstein, and C.C. Harris, *p53 mutations in human cancers*. Science, 1991. 253(5015): p. 49-53.
19. Ford, D., D.F. Easton and J. Peto, *Estimates of the gene frequency of BRCA1 and its contribution to breast and ovarian cancer incidence*. Am J Hum Genet, 1995. 57(6): p. 1457-62.
20. Easton, D.F., D.T. Bishop, D. Ford, and G.P. Crockford, *Genetic linkage analysis in familial breast and ovarian cancer: results from 214 families. The Breast Cancer Linkage Consortium*. Am J Hum Genet, 1993. 52(4): p. 678-701.
21. Rahman, N. and M.R. Stratton, *The genetics of breast cancer susceptibility*. Annu Rev Genet, 1998. 32: p. 95-121.
22. Haagensen, C.D. and A.P. Stout, *Carcinoma of the Breast. II-Criteria of Operability*. Ann Surg, 1943. 118(6): p. 1032-51.
23. Harris, J.R., J. Sawicka, R. Gelman, and S. Hellman, *Management of locally advanced carcinoma of the breast by primary radiation therapy*. Int J Radiat Oncol Biol Phys, 1983. 9(3): p. 345-9.

24. Hortobagyi, G.N., *Comprehensive management of locally advanced breast cancer*. Cancer, 1990. 66(6 Suppl): p. 1387-91.
25. Hortobagyi, G., Budzar, A.U., *Locally advanced breast cancer: a review including the MD Anderson Experience.*, in Ragaz, J., Ariel, I., eds. *High-Risk Breast Cancer*. 1991, Springer-Verlag: Berlin. p. 382.
26. Green, M., S. Giordano and G. Hortobagyi, *Medical Therapy of Locally Advanced Breast Cancer*, in *Breast Cancer and Molecular Medicine*. 2006. p. 427-447.
27. Bonadonna, G., P. Valagussa, A. Moliterni, M. Zambetti, and C. Brambilla, *Adjuvant Cyclophosphamide, Methotrexate, and Fluorouracil in Node-Positive Breast Cancer -- The Results of 20 Years of Follow-Up*. N Engl J Med, 1995. 332(14): p. 901-906.
28. *Polychemotherapy for early breast cancer: an overview of the randomised trials*. The Lancet, 1998. 352(9132): p. 930-942.
29. Pentti, G., H. Erkki, K. Pentti, and T. Jussi, *Adjuvant postoperative radiotherapy, chemotherapy, and immunotherapy in stage III breast cancer*. Cancer, 1984. 54(4): p. 670-674.
30. Chia, S., S.M. Swain, D.R. Byrd, and D.A. Mankoff, *Locally Advanced and Inflammatory Breast Cancer*. Journal of Clinical Oncology, 2008. 26(5): p. 786-790.
31. Fisher, B., J. Bryant, N. Wolmark, et al., *Effect of preoperative chemotherapy on the outcome of women with operable breast cancer*. J Clin Oncol, 1998. 16(8): p. 2672-85.
32. van der Hage, J.A., C.J. van de Velde, J.P. Julien, et al., *Preoperative chemotherapy in primary operable breast cancer: results from the European Organization for Research and Treatment of Cancer trial 10902*. J Clin Oncol, 2001. 19(22): p. 4224-37.
33. Evans, T.R., A. Yellowlees, E. Foster, et al., *Phase III randomized trial of doxorubicin and docetaxel versus doxorubicin and cyclophosphamide as primary medical therapy in women with breast cancer: an anglo-celtic cooperative oncology group study*. J Clin Oncol, 2005. 23(13): p. 2988-95.
34. Untch, M., Konecny, G., Ditsch, N., et al. *Dose dense sequential epirubicin-paclitaxel as preoperative treatment of breast cancer: Results of a randomised AGO study*. in *Proc Am Soc Clin Oncol*. 2002.

35. Shenkier, T., L. Weir, M. Levine, et al., *Clinical practice guidelines for the care and treatment of breast cancer: 15. Treatment for women with stage III or locally advanced breast cancer*. CMAJ, 2004. 170(6): p. 983-994.
36. McGuire, S.E., Gonzalez-Angulo, A.M., Tucker, S.L., et al., *Radiation is an important component of therapy for patients with stage III breast cancer who achieve a pathological complete response after neoadjuvant chemotherapy*. Int J Radiat Oncol Biol Phys, 2005. 63(85): p. abstr,suppl 2.
37. Bristol, I.J., Strom, E.A., Domain, D., et al., *Long term locoregional treatment outcomes for patients with inflammatory breast cancer* Int J Radiat Oncol Biol Phys, 2006. 66(2001): p. abstr, suppl 3.
38. Dewhurst, M., E. Jones, R.J. Samulski, et al., *Hyperthermia*, in *Cancer Medicine 6*, D.W. Kufe, et al., Editors. 2003, BC Decker, Inc.: Hamilton. p. 623-636.
39. Jones, E.L., L.R. Prosnitz, M.W. Dewhurst, et al., *Thermochemoradiotherapy Improves Oxygenation in Locally Advanced Breast Cancer*. Clinical Cancer Research, 2004. 10(13): p. 4287-4293.
40. Jones, E.L., J.R. Oleson, L.R. Prosnitz, et al., *Randomized trial of hyperthermia and radiation for superficial tumors*. Journal of Clinical Oncology, 2005. 23(13): p. 3079-85.
41. Paulides, M.M., J.F. Bakker, E. Neufeld, et al., *The HYPERcollar: A novel applicator for hyperthermia in the head and neck\**. International Journal of Hyperthermia, 2007. 23(7): p. 567-576.
42. Wu, L., R.J. McGough, O.A. Arabe, and T.V. Samulski, *An RF phased array applicator designed for hyperthermia breast cancer treatments*. Phys Med Biol, 2006. 51(1): p. 1-20.
43. Fatehi, D., J.v.d. Zee, M.d. Bruijne, M. Franckena, and G.C.v. Rhoon, *RF-power and temperature data analysis of 444 patients with primary cervical cancer: Deep hyperthermia using the Sigma-60 applicator is reproducible*. International Journal of Hyperthermia, 2007. 23(8): p. 623-643.
44. Johnson, J.E., D.G. Neuman, P.F. Maccarini, et al., *Evaluation of a dual-arm Archimedean spiral array for microwave hyperthermia*. International Journal of Hyperthermia, 2006. 22(6): p. 475-490.
45. Juang, T., P.R. Stauffer, D.G. Neuman, and J.L. Schlorff, *Multilayer conformal applicator for microwave heating and brachytherapy treatment of superficial tissue disease*. International Journal of Hyperthermia, 2006. 22(7): p. 527-544.

46. Titania, J., W. Jeffery, I.C. Hsu, and D. Chris. *Treatment delivery platform for conformal catheter-based ultrasound hyperthermia*. 2009: SPIE.
47. Rares, S., C.V. Frédéric, A.d.Z. Jacco, G. Nicolas, and T.W.M. Chrit, *Hyperthermia by MR-guided focused ultrasound: Accurate temperature control based on fast MRI and a physical model of local energy deposition and heat conduction*. *Magnetic Resonance in Medicine*, 2000. 43(3): p. 342-347.
48. Tasci, T.O., V. Ibrahim, A. Anil, et al., *Focused RF hyperthermia using magnetic fluids*. *Medical Physics*, 2009. 36(5): p. 1906-1912.
49. Jordan, A., P. Wust, H. Fähling, et al., *Inductive heating of ferrimagnetic particles and magnetic fluids: Physical evaluation of their potential for hyperthermia*. *International Journal of Hyperthermia*, 2009. 25(7): p. 499-511.
50. Falk, M.H. and R.D. Issels, *Hyperthermia in oncology*. *Int J Hyperthermia*, 2001. 17(1): p. 1-18.
51. Wust, P., B. Hildebrandt, G. Sreenivasa, et al., *Hyperthermia in combined treatment of cancer*. *Lancet Oncol*, 2002. 3(8): p. 487-97.
52. Vernon, C.C., J.W. Hand, S.B. Field, et al., *Radiotherapy with or without hyperthermia in the treatment of superficial localized breast cancer: results from five randomized controlled trials. International Collaborative Hyperthermia Group [see comments]*. *Int J Radiat Oncol Biol Phys*, 1996. 35(4): p. 731-44.
53. Overgaard, J., D. Gonzalez Gonzalez, M.C. Hulshof, et al., *Hyperthermia as an adjuvant to radiation therapy of recurrent or metastatic malignant melanoma. A multicentre randomized trial by the European Society for Hyperthermic Oncology*. *Int J Hyperthermia*, 1996. 12(1): p. 3-20.
54. Valdagni, R. and M. Amichetti, *Report of long-term follow-up in a randomized trial comparing radiation therapy and radiation therapy plus hyperthermia to metastatic lymph nodes in stage IV head and neck patients*. *Int J Radiat Oncol Biol Phys*, 1994. 28(1): p. 163-9.
55. Kitamura, K., H. Kuwano, M. Watanabe, et al., *Prospective randomized study of hyperthermia combined with chemoradiotherapy for esophageal carcinoma*. *J Clin Oncol*, 1995. 60: p. 55-58.
56. Kim, D.W., K. Blackwell, Z. Vujaskovic, et al., *A Phase I/II Study of Neoadjuvant Liposomal Doxorubicin, Paclitaxel and Hyperthermia in Locally Advanced Breast Cancer*. *International journal of radiation oncology, biology, physics*, 2008. 72(1): p. S183-S184.

57. Ponce, A.M., Z. Vujaskovic, F. Yuan, D. Needham, and M.W. Dewhirst, *Hyperthermia mediated liposomal drug delivery*. International Journal of Hyperthermia, 2006. 22(3): p. 205-213.
58. Nichols, J.W. and D.W. Deamer, *Catecholamine uptake and concentration by liposomes maintaining p/ gradients*. Biochim Biophys Acta, 1976. 455(1): p. 269-71.
59. Sharpe, M., S.E. Easthope, G.M. Keating, and H.M. Lamb, *Polyethylene glycol-liposomal doxorubicin: a review of its use in the management of solid and haematological malignancies and AIDS-related Kaposi's sarcoma*. Drugs, 2002. 62(14): p. 2089-126.
60. Papahadjopoulos, D., Gabizon, A., *Liposomes designed to avoid the reticuloendothelial system*. Prog Clin Biol Res, 1990. 343: p. 85-93.
61. Allen, T.M., C.B. Hansen and D.E.L. de Menezes, *Pharmacokinetics of long-circulating liposomes*. Advanced Drug Delivery Reviews, 1995. 16(2-3): p. 267-284.
62. Yuan, F., M. Dellian, D. Fukumura, et al., *Vascular permeability in a human tumor xenograft: molecular size dependence and cutoff size*. Cancer Res, 1995. 55(17): p. 3752-6.
63. Wu, N.Z., D. Da, T.L. Rudoll, et al., *Increased microvascular permeability contributes to preferential accumulation of Stealth liposomes in tumor tissue*. Cancer Res, 1993. 53(16): p. 3765-70.
64. Gabizon, A.A., O. Lyass, G.J. Berry, and M. Wildgust, *Cardiac safety of pegylated liposomal doxorubicin (Doxil/Caelyx) demonstrated by endomyocardial biopsy in patients with advanced malignancies*. Cancer Invest, 2004. 22(5): p. 663-9.
65. Needham, D., G. Anyarambhatla, G. Kong, and M.W. Dewhirst, *A new temperature-sensitive liposome for use with mild hyperthermia: characterization and testing in a human tumor xenograft model*. Cancer Res, 2000. 60(5): p. 1197-201.
66. Kong, G., G. Anyarambhatla, W.P. Petros, et al., *Efficacy of liposomes and hyperthermia in a human tumor xenograft model: importance of triggered drug release*. Cancer Res, 2000. 60(24): p. 6950-7.
67. Chen, Q., S. Tong, M.W. Dewhirst, and F. Yuan, *Targeting tumor microvessels using doxorubicin encapsulated in a novel thermosensitive liposome*. Mol Cancer Ther, 2004. 3(10): p. 1311-7.

68. Hand, J.W., D. Machin, C.C. Vernon, and J.B. Whaley, *Analysis of thermal parameters obtained during phase III trials of hyperthermia as an adjunct to radiotherapy in the treatment of breast carcinoma*. Int J Hyperthermia, 1997. 13(4): p. 343-64.
69. Kapp, D.S. and R.S. Cox, *Thermal treatment parameters are most predictive of outcome in patients with single tumor nodules per treatment field in recurrent adenocarcinoma of the breast [see comments]*. Int J Radiat Oncol Biol Phys, 1995. 33(4): p. 887-99.
70. Oleson, J.R., T.V. Samulski, K.A. Leopold, et al., *Sensitivity of hyperthermia trial outcomes to temperature and time: implications for thermal goals of treatment*. Int J Radiat Oncol Biol Phys, 1993. 25(2): p. 289-97.
71. Seegenschmiedt, M.H., P. Martus, R. Fietkau, et al., *Multivariate analysis of prognostic parameters using interstitial thermoradiotherapy (IHT-IRT): tumor and treatment variables predict outcome*. Int J Radiat Oncol Biol Phys, 1994. 29(5): p. 1049-63.
72. Sherar, M., F.F. Liu, M. Pintilie, et al., *Relationship between thermal dose and outcome in thermoradiotherapy treatments for superficial recurrences of breast cancer: data from a phase III trial*. Int J Radiat Oncol Biol Phys, 1997. 39(2): p. 371-80.
73. Sapareto, S.A. and W.C. Dewey, *Thermal dose determination in cancer therapy*. Int J Radiat Oncol Biol Phys, 1984. 10(6): p. 787-800.
74. Field, S.B. and C.C. Morris, *The relationship between heating time and temperature: its relevance to clinical hyperthermia*. Radiother Oncol, 1983. 1(2): p. 179-86.
75. Rosner, G.L., S.T. Clegg, D.M. Prescott, and M.W. Dewhirst, *Estimation of cell survival in tumours heated to nonuniform temperature distributions*. Int J Hyperthermia, 1996. 12(2): p. 303-4.
76. Dewhirst, M.W., Z. Vujaskovic, E. Jones, and D. Thrall, *Re-setting the biologic rationale for thermal therapy*. Int J Hyperthermia, 2005. 21(8): p. 779-90.
77. Jones, E., D. Thrall, M.W. Dewhirst, and Z. Vujaskovic, *Prospective thermal dosimetry: the key to hyperthermia's future*. International Journal of Hyperthermia, 2006. 22(3): p. 247-53.
78. Thrall, D.E., S.M. LaRue, D. Yu, et al., *Thermal dose is related to duration of local control in canine sarcomas treated with thermoradiotherapy.[see comment]*. Clinical Cancer Research, 2005. 11(14): p. 5206-14.



79. MacFall, J.R., D.M. Prescott, H.C. Charles, and T.V. Samulski, *1H MRI phase thermometry in vivo in canine brain, muscle, and tumor tissue*. Med Phys, 1996. 23(10): p. 1775-82.
80. Craciunescu, O.I., S.K. Das, R.L. McCauley, J.R. MacFall, and T.V. Samulski, *3D numerical reconstruction of the hyperthermia induced temperature distribution in human sarcomas using DE-MRI measured tissue perfusion: validation against non-invasive MR temperature measurements*. Int J Hyperthermia, 2001. 17(3): p. 221-39.
81. Carter, D.L., J.R. MacFall, S.T. Clegg, et al., *Magnetic resonance thermometry during hyperthermia for human high-grade sarcoma*. Int J Radiat Oncol Biol Phys, 1998. 40(4): p. 815-22.
82. Clegg, S.T., S.K. Das, Y. Zhang, et al., *Verification of a hyperthermia model method using MR thermometry*. Int J Hyperthermia, 1995. 11(3): p. 409-24.
83. Craciunescu, O.I., T.V. Samulski, J.R. MacFall, and S.T. Clegg, *Perturbations in hyperthermia temperature distributions associated with counter-current flow: numerical simulations and empirical verification*. IEEE Trans Biomed Eng, 2000. 47(4): p. 435-43.
84. Samulski, T.V., S.T. Clegg, S. Das, J. MacFall, and D.M. Prescott, *Application of new technology in clinical hyperthermia*. Int J Hyperthermia, 1994. 10(3): p. 389-94.
85. Lewa, C.J. and J.D. de Certaines, *Body Temperature Mapping by Magnetic Resonance Imaging*. Spectroscopy Letters: An International Journal for Rapid Communication, 1994. 27(10): p. 1369-1419.
86. Wlodarczyk, W., M. Hentschel, P. Wust, et al., *Comparison of four magnetic resonance methods for mapping small temperature changes*. Phys Med Biol, 1999. 44(2): p. 607-24.
87. Quesson, B., J.A. de Zwart and C.T. Moonen, *Magnetic resonance temperature imaging for guidance of thermotherapy*. J Magn Reson Imaging, 2000. 12(4): p. 525-33.
88. Denis de Senneville, B., B. Quesson and C.T. Moonen, *Magnetic resonance temperature imaging*. Int J Hyperthermia, 2005. 21(6): p. 515-31.
89. Viola Rieke, K.B.P., *MR thermometry*. Journal of Magnetic Resonance Imaging, 2008. 27(2): p. 376-390.

90. Ludemann, L., Wlodarczyk, W., Nadobny, J., Weihrauch, M., Gellermann, J., Wust, P., *Non-invasive magnetic resonance thermography during regional hyperthermia*. International Journal of Hyperthermia, 2010(In Press).
91. Zhang, Y., T.V. Samulski, W.T. Joines, et al., *On the accuracy of noninvasive thermometry using molecular diffusion magnetic resonance imaging*. Int J Hyperthermia, 1992. 8(2): p. 263-74.
92. Ong, J.T., J.A. d'Arcy, D.J. Collins, et al., *Sliding window dual gradient echo (SW-dGRE): T1 and proton resonance frequency (PRF) calibration for temperature imaging in polyacrylamide gel*. Phys Med Biol, 2003. 48(13): p. 1917-31.
93. Hynynen, K., *Focused Ultrasound Surgery guided by MRI*. Sci. Med., 1996. 3.
94. Zuo, C.S., A. Mahmood and A.D. Sherry, *TmDOTA-: A Sensitive Probe for MR Thermometry in Vivo*. Journal of Magnetic Resonance, 2001. 151(1): p. 101-106.
95. Seshan, V., M.J. Germann, P. Preisig, et al., *TmDOTP5- as a <sup>23</sup>Na shift reagent for the in vivo rat kidney*. Magn Reson Med, 1995. 34(1): p. 25-31.
96. Winter, P.M. and N. Bansal, *TmDOTP(5-) as a (<sup>23</sup>Na) shift reagent for the subcutaneously implanted 9L gliosarcoma in rats*. Magn Reson Med, 2001. 45(3): p. 436-42.
97. Chen, J.C., J.A. Moriarty, J.A. Derbyshire, et al., *Prostate Cancer: MR Imaging and Thermometry during Microwave Thermal Ablation-Initial Experience1*. Radiology, 2000. 214(1): p. 290-297.
98. McDannold, N., C.M. Tempny, F.M. Fennessy, et al., *Uterine Leiomyomas: MR Imaging-based Thermometry and Thermal Dosimetry during Focused Ultrasound Thermal Ablation*. Radiology, 2006. 240(1): p. 263-272.
99. Hynynen, K., O. Pomeroy, D.N. Smith, et al., *MR Imaging-guided Focused Ultrasound Surgery of Fibroadenomas in the Breast: A Feasibility Study*. Radiology, 2001. 219(1): p. 176-185.
100. Hynynen, K., N. McDannold, G. Clement, et al., *Pre-clinical testing of a phased array ultrasound system for MRI-guided noninvasive surgery of the brain--A primate study*. European Journal of Radiology, 2006. 59(2): p. 149-156.
101. Catane, R., A. Beck, Y. Inbar, et al., *MR-guided focused ultrasound surgery (MRgFUS) for the palliation of pain in patients with bone metastases--preliminary clinical experience*. Ann Oncol, 2007. 18(1): p. 163-167.

102. David Melodelima, R.S.J.-Y.C.Y.T.C.M.D.C., *Intraluminal high intensity ultrasound treatment in the esophagus under fast MR temperature mapping: In vivo studies*. *Magnetic Resonance in Medicine*, 2005. 54(4): p. 975-982.
103. Gellermann, J., W. Wlodarczyk, B. Hildebrandt, et al., *Noninvasive Magnetic Resonance Thermography of Recurrent Rectal Carcinoma in a 1.5 Tesla Hybrid System*. *Cancer Res*, 2005. 65(13): p. 5872-5880.
104. Gellermann, J., B. Hildebrandt, R. Issels, et al., *Noninvasive magnetic resonance thermography of soft tissue sarcomas during regional hyperthermia: correlation with response and direct thermometry*. *Cancer*, 2006. 107(6): p. 1373-82.
105. Schmidt, E.J., V.K. Reddy and J.N. Ruskin, *Nonenhanced magnetic resonance imaging for characterization of acute and subacute radiofrequency ablation lesions*. *Heart Rhythm*, 2007. 4(2): p. 215-7.
106. De Poorter, J., C. De Wagter, Y. De Deene, et al., *Noninvasive MRI thermometry with the proton resonance frequency (PRF) method: in vivo results in human muscle*. *Magn Reson Med*, 1995. 33(1): p. 74-81.
107. El-Sharkawy, A.M., M. Schar, P.A. Bottomley, and E. Atalar, *Monitoring and correcting spatio-temporal variations of the MR scanner's static magnetic field*. *MAGMA*, 2006. 19(5): p. 223-36.
108. Gellermann, J., W. Wlodarczyk, H. Ganter, et al., *A practical approach to thermography in a hyperthermia/magnetic resonance hybrid system: validation in a heterogeneous phantom*. *Int J Radiat Oncol Biol Phys*, 2005. 61(1): p. 267-77.
109. Wust, P., C.H. Cho, B. Hildebrandt, and J. Gellermann, *Thermal monitoring: invasive, minimal-invasive and non-invasive approaches*. *Int J Hyperthermia*, 2006. 22(3): p. 255-62.
110. Kuroda, K., K. Oshio, A.H. Chung, K. Hynynen, and F.A. Jolesz, *Temperature mapping using the water proton chemical shift: a chemical shift selective phase mapping method*. *Magn Reson Med*, 1997. 38(5): p. 845-51.
111. Kuroda, K., R.V. Mulkern, K. Oshio, et al., *Temperature mapping using the water proton chemical shift: Self-referenced method with echo-planar spectroscopic imaging*. *Magnetic Resonance in Medicine*, 2000. 43(2): p. 220-225.
112. Rieke, V. and K. Butts Pauly, *Echo combination to reduce proton resonance frequency (PRF) thermometry errors from fat*. *J Magn Reson Imaging*, 2008. 27(3): p. 673-7.

113. Hynynen, K., N. McDannold, R.V. Mulkern, and F.A. Jolesz, *Temperature monitoring in fat with MRI*. Magn Reson Med, 2000. 43(6): p. 901-4.
114. Kuroda, K., *Non-invasive MR thermography using the water proton chemical shift*. International Journal of Hyperthermia, 2005. 21(6): p. 547 - 560.
115. McDannold, N., K. Hynynen, K. Oshio, and R.V. Mulkern, *Temperature monitoring with line scan echo planar spectroscopic imaging*. Med Phys, 2001. 28(3): p. 346-55.
116. de Zwart, J.A., F.C. Vimeux, C. Delalande, P. Canioni, and C.T. Moonen, *Fast lipid-suppressed MR temperature mapping with echo-shifted gradient-echo imaging and spectral-spatial excitation*. Magn Reson Med, 1999. 42(1): p. 53-9.
117. Weidensteiner, C., B. Quesson, B. Caire-Gana, et al., *Real-time MR temperature mapping of rabbit liver in vivo during thermal ablation*. Magn Reson Med, 2003. 50(2): p. 322-30.
118. Galiana, G., R.T. Branca, E.R. Jenista, and W.S. Warren, *Accurate Temperature Imaging Based on Intermolecular Coherences in Magnetic Resonance*. Science, 2008. 322(5900): p. 421-424.
119. Hu, X., T.H. Le, T. Parrish, and P. Erhard, *Retrospective estimation and correction of physiological fluctuation in functional MRI*. Magn Reson Med, 1995. 34(2): p. 201-12.
120. van Gelderen, P., Moonen, C.T.W. . *Respiration induced changes of field homogeneity in the brain: implications for fMRI*. in *6th Annual Meeting of ISMRM*. 1998 (Abstract 422). Sydney, Australia.
121. Pierre-François Van de, M., P. Josef, H.G. Gary, U. Kamil, and H. Xiaoping, *Respiration-induced B0 fluctuations and their spatial distribution in the human brain at 7 Tesla*. Magnetic Resonance in Medicine, 2002. 47(5): p. 888-895.
122. Bolan, P.J., P.G. Henry, E.H. Baker, S. Meisamy, and M. Garwood, *Measurement and correction of respiration-induced B0 variations in breast 1H MRS at 4 Tesla*. Magn Reson Med, 2004. 52(6): p. 1239-45.
123. Nicky, H.G.M.P., W.B. Lambertus, M.S. Sara, L.V. Koen, and J.G.B. Chris, *Do respiration and cardiac motion induce magnetic field fluctuations in the breast and are there implications for MR thermometry?* Journal of Magnetic Resonance Imaging, 2009. 29(3): p. 731-735.

124. Hey, S., G. Maclair, B.D. de Senneville, et al., *Online correction of respiratory-induced field disturbances for continuous MR-thermometry in the breast*. Magn Reson Med, 2009. 61(6): p. 1494-9.
125. Rempp, H., P. Martirosian, A. Boss, et al., *MR temperature monitoring applying the proton resonance frequency method in liver and kidney at 0.2 and 1.5 T: segment-specific attainable precision and breathing influence*. MAGMA, 2008. 21(5): p. 333-43.
126. Marques, J.P. and R. Bowtell, *Application of a Fourier-based method for rapid calculation of field inhomogeneity due to spatial variation of magnetic susceptibility*. Concepts in Magnetic Resonance Part B: Magnetic Resonance Engineering, 2005. 25B(1): p. 65-78.
127. Raj, D., D.P. Paley, A.W. Anderson, R.P. Kennan, and J.C. Gore, *A model for susceptibility artefacts from respiration in functional echo-planar magnetic resonance imaging*. Phys Med Biol, 2000. 45(12): p. 3809-20.
128. Rares, S., S. Baudouin Denis de and T.W.M. Chrit, *A fast calculation method for magnetic field inhomogeneity due to an arbitrary distribution of bulk susceptibility*. Concepts in Magnetic Resonance Part B: Magnetic Resonance Engineering, 2003. 19B(1): p. 26-34.
129. Wowk, B., M.C. McIntyre and J.K. Saunders, *k-Space detection and correction of physiological artifacts in fMRI*. Magn Reson Med, 1997. 38(6): p. 1029-34.
130. van Gelderen, P., J.A. de Zwart, P. Starewicz, R.S. Hinks, and J.H. Duyn, *Real-time shimming to compensate for respiration-induced B0 fluctuations*. Magn Reson Med, 2007. 57(2): p. 362-8.
131. de Senneville, B.D., B. Quesson, P. Desbarats, et al. *Atlas-based motion correction for online MR temperature mapping*. in *Image Processing, 2004. ICIP '04. 2004 International Conference on*. 2004.
132. de Zwart, J.A., F.C. Vimeux, J. Palussiere, et al., *On-line correction and visualization of motion during MRI-controlled hyperthermia*. Magn Reson Med, 2001. 45(1): p. 128-37.
133. Pfeuffer, J., P.F. Van de Moortele, K. Ugurbil, X. Hu, and G.H. Glover, *Correction of physiologically induced global off-resonance effects in dynamic echo-planar and spiral functional imaging*. Magn Reson Med, 2002. 47(2): p. 344-53.
134. Vigen, K.K., B.L. Daniel, J.M. Pauly, and K. Butts, *Triggered, navigated, multi-baseline method for proton resonance frequency temperature mapping with respiratory motion*. Magn Reson Med, 2003. 50(5): p. 1003-10.

135. Shmatukha, A.V. and C.J. Bakker, *Correction of proton resonance frequency shift temperature maps for magnetic field disturbances caused by breathing*. Phys Med Biol, 2006. 51(18): p. 4689-705.
136. Rieke, V., K.K. Vigen, G. Sommer, et al., *Referenceless PRF shift thermometry*. Magn Reson Med, 2004. 51(6): p. 1223-31.
137. McDannold, N., C. Tempany, F. Jolesz, and K. Hynynen, *Evaluation of referenceless thermometry in MRI-guided focused ultrasound surgery of uterine fibroids*. J Magn Reson Imaging, 2008. 28(4): p. 1026-32.
138. Scott, B.R., W. Zhifei, Y. Huanzhou, et al., *Multicoil Dixon chemical species separation with an iterative least-squares estimation method*. Magnetic Resonance in Medicine, 2004. 51(1): p. 35-45.
139. Styner, M., C. Brechbuhler, G. Szekely, and G. Gerig, *Parametric estimate of intensity inhomogeneities applied to MRI*. IEEE Trans Med Imaging, 2000. 19(3): p. 153-65.
140. Vovk, U., F. Pernus and B. Likar, *MRI intensity inhomogeneity correction by combining intensity and spatial information*. Phys Med Biol, 2004. 49(17): p. 4119-33.
141. Lin, F.H., Y.J. Chen, J.W. Belliveau, and L.L. Wald, *A wavelet-based approximation of surface coil sensitivity profiles for correction of image intensity inhomogeneity and parallel imaging reconstruction*. Hum Brain Mapp, 2003. 19(2): p. 96-111.
142. Wyatt, C., Soher, B, Maccarini, P, Charles, HC, Stauffer, P, et al., *Hyperthermia MRI temperature measurement: Evaluation of measurement stabilisation strategies for extremity and breast tumours*. International Journal of Hyperthermia, 2009. 25(6): p. 422-433.
143. Franke, R., *Smooth Interpolation of scattered data by local thin plate splines*. Computers Math with Applic., 1982. 8(4): p. 273-281.
144. Madsen, E.L., M.A. Hobson, G.R. Frank, et al., *Anthropomorphic breast phantoms for testing elastography systems*. Ultrasound Med Biol, 2006. 32(6): p. 857-74.
145. Zhang, Y., W.T. Joines, R.L. Jirtle, and T.V. Samulski, *Theoretical and measured electric field distributions within an annular phased array: consideration of source antennas*. IEEE Trans Biomed Eng, 1993. 40(8): p. 780-7.
146. Li, Z., et al., *Towards the Validation of a Commercial Hyperthermia Planning System*. Microwave Journal, 2008. 51(12): p. 28.

147. Peters, R.D., et al., *Ex vivo tissue-type independence in proton-resonance frequency shift MR thermometry*. *Magnetic Resonance in Medicine*, 1998. 40(3): p. 454-459.
148. Soher, B.J., Wyatt, C., Reeder, S.B., MacFall, J.R. *Temperature Mapping with IDEAL Water-Fat Phase Differences*. in *Proceedings of the International Society of Magnetic Resonance in Medicine*. 2008. Toronto, ON.
149. Van-Trees, H., *Detection, estimation and modulation theory: part I*. 1968, New York: Wiley.
150. Barrett, H., Myers, KJ, *Foundations of image science*. 2004, New York: Wiley.
151. Pineda, A.R., S.B. Reeder, Z. Wen, and N.J. Pelc, *Cramer-Rao bounds for three-point decomposition of water and fat*. *Magn Reson Med*, 2005. 54(3): p. 625-35.
152. Cheng, L., P. Xinyi, Y. Kui, et al. (2009) *An internal reference model-based PRF temperature mapping method with Cramer-Rao lower bound noise performance analysis*. *Magnetic Resonance in Medicine* Volume, NA DOI: 10.1002/mrm.22121
153. Soher, B., Wyatt, CR., Reeder, SB., MacFall, JR., *Non-invasive Temperature Mapping with MRI using Chemical Shift Water-Fat Separation*. *Magnetic Resonance in Medicine*, 2010.
154. Peters, R.D., R.S. Hinks and R.M. Henkelman, *Ex vivo tissue-type independence in proton-resonance frequency shift MR thermometry*. *Magn Reson Med*, 1998. 40(3): p. 454-9.
155. Bydder, M., T. Yokoo, G. Hamilton, et al., *Relaxation effects in the quantification of fat using gradient echo imaging*. *Magn Reson Imaging*, 2008. 26(3): p. 347-59.
156. Yu, H., A. Shimakawa, C.A. McKenzie, et al., *Multiecho water-fat separation and simultaneous R2\* estimation with multifrequency fat spectrum modeling*. *Magn Reson Med*, 2008. 60: p. 1122-1134.
157. Yu, H., A. Shimakawa, C.A. McKenzie, et al., *Multiecho water-fat separation and simultaneous R2\* estimation with multifrequency fat spectrum modeling*. *Magn Reson Med*, 2008. 60(5): p. 1122-34.
158. Richard, K., A.W. Michael, S.L. Kenneth, et al., *Improved fat suppression using multipeak reconstruction for IDEAL chemical shift fat-water separation: Application with fast spin echo imaging*. *Journal of Magnetic Resonance Imaging*, 2009. 29(2): p. 436-442.

159. McDannold, N., A.S. Barnes, F.J. Rybicki, et al., *Temperature mapping considerations in the breast with line scan echo planar spectroscopic imaging*. Magn Reson Med, 2007. 58(6): p. 1117-23.
160. Soher, B.J., P.C. van Zijl, J.H. Duyn, and P.B. Barker, *Quantitative proton MR spectroscopic imaging of the human brain*. Magn Reson Med, 1996. 35(3): p. 356-63.
161. Zhang, Y., W.T. Joines, R.L. Jirtle, and T.V. Samulski, *Theoretical and measured electric field distributions within an annular phased array: Consideration of source antennas*. IEEE Trans Biomed Eng, 1993. 40: p. 780-787.
162. in *Numerical Recipes: The Art of Scientific Computing, Third Edition*. 2007, Cambridge University Press. p. 722.
163. de Zwart, J.A., P. van Gelderen, D.J. Kelly, and C.T. Moonen, *Fast magnetic-resonance temperature imaging*. J Magn Reson B, 1996. 112(1): p. 86-90.
164. Hamilton, G., M.S. Middleton, M. Bydder, et al., *Effect of PRESS and STEAM sequences on magnetic resonance spectroscopic liver fat quantification*. J Magn Reson Imaging, 2009. 30(1): p. 145-52.
165. Peters, N.H., L.W. Bartels, S.M. Sprinkhuizen, K.L. Vincken, and C.J. Bakker, *Do respiration and cardiac motion induce magnetic field fluctuations in the breast and are there implications for MR thermometry?* J Magn Reson Imaging, 2009. 29(3): p. 731-5.
166. Yu, H., C.A. McKenzie, A. Shimakawa, et al., *Multiecho reconstruction for simultaneous water-fat decomposition and T2\* estimation*. J Magn Reson Imaging, 2007. 26(4): p. 1153-61.
167. Bollard, M.E., S. Garrod, E. Holmes, et al., *High-resolution (1)H and (1)H-(13)C magic angle spinning NMR spectroscopy of rat liver*. Magn Reson Med, 2000. 44: p. 201-207.
168. Griffin, J.L., K.K. Lehtimaki, P.K. Valonen, et al., *Assignment of 1H Nuclear Magnetic Resonance Visible Polyunsaturated Fatty Acids in BT4C Gliomas Undergoing Ganciclovir-Thymidine Kinase Gene Therapy-induced Programmed Cell Death1*. Cancer Res, 2003. 63: p. 3195-3201.
169. Griffin, J.L., H.J. Williams, E. Sang, and J.K. Nicholson, *Abnormal lipid profile of dystrophic cardiac tissue as demonstrated by one- and two-dimensional magic-angle spinning (1)H NMR spectroscopy*. Magn Reson Med, 2001. 46: p. 249-255.



170. Knothe, G. and J.A. Kenar, *Determination of the fatty acid profile by <sup>1</sup>H NMR spectroscopy*. Eur. J. Lipid Sci. Technol., 2004. 106: p. 88-96.
171. Liu, C.Y., C.A. McKenzie, H. Yu, J.H. Brittain, and S.B. Reeder, *Fat quantification with IDEAL gradient echo imaging: correction of bias from T(1) and noise*. Magn Reson Med, 2007. 58(2): p. 354-64.
172. Lu, W., H. Yu, A. Shimakawa, et al., *Water-fat separation with bipolar multiecho sequences*. Magn Reson Med, 2008. 60(1): p. 198-209.
173. Lu, W. and B.A. Hargreaves, *Multiresolution field map estimation using golden section search for water-fat separation*. Magn Reson Med, 2008. 60(1): p. 236-44.

## **Biography**

Cory Robert Wyatt

### **Born**

April 7<sup>th</sup>, 1984

Richland, Washington USA

### **Education**

**Duke University**, Durham, North Carolina

Ph.D. Biomedical Engineering, May 2010

**University of Washington**, Seattle, Washington

BS, Bioengineering, June 2006

Minor Mathematics

### **Honors and Affiliations**

NIH Medical Imaging Training Grant Recipient (2006-2008)

2010 recipient of the International Journal of Hyperthermia Informa-Yamamoto Editor's award in Physics/Engineering

International Society of Magnetic Resonance Member 2005-present

Society of Thermal Medicine Member

## Publications

**Wyatt CR.**, Soher, BJ., Maccarrini, P., Stauffer, P., MacFall, JR. Hyperthermia MRI Temperature Measurement: Evaluation of Measurement Stabilization Strategies for Extremity and Breast Tumors. *International Journal of Hyperthermia*, 25(6): 422-433. DOI:10.1080/02656730903133762.

**Wyatt, CR.**, Soher, BJ., Arunachalam, K., MacFall, JR. Cramer-rao bounds for magnetic resonance temperature change measurement in fat-water voxels using multi-echo imaging. In Review with *Physics in Medicine and Biology*

**Wyatt, CR.**, Soher, BJ., MacFall, JR. Correction of Breath Hold Artifacts in MR Thermometry in Locally Advanced Breast Cancer using Multi-echo B<sub>0</sub> Field Estimation. In Preparation.

Soher, BJ., **Wyatt, CR.**, Reeder, SB., MacFall, JR. Non-invasive Temperature Mapping with MRI using Chemical Shift Water-Fat Separation. In Press with the *Journal of Magnetic Resonance in Medicine*.

Yuan, Y., **Wyatt, CR.**, Maccarrini, P., Stauffer, P, MacFall, JR., Dewhirst, M., Das, SK. A heterogeneous human tissue mimicking phantom for RF heating and MRI thermal monitoring verification. In Preparation.

OI Craciunescu, PR Stauffer, BJ Soher, **CR Wyatt**, O Arabe, P Maccarrini, SK Das, KS Cheng, TZ Wong, EL Jones, MW Dewhirst, Z Vujaskovic, JR MacFall, Accuracy of real time noninvasive temperature measurements using magnetic resonance thermal imaging in patients treated for high grade extremity soft tissue sarcomas., *Medical Physics*, United States, vol. 36 no. 11 (November, 2009), pp. 4848-58

## Abstracts and Conference Proceedings

**C. Wyatt**, B. Soher, J. MacFall. Use of Fat-Water Phase Difference to Stabilize MR Thermometry. In: *Proceedings of the Society of Thermal Medicine*; 2007 May 13-17; Washington D.C. Abstract No. 33.

Soher, BJ, **Wyatt, CR**, Stakhursky, V, MacFall, JR. Correcting for B<sub>0</sub> Field Drift in MR Temperature Mapping with Oil References. In: *Proceedings of the International Society of Magnetic Resonance in Medicine*; 2008 May 3-9; Toronto, ON. Abstract No. 3029.

Soher, BJ, **Wyatt, CR**, Reeder, S, MacFall, JR. Temperature Mapping with IDEAL Water-Fat Phase Differences. In: *Proceedings of the International Society of Magnetic Resonance in Medicine*; 2008 May 3-9; Toronto, ON. Abstract No. 3018.

PR Stauffer, OI Craciunescu, PF Maccarini, **C Wyatt**, K Arunachalam, O Arabe, V Stakhursky, B Soher, JR MacFall, Z Li, WT Joines, S. Rangarao, KS Cheng, SK Das, CD Martins, C Charles, MW Dewhirst, T Wong, E Jones, Z Vujaskovic. Clinical Utility of Magnetic Resonance Thermal Imaging (MRTI) For Realtime Guidance of Deep Hyperthermia. In: *Proc. SPIE*, Vol. 7181, 71810I (2009); doi:10.1117/12.812188

Yuan, Y., **Wyatt, CR.**, Maccarini, P., Stauffer, P, MacFall, JR., Dewhirst, M., Das, SK. A heterogeneous human tissue mimicking phantom for RF heating and MRI thermal monitoring verification. In: *Proceedings of the Society of Thermal Medicine*; 2009 April 3-7; Tuscon, AZ.

Yuan, Y., **Wyatt, CR.**, Maccarini, P., Stauffer, P, MacFall, JR., Dewhirst, M., Das, SK. A novel steering technique for optimal heating in hyperthermia. In: *Proceedings of the Society of Thermal Medicine*; 2010 April 23-26; Clearwater, FL.

**Wyatt, CR**, Soher, BJ, MacFall, JR. Temperature and B0 Field Measurement Bias of Multi-echo Fat-Water Fitting Algorithms. In: *Proceedings of the International Society of Magnetic Resonance in Medicine*; 2010 May 1-7; Stockholm, Sweden. Abstract No. 1820

**Wyatt, CR**, Soher, BJ, MacFall, JR. Optimal Multi-echo Water-Fat Separated Imaging Parameters for Temperature Change Measurement using Cramer-Rao Bounds. In: *Proceedings of the International Society of Magnetic Resonance in Medicine*; 2010 May 1-7; Stockholm, Sweden. Abstract No. 1821

**Wyatt, CR**, Soher, BJ, MacFall, JR. Breath Hold Phase Correction for Water-Fat Separated MR Thermometry Using B0 Field Changes. In: *Proceedings of the International Society of Magnetic Resonance in Medicine*; 2010 May 1-7; Stockholm, Sweden. Abstract No. 4147